Accurate Modeling of the Neutral and Unstable Atmospheric Boundary Layer at Horns Rev using the k-ε Method in FLUENT 6.3

A Thesis

Presented to

the Faculty of the Department of Mechanical Engineering

University of Houston

In Partial Fulfillment

of the Requirements for the Degree

Master of Science

in Mechanical Engineering

by

Natalie Martin

December 2012

Accurate Modeling of the Neutral and Unstable Atmospheric Boundary Layer at Horns Rev using the k-ε Method in FLUENT 6.3

Natalie Martin

Approved:

Chair of the Committee
Dr. Ralph Metcalfe, Professor
Mechanical Engineering

Committee Members:

Dr. Stanley Kleis, Associate Professor
Mechanical Engineering

Dr. Bernhard Rappenglück,
Associate Professor
Earth & Atmospheric Sciences

Dr. Suresh K. Khator,
Associate Dean
Cullen College of Engineering

Dr. Pradeep Sharma,
Professor and Chair
Mechanical Engineering

Acknowledgements

This research was partially funded by the University of Houston's Cullen College of Engineering and the Mechanical Engineering Department through the Graduate Tuition Scholarship Fund. Thanks to Dr. Ralph Metcalfe for his advisement and the quality discussion time that ultimately led to the success of this manuscript. Additional gratitude is extended to the defense committee members, Dr. Stanley Kleis and Dr. Bernhard Rappenglück, for their commitment to this project.

Accurate Modeling of the Neutral and Unstable Atmospheric Boundary Layer at Horns Rev using the k-ε Method in FLUENT 6.3

An Abstract

of a

Thesis

Presented to

the Faculty of the Department of Mechanical Engineering

University of Houston

In Partial Fulfillment

of the Requirements for the Degree

Master of Science

in Mechanical Engineering

by

Natalie Martin

December 2012

Abstract

A k-ε code is customized in FLUENT 6.3 to simulate neutral and unstable atmospheric boundary layers (ABL) derived from Monin-Obukhov (MO) similarity theory. The code is tuned until velocity, temperature, turbulent kinetic energy (TKE), and turbulent dissipation rate (TDR) results maintain the initial theoretical values at upstream and downstream positions in a 2D and 3D domain.

After verifying that the code is performing consistently, neutral and unstable initial profiles are constructed from averaged observations of the ABL at Horns Rev and are implemented into the k-ε code. The simulation results display that the Horns Rev velocity profiles are slightly under approximated in the neutral simulation and moderately over approximated in the unstable simulations. Moreover, the simulated TKE profile shows divergence from the initial MO TKE profile as the thermal stability becomes more unstable. A study of the developing 3D dynamics of a turbulent ABL illustrating structures such as vortices and streaks is not reported on, and the results display strictly steady parallel flow.

Table of Contents

Acknowledgements....iv
Abstract....vi
Table of Contents....vii
List of Figures....ix
List of Tables....xi
Acronyms and Abbreviations....xii
Nomenclature....xiv
1 Introduction....1
2 Meteorological Measurements at Horns Rev....6
2.1 Data Collection at M2....7
2.1.1 Cup Anemometers....7
2.1.2 Other Measuring Equipment at M2....10
2.2 A Review of Horns Rev Observations—1999-2007....12
2.2.1 Neckelmann & Petersen (2000) Observations....12
2.2.2 Hansen (2001) Observations....18
2.2.3 Tech-Wise (2002) Observations....22
2.2.4 Tambke *et al.* (2003) Observations....29
2.2.5 Peña *et al.* (2008) Observations....32
2.2.6 Larsén *et al.* (2011) Observations....46
3 Atmospheric Boundary Layer Theory....51
3.1 Theoretical Mean Profiles—u(z), T(z), k(z), and ε(z)....51
3.2 Roughness Length—z_0....55
3.2.1 The Charnock Parameter—α_c....56
3.3 Theoretical Turbulent Viscosity—μ_t....57
3.4 A Caveat on the Theoretical Convective Boundary Layer Height, z_i....58
4 FLUENT 6.3 Governing Equations....61
4.1 Reynolds Time-Averaged Navier-Stokes (RANS) Equations....61
4.2 The Governing Energy Equation....63
4.3 The Standard k-ε Method....65
4.3.1 Choice of k-ε Method Model Constants....67
4.3.2 Choice of Turbulent Energy Prandtl Number, Pr_t....68
4.4 FLUENT 6.3 Finite-Volume Method....70
5 Mesh Characteristics....72
6 Flow Characteristics....76
7 Boundary Conditions and Prescribed Quantities....79
8 Solution Approach and Numerical Schemes....83
9 Results....85
9.1 Convergence of Solution....87
9.2 Neutral and Unstable Verification Studies....88
9.2.1 Neutral Verification Study....88
9.2.1.1 Tuning Pr_t....90
9.2.1.2 Consistency of Velocity Inlet Boundary Conditions....93
9.2.1.3 Dimensionless Neutral Simulated Profiles....101
9.2.2 Unstable Verification Study....105
9.2.2.1 Correcting the Dimensionless Unstable TDR Profile....109
9.3 Neutral and Unstable Validation Studies....111
9.3.1 Neutral (N) Validation....119
9.3.2 Near Unstable (NU) Validation Study....125

9.3.3 Unstable (U) Validation Study……..... 127
9.3.4 Very Unstable (VU) Validation Study……..... 128
9.3.5 Comparison with a Horns Rev Data Set from Peña *et al.* (2008)…….....130
9.3.5.1 Suggested Correction for Simulations……...133
10 Limitations of the Customized k-ε Code……..... 139
11 Conclusion……..... 142
References……144
Appendix A: Computation of Wind Deficit, u_d…….....153
Appendix B: Correcting the Simulated Dimensionless TKE Profile……...154
B.1: Correcting the Dimensionless Neutral TKE Profile……158
B.2: Correcting the Dimensionless Unstable TKE Profile…….. 160
Appendix C: Stability Class Flow Parameter & Property Tables…….....164
C.1: NU Flow Parameter & Property Table…….....164
C.2: U Flow Parameter & Property Table……165
C.3: VU Flow Parameter & Property Table…….....166
Appendix D: Boundary Profile .txt File for 2D(L) N Verification Study…….....167

List of Figures

Figure 2.1: Horns Rev site description……6
Figure 2.2: Measurement setup on M2……...7
Figure 2.3: (Left) Direct flow distortion. (Right) Non-direct flow distortion……9
Figure 2.4: Non-direct flow distortion. 10
Figure 2.5: Measurement setup on M2…… 11
Figure 2.6: (Left) Wind speed probability distribution. (Right) Wind rose at 62 m ASL. 14
Figure 2.7: Wind speed vs direction sector at all observation heights. 15
Figure 2.8: Semi-log plot of height vs wind speed……... 15
Figure 2.9: Turbulence intensity vs wind speed. 16
Figure 2.10: Turbulence intensity vs direction sector……...17
Figure 2.11: Nominal wind speed observations at 50 m ASL……... 18
Figure 2.12: Nominal turbulence intensity observations at 50 m ASL……19
Figure 2.13: Turbulence intensity (Adapted, Hansen, 2001)…… 20
Figure 2.14: Wind speed distribution at 50 m ASL……... 21
Figure 2.15: Distribution of the turbulence intensity at 50 m ASL……... 21
Figure 2.16: Wind rose at 50 m ASL…… 22
Figure 2.17: Average observed wind speed……... 23
Figure 2.18: Wind direction frequency observed by the wind vane at 60 m ASL……... 24
Figure 2.19: Wind speed distribution at 62 m ASL……..... 24
Figure 2.20: Monthly variation of average wind speed……..... 25
Figure 2.21: Diurnal variation of wind speed at 62 m ASL. 25
Figure 2.22: Temperature distribution at 55 m ASL for 2001……... 27
Figure 2.23: Monthly mean temperature at 55 m ASL…… 27
Figure 2.24: Daily variation of mean temperature at 55 m ASL…… 28
Figure 2.25: M2 wind rose at 43 m ASL. 30
Figure 2.26: Ratio of wind speeds compared with the gradient Richardson number. 31
Figure 2.27: Open sea sector wind profiles outlined by potential temperature difference…… 32
Figure 2.28: LiDAR scanning geometry (Adapted, Peña *et al.*, 2006)……33
Figure 2.29: Installation of LiDAR……..... 34
Figure 2.30: Location of M2 and the transformer/platform (Peña *et al.*, 2008)……. 35
Figure 2.31: Validation of LiDAR observations at 63 m ASL (Hasager *et al.*, 2007)…… 37
Figure 2.32: Horizontal mean wind speed profiles extended using LiDAR data. 38
Figure 2.33: Correlation between M2 and LiDAR platform wind speeds. 39
Figure 2.34: Coupled LiDAR and M2 mean wind speed observations……. 39
Figure 2.35: Dimensionless averaged wind profiles and stability classes (Adapted)……... 40
Figure 2.36: Ambient water and air temperature (Peña *et al.*, 2008)……....41
Figure 2.37: Ambient water and air temperature for days 131 to 135 (Peña *et al.*, 2009)…… ...41
Figure 2.38: Linear regression analysis of daily average temperature (Hasager *et al.*, 2007)……..42
Figure 2.39: Deviation between MO length scale derived using sonic and bulk methods……...46
Figure 2.40: Frequency of seasonal stability classes from 1999-2005 (Adapted)……....47
Figure 2.41: Horns Rev showing all met masts and wind farm…… 49
Figure 2.42: Frequency of seasonal stability classes from 2003-2007 (Adapted)…… 49
Figure 3.1: Virtual potential temperature fluxes of two moderately buoyant LES simulations……... 59
Figure 5.1: Illustration of 2D(S) domain…….. 74
Figure 5.2: Illustrations of 2D(L) and 3D domains…….. 75
Figure 9.1: Neutral TKE profile for assorted Pr_t values……... 90
Figure 9.2: Neutral temperature profile results for assorted Pr_t values……91
Figure 9.3: Dimensionless neutral TDR profile results for assorted Pr_t values.....92
Figure 9.4: 2D(S) contours of vertical velocity, V(y), inhibiting regions near edges…….. 94
Figure 9.5: 2D(L) contours of vertical velocity. The 2D(S) domain is outlined in red at the inlet.....94

Figure 9.6: 3D domain x-y planes of vertical velocity, V(y), contours at various lateral positions……..……96
Figure 9.7: 3D domain x-z planes of vertical velocity, V(y), contours at various heights.....97
Figure 9.8: 3D domain y-z planes of vertical velocity, V(y), contours at various downstream positions……..……99
Figure 9.9: Martin's 2D(S) & 3D simulated dimensionless neutral verification results……101
Figure 9.10: Unintended y-velocity component generated in the 2D(S) neutral simulation……...103
Figure 9.11: Unintended y-velocity component generated in the 3D neutral simulation.....103
Figure 9.12: Unintended z-velocity component generated in the 3D neutral simulation.....104
Figure 9.13: 3D neutral verification simulated dimensionless profiles for $\sigma_\varepsilon = 1.1$……..104
Figure 9.14: Unstable verification simulated dimensionless profiles for the 2D(S) & 3D domains……106
Figure 9.15: Unstable verification simulated dimensionless profiles for the 3D domain.....107
Figure 9.16: Unintended y-velocity component generated in the 2D(S) unstable simulation.....108
Figure 9.17: Unintended y-velocity component generated in the 3D unstable simulation.....108
Figure 9.18: Unintended z-velocity component generated in the 3D unstable simulation.....109
Figure 9.19: Unstable verification simulated dimensionless profiles with the TDR correction……..111
Figure 9.20: Horns Rev average data at all observation heights classified by thermal stability.....113
Figure 9.21: Martin's election of stability regions used to generate the MO temperature profile……... 113
Figure 9.22: Stability classification of Horns Rev from 2003-2007. 115
Figure 9.23: Stability classification of Horns Rev from 1999-2006. 115
Figure 9.24: Dimensionless profile results for the N validation study at L = ∞.....121
Figure 9.25: Dimensionless profiles for the N validation study at two values of L using the neutral dimensionless parameterizations……..122
Figure 9.26: Dimensionless profile results for the N validation study at two values of L using the unstable dimensionless parameterizations.....123
Figure 9.27: Dimensionless profile results for the N validation study at L = -1531 m…….. 125
Figure 9.28: Dimensionless profile results for the NU validation study at L = -288 m…… 126
Figure 9.29: Dimensionless profile results for the U validation study at L = -139 m…… 127
Figure 9.30: Dimensionless profile results for the VU validation study at L = -73 m……..... 129
Figure 9.31: Martin's simulation results plotted together with Peña *et al.* (2008)……. 131
Figure 9.32: Martin's simulation results plotted together with Peña *et al.* (2008). (abscissa = 27-35) 133
Figure 9.33: Martin's corrected simulation results plotted together with Peña *et al.* (2008)……. 135
Figure 9.34: Sonic-derived and M2 bulk Richardson number-derived stability bins……136
Figure 9.35: Proposed linear relationship between two MO length scales.....137
Figure A.1: Iso-speed plots used to compute the wind deficit. 153
Figure B.1: Domain details of mesh 3D(S) …… 155
Figure B.2: Dimensionless TKE profiles for assorted σ_ε in the 3D(S) neutral verification study. 158
Figure B.3: Dimensionless TKE profile for $\sigma_\varepsilon = 1.1$ in the 3D(S) neutral verification study. 159
Figure B.4: Neutral verification simulated dimensionless profiles for the enlarged 3D domain using $\sigma_\varepsilon = 1.1$……160
Figure B.5: Dimensionless TKE profiles for assorted σ_ε in the 3D(S) unstable verification study. 161
Figure B.6: Dimensionless TKE profile for $\sigma_\varepsilon = 1.1$ in the 3D(S) unstable verification study. 161
Figure B.7: Dimensionless U verification profiles on the 3D enlarged domain for $\sigma_\varepsilon = 1.1$. 162

List of Tables

Table 2.1: Mean data at Horns Rev from May 1999 to January 2000. 13
Table 2.2: Data coverage for M2 22
Table 2.3: Mean 10-minute statistics at M2 23
Table 2.4: Average 3D turbulence statistics at 50 m ASL 26
Table 2.5: Stability distribution from May 1999 to December 2002. 29
Table 2.6: Data availability for LiDAR and M2 measurements (Adapted, Peña *et al.*, 2009)..... 36
Table 2.7: Stability classes according to MO length. 43
Table 2.8: Averaged stability classes from Peña *et al.* (2008). 43
Table 2.9: Data availability at Horns Rev for M2 & M7 (Adapted). 47
Table 4.1: Review of k-ε Method Constants since 1972. 68
Table 5.1: Domain characteristics..... 74
Table 6.1: Flow quantities and parameters for the neutral verification case..... 77
Table 9.1: Dimensionless relations for neutral simulations 86
Table 9.2: Dimensionless relations for unstable simulations 87
Table 9.3: Convergence details for the neutral and unstable 2D and 3D verification simulations..... 88
Table 9.4: Neutral verification study flow parameters. 89
Table 9.5: Unstable flow parameters..... 105
Table 9.6: Average data categorized by stability class..... 112
Table 9.7: Stability classes selected by Martin and comparison of three bulk Richardson number formulations..... 118
Table 9.8: Stability classes categorized by MO length scale range..... 118
Table 9.9: Adiabatic neutral property table..... 119
Table 9.10: Diabatic neutral property table..... 120
Table 9.11: Corrected $\bar{L}_b$ and u_{15}. 134
Table B.1: Domain characteristics for mesh 3D(S) 156
Table B.2: Recommended pre-processed σ_ε for neutral and unstable verification & validation simulations 163
Table C.1: NU flow parameter & property table 164
Table C.2: U flow parameter & property table..... 165
Table C.3: VU flow parameter & property table..... 166

Acronyms and Abbreviations

1D	One-Dimensional
2D	Two-Dimensional
3D	Three-Dimensional
ABL	Atmospheric Boundary Layer
ANSYS	ANSYS, Inc. (Analysis System for Static and Dynamic Problems)
ASL	Above Sea Level
BC	Boundary Condition
BSL	Below Sea Level
CBL	Convective Boundary Layer
CFD	Computational Fluid Dynamics
CFF	Custom Field Function
DES	Detached Eddy Simulation
DNN	Danish Normal Zero (or mean sea level)
DNS	Direct Numerical Simulation
DONG Energy	Dansk Olie og Naturgas A/S
FE	Finite Element
FLUENT	Fluent Inc. CFD software program
FV	Finite Volume
GW	Gigawatt
IBL	Internal Boundary Layer
LES	Large Eddy Simulation
LiDAR	Light Detection And Ranging
LOS	Line Of Sight
M2	Meteorological Mast 2
M7	Meteorological Mast 7
Ma	Mach Number
MO	Monin-Obukhov
N	Neutral
N	North
NE	Northeast
NNS	Neutral & Near Stable
NNU	Neutral & Near Unstable
NNW	North Northwest
NU	Near Unstable
Nu	Nusselt Number
NW	Northwest
OCC	Open Cellular Convection
PBL	Planetary Boundary Layer

PCT (or pct)	Percentage
PDF (pdf)	Probability Density Function
Pr	Prandtl Number
PRESTO!	PREssure STaggered Option
R & D	Research & Development
Ra	Rayleigh Number
RANS	Reynolds Averaged Navier Stokes
Re	Reynolds Number
RH	Richards and Hoxey
R or Ri	Richardson Number
Risø-DTU	Risø -Technical University of Denmark
S	South
SBL	Stable Boundary Layer
SGS	Subgrid Scale
SIMPLE	Semi-Implicit Method for Pressure Linked Equations
SIMPLEC	SIMPLE-Consistent
SoDAR	Sound Detection And Ranging
SS	Steady State
SST	Sea Surface Temperature
SSW	South Southwest
SW	Southwest
TDR	Turbulence Dissipation Rate
TI	Turbulence Intensity
TKE	Turbulent Kinetic Energy
U	Unstable
UDF	User Defined Function
VS	Very Stable
VU	Very Unstable
W	West
WRF	Weather Research and Forecasting

Nomenclature

Greek Symbols	
α_C	Charnock parameter (= 0.012)
β [K^{-1}]	thermal expansion coefficient
δ [m]	displacement thickness
δ_{ij}	Kronecker delta
ε [m^2/s^3]	turbulent kinetic energy dissipation rate
ε_o [m^2/s^3]	turbulent dissipation rate given by MO similarity theory
ε_R [m]	sand grain roughness height used in 'Wall Boundary' panel in FLUENT
θ [m]	momentum thickness
θ [°]	instantaneous azimuth angle
θ [K]	potential temperature or potential temperature at highest height of a pair of temperature measurements
θ_d or θ [°]	wind direction
θ_{M2} [°]	angle of open sea wind directions at Horns Rev met mast M2 (= 174-13°)
θ_P [°]	angle of open sea wind directions at Horns Rev platform (= 270-10°)
θ_{rel} [°]	relative flow angle measured between the boom/lattice and the wind direction
Θ_v[K]	mean virtual potential temperature
κ	von Kármán constant
μ [Pa s]	dynamic viscosity
μ_{eff} [Pa s]	dynamic viscosity given in deviatoric stress tensor relation
μ_t [Pa s]	dynamic turbulent viscosity
μ_{to} [Pa s]	turbulent eddy viscosity given by MO similarity theory
ν [m^2/s]	kinematic viscosity
ξ	1D element
ρ [kg/m^3]	density of air (= 1.225)
σ_k	turbulent kinetic energy Prandtl number
σ_ε	turbulent dissipation rate Prandtl number
$(\tau_{ij})_{eff}$ [Pa]	deviatoric stress tensor
ϕ [°]	angle measured from the zenith (= 30.6°); also instantaneous scalar
ϕ_ε	non-dimensional turbulent dissipation rate used in MO similarity theory expressions
ϕ_m	non-dimensional wind shear
Latin Symbols	
a [m/s]	speed of sound
C	constant used to compute ABL height (= 0.12)
C_1	empirical constant used to determine MO length scale (= 10)
c_p [J/kgK]	specific heat of air
C_S	roughness constant used in 'Wall Boundary' panel; default (= 0.5)
C_t	thrust coefficient
$C_{\varepsilon 1}, C_{\varepsilon 2}, C_{\varepsilon 3}$	dissipation rate k-ε model constants
C_μ	turbulent viscosity constant in k-ε model
E	empirical constant for a smooth wall; FLUENT default value = 9.793
E [m^2/s^2]	energy term used in energy equation

f_c [N]	Coriolis force
G_b [Pa/s]	generation of turbulent kinetic energy evolved from buoyancy
G_k [Pa/s]	generation of turbulent kinetic energy evolved from the mean velocity gradients
g [m/s^2]	gravitational acceleration
H [m]	reference height; also z_{ref}
k [W/mK]	thermal conductivity given in energy equation
k [m^2/s^2]	turbulent kinetic energy
k_{FLUENT} [m^2/s^2]	turbulent kinetic energy from FLUENT simulation results
k_o [m^2/s^2]	turbulent kinetic energy given by MO similarity theory
k_t [m^2/s]	turbulent thermal diffusivity of air
L [m]	length of boom/lattice cross-section
L [m]	MO similarity theory length scale
$\bar{L}_b$ [m]	average MO length scale from Horns Rev data set
Ma	Mach number
Nu	Nusselt number
P [Pa]	pressure profile used in MO similarity theory
P_0 [Pa]	reference pressure at the surface; 101325 Pa
Pr	Prandtl number
Pr_t	turbulent Prandtl number used in energy equation
$Pr_{t,wall}$	turbulent Prandtl number at the wall
q [%]	specific humidity
$\dot{q}_w$[W/m^2]	wall heat flux
R [m]	distance from center of boom/lattice to end of the iso-circle formed by an iso-speed plot
R [kgK/J]	gas constant of air
Ra	Rayleigh number
Re	Reynolds number
$Re_{x,cr}$	critical Reynolds number for transition to turbulence (= 5e5)
R_B	bulk Richardson number formulation excluding potential temperature effects
Ri_B	bulk Richardson number formulation including potential temperature effects
Ri_g	gradient Richardson number formulation
S_h [Pa/s]	other energy source terms in energy equation
S_k [Pa/s]	kinetic energy source terms
S_ε [Pa/s^2]	dissipation rate source terms
T [K]	absolute temperature
t	boom/lattice solidity
T_o [K]	temperature profile given by MO similarity theory
T_{op} [K]	absolute operating temperature (= T_w)
T_{ref1} [K]	absolute temperature at first reference height
T_{ref2} [K]	absolute temperature at second reference height
T_w [K]	wall temperature or water temperature
T_* [K]	turbulent temperature used in MO similarity theory
U or u [m/s]	velocity from MO profile or measured velocity
u,w,v [m/s]	velocities along the Cartesian axes x, y, z

u_{15} [m/s]	average velocity profile for Horns Rev data set at 15 m
u_d [m/s]	wind speed deficit
u_{NE} [m/s]	wind speed measured from the northeast
u_o [m/s]	velocity profile using MO similarity theory
u_{ref} [m/s]	reference velocity
u_{SW} [m/s]	wind speed measured from the southwest
u_* [m/s]	friction velocity
$\overline{u_{*o}}$ [m/s]	average MO friction velocity for Horns Rev data set
u_∞ [m/s]	velocity used to find flow parameters, (= $u(y_{top})$)
V_{LOS} [m/s]	speed of atmosphere using LiDAR devices
x,y,z [m]	Cartesian coordinates or FLUENT grid point
x_{cr} [m]	critical distance from leading edge where transition to turbulence occurs
y_i [m]	height of boundary layer
Y_M [Pa/s]	effect of compressible turbulence found between the fluctuating dilatation and the total dissipation rate
y_{top} [m]	height of simulation domain
z_0 or z_o [m]	surface roughness length or sea roughness length
z_{ref} [m]	reference height
z_{ref1} [m]	distance from surface to first temperature measuring height (= 0 m)
z_{ref2} [m]	distance from surface to second temperature measuring height (= 55 m)
z_U [m]	distance from surface to a velocity measurement height
z_θ [m]	distance from surface to a temperature measurement height
Mathematical Operators and Constants	
Δ [m]	cell center width
Δ	difference operator
Δx [m]	primary flow direction mesh spacing
Δy [m]	vertical mesh spacing
Δz [m]	cross flow direction mesh spacing
∇	gradient operator
$\frac{\partial *}{\partial *}$	partial differential operator
$\frac{d*}{d*}$	differential operator
Miscellaneous Notation	
i (index number)	i = x = 1, i = y = 2, or i = z = 3
‘ (prime)	(lowercase letters with primes) fluctuating (RMS) component in a Reynolds decomposition
‘ (prime)	SGS scale used in the LES method
~ (tilde)	instantaneous quantities
$\bar{}$ (overbar)	resolved large eddy scale used in the LES method or time-averaged component
(capitalized variable)	time-averaged component

1 Introduction

With the inclined electricity demand of residential and commercial sectors, permitting of new power generation projects is evident. However, global warming and pollution concerns have conduced to legislative action controlling emissions of coal- and gas-fired power plants, which limits the total annual global power production. So how will the global energy sector meet the heightened electricity demanded by countries and their residents? One of the answers to this trite question is—the power generation industry can focus its crosshairs on wind energy projects to fulfill any electricity production shortfalls.

Germany led in total wind power until recently producing nearly 21 GW in 2006 (Efiong, 2007). The German country now holds the bronze medal for its wind energy infrastructure totaling more than 27 GW in 2010 (IEA Wind, 2011). Interestingly also in Europe, Denmark has become the landmark for most domestically consumed wind energy, 22% , and has contributed the second largest investment to global offshore wind power, 30% of all offshore construction. Famed Danish offshore wind farms include Horns Rev I and II, Nysted, Middelgrunden, and Vindeby, to name a few. The newcomer, China, of late amazingly maintains the lead in total wind power capacity—over 44 GW in installed wind power in 2010 amounting to roughly 17 times that which the country had permitted by 2005 (IEA Wind, 2011 & Efiong, 2007). The US lags behind the frontrunner with a total capacity of over 40 GW in 2010 where the Lone Star State holds the accolade for the largest national wind resource development, more than 10 GW (IEA Wind, 2011).

Major strides have been taken in the offshore wind energy research and development arena with knowledge that offshore winds at hub height are stronger than winds onshore placed at heights approximately near sea level. Taking advantage of the marine wind behavior increases the potential annual energy production of a proposed wind farm (Moskalenko *et al*., 2010). Assessing the local ambient conditions such as the wind behavior and the thermal stability is the precursor to quantifying the average annual energy production of a new offshore wind farm site. Before construction of a wind farm commences, a comprehensive site assessment must ensue to mollify stakeholders' apprehensions about the wind farm's forecasted power production, cabling costs, and public opinion. Public opinion is pacified by placing wind farms 10-15 km offshore. This fetch distance is also beneficial to the wind farm siting because the sea surface has a constant roughness unlike locations near the coast and onshore, which are characterized with elevation changes that cause slowdown effects and acclivity in turbulence of the ambient wind, subsequently increasing the loads on the wind turbine and decreasing the power potential (Neckelmann & Petersen, 2000). Cabling costs are minimized by placing wind farms in shallow waters near coastal city hubs, which provide an electricity nexus to hook into from offshore (Musial & Ram, 2010). Potential power production at a site is elevated by quantifying the offshore wind behavior and determining nominal trends such as the seasonal wind speed frequency, wind magnitude, wind direction, turbulence intensity, thermal stratification, and wind speed profile as a function of marine roughness height. Taking into account the marine roughness and the thermal stability of a potential wind farm site can highlight excursions from the classic logarithmic wind profile. The deviations associated with a site's ambient thermal stability have been reformulated in a

non-linear theoretical atmospheric boundary layer similarity theory first derived by Monin and Obukhov and replaces the typical logarithmic wind profile expression (Monin & Obukhov, 1954). This theory is employed to generate the initial conditions of the steady k-ε ABL simulations and to compare the accuracy of the ambient wind profiles using CFD to those constructed with MO theory.

The prime example of an offshore wind farm site that fits the model of a lucrative and well-resourced site is Denmark's Horns Rev I located 14 km offshore from Jylland (Jutland) in the shallow reef waters of Horns Rev. Unadulterated by inhomogeneous sea roughness from the North, West, and South directions, the ambient wind has an annual average wind speed range of 9-12 m/s. This wind farm is co-owned and -operated by DONG Energy and Vattenfall. This site has been in operation since 1999 and studied since 1998. Data acquired by the owners from the met mast, M2, constructed a year prior to the development of the Horns Rev farm is proprietary; however, Elsam Engineering (now DONG) has generously provided research groups such as Risø-DTU access to this information, which has resulted in an influx of public case studies in all areas of wind energy resource assessment.

Additional data acquired at the Horns Rev site by these same research groups using ancillary flow measurement technologies, namely LiDAR and SoDAR, has led to combined data sets that generate wind profiles of the Horns Rev site as well as other locations of interest at heights above traditional hub heights and illuminate outlying behaviors that deviate from current atmospheric boundary layer (ABL) theory in the outer layer.

A relic—turbulent boundary layer theory has proved reliable surviving contemporary research and remains a keystone of CFD models. With this link, RANS equations are transformed to approximate turbulent flows by using the large eddy equations (also known as large eddy simulation (LES), which models the largest turbulent structures, whilst the small scale turbulent structures are estimated using an eddy viscosity) or by using the k-ε closure equations. Corrections to the turbulent eddy viscosity profile or the velocity and temperature profiles to include thermal stability (Monin-Obukhov (MO) boundary layer similarity theory), marine roughness height, and Coriolis forcing factors is standard. These alternative formulations of the turbulence equations assist CFD solvers when processing the turbulent RANS equations and are capable of generating representative site ambient profiles corresponding to measured data.

In this paper, a steady 2D and 3D k-ε model is devised to assure consistency of the average flow variables of velocity, temperature, TKE, and TDR, which have been derived initially from MO similarity theory inclusive of thermal stability. This research produces the necessary steps to customize a k-ε steady code capable of modeling an ABL with thermal effects. The codes are limited and cannot predict the developing 3D dynamics of a turbulent ABL such as vortices and streaks. Additionally, the boundary conditions are proposed only to model ABL flows without inhomogeneities like varying roughness, changes in terrain, or flow around structures. It is remembered that steady k-ε method ABL simulation results can be used as precursors to LES-ABL simulations to reduce the computational time. Other applications of steady k-ε ABL simulations are pollution dispersion, building and industrial flow, and wind farm wake modeling. But only after a secondary set of boundary conditioning is prescribed can these applications be simulated.

The results from this author's novel k-ε code are compared to a verification study conducted by Alinot & Masson (2005) and to data acquired by met mast and LiDAR measurements at Horns Rev for the purpose of quantifying the neutral and unstable wind conditions at Horns Rev (Peña *et al*., 2008). Prior to the 'Results' section, the general site ambient conditions at Horns Rev are accentuated followed by the fundamentals of turbulent boundary layer theory and MO similarity theory. Highlighted next are the specifications and solution methodology of the customized k-ε method constructed in FLUENT 6.3, which is utilized to compute the modeled wind profiles that are displayed in the 'Results' section. A 'Limitations of the Customized k-ε Code' section is provided before the concluding remarks. Auxiliary material is detailed in the appendices at the end of the manuscript.

2 Meteorological Measurements at Horns Rev

The Horns Rev site is located in the Danish waters of the North Sea approximately 14 km west of Jylland (Jutland) and consists of a shallow reef from which its namesake Horns Rev, or Horns Reef, originates. The water depth range is 6-12 m below sea level (BSL). A meteorological mast known as 'M2' was constructed in 1999 after approval from the Danish Government and funding from the owners of the mast, then Energi E2 and Elsam Engineering and now Vattenfall and DONG Energy, was obtained. The purpose of M2 is to collect atmospheric data that determines the wind behavior and thermal stability as well as other ambient conditions near the proposed Horns Rev wind farm, which was slated to connect to the Danish electricity grid in late 2002. The Horns Rev wind farm and reef along with M2 are shown in the figure below (Neckelmann & Petersen, 2000).

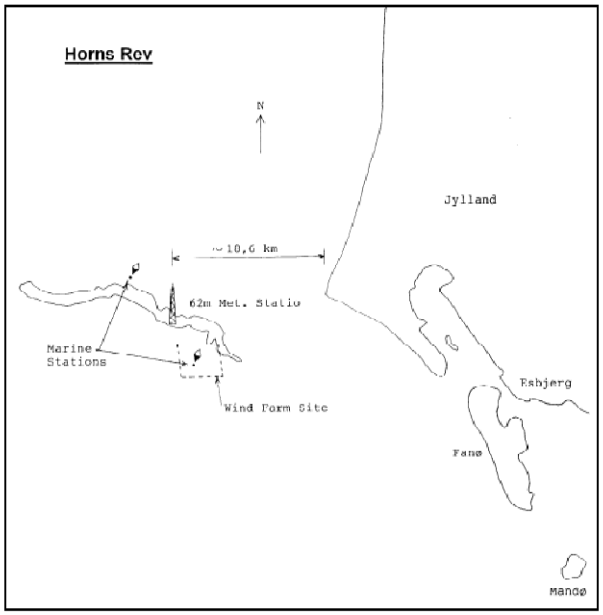

Figure 2.1: Horns Rev site description.

From the collection of meteorological measurements, one is able to quantify wind and thermal statistics such as the average wind profile, thermal stability, turbulence behavior,

wind frequency and direction, and seasonal or diurnal variations of these characteristics. These trends are illustrated in this chapter to identify the wind conditions and thermal stability at the reef and to understand how the wind profile at Horns Rev deviates from the classic logarithmic wind profile for various thermal stability classes.

2.1 Data Collection at M2

The data collection at M2 consists of recordings from cup anemometers among other types of measuring equipment such as thermometers, wind vanes, pressure sensors, etc. These components are discussed in the next subsections.

2.1.1 Cup Anemometers

Shown in Figure 2.2 from Neckelmann & Petersen (2000), M2 is a square lattice mast that sits atop a shallow monopile base and stretches above sea level (ASL) to 62 m.

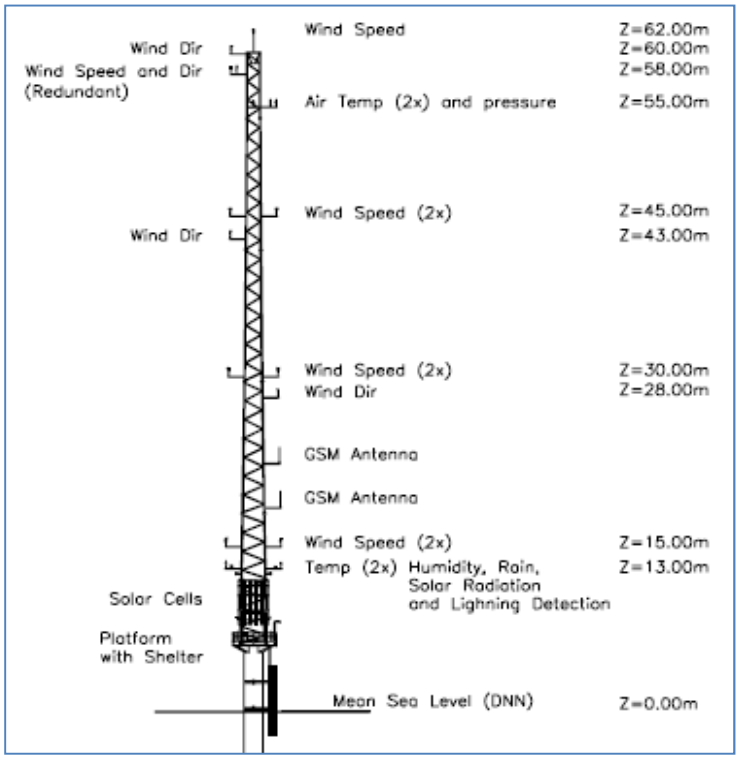

Figure 2.2: Measurement setup on M2.

At four heights, 15, 30, 45, and 62 m ASL, the met mast is fitted with two-sided, boom-mounted cup anemometers that extend from the mast at each given measurement level except for the top height, where a single cup anemometer stretches from the tip of the lattice construction (Neckelmann & Petersen, 2000).

Installing anemometers on both sides of the tower reduces the shadowing effect caused by the wake of the wind flowing past the mounting boom and lattice pieces nearest the anemometers. This type of shadowing effect is known as non-direct flow distortion. The measurement error associated with each structural piece is quantified and found to represent the following deviations: 2% for boom shadowing and 2% for lattice shadowing. Both errors generate a wind speed deficit or increment in the measurements depending on the relative angle between the wind flow and the boom/lattice position. Lattice effects are completely remedied with the two-sided assembly along with use of data collected from anemometers on the upstream side of the wind flow. As for the boom anomalies, post-processing algorithms and empirical standards are created to correct the flow distortion error (Pederson & Wagner, 2011).

Another measurement imperfection is the speedup effect found at top-mounted anemometers. These effects are revealed by Perrin *et al*. (2007) and cause deviations of near 2%. Further, to alleviate speedup errors at top-mounted anemometers, it is suggested to place the equipment lifted five top lattice diameters above the structure.

Lastly, direct flow distortion caused by the bulk geometry of the mast itself at various wind directions is studied by Hasager *et al*. (2007) at M2. For wind directions between

50-100° and again at 250-300°, where the direction is taken as 0° from N and rotates clockwise, the relative cup anemometer wind speed variation, u_{SW}/u_{NE}, is shown to total between 22-30%. Higher variations are exhibited when the wind is blowing from the southwest, -30%. Data that correspond to the direct mast shade window is excluded from final processing. Hasager *et al*. (2007) illustrates both the wind speed variation of the non-direct flow distortion as a function of the wind direction, θ, and the dimensionless wind deficit and/or increment, u_d, (see Appendix A for computation details), of the direct flow distortion at M2 as a function of relative flow angle measured between the boom/lattice and the wind direction, θ_{rel}, respectively, in Figure 2.3.

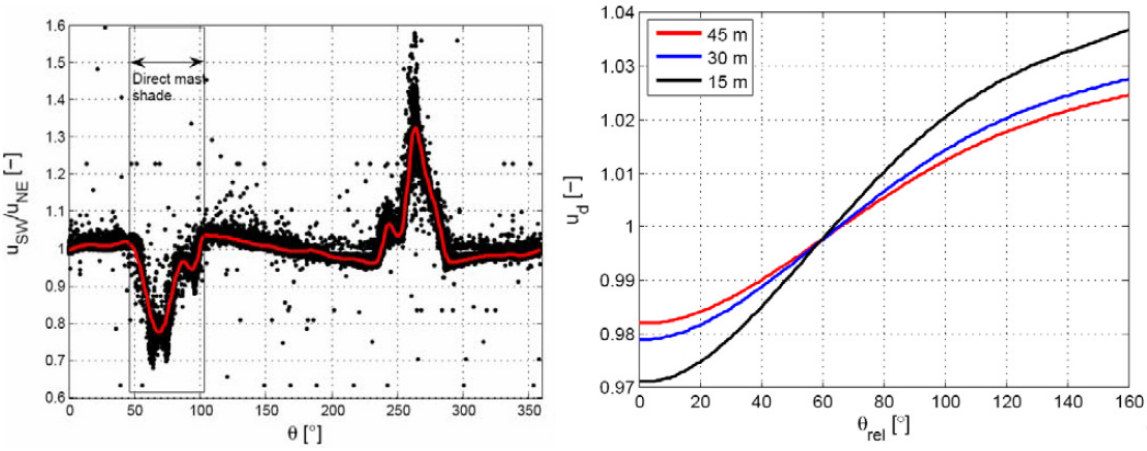

Figure 2.3: (Left) Direct flow distortion. (Right) Non-direct flow distortion.

A similar depiction of the non-direct flow distortion with the open sea, land, and wake sector labels highlighted is provided in the Figure 2.4 from Peña *et al*. (2009). The wake region is the area where wakes are generated as the wind blows through the wind farm from the eastern and southern directions toward M2. The open sea sector is the northwesterly direction where no coastal roughness effects alter the wind profile.

The land influenced region is where elevation changes from the coast affect the wind profile from easterly directions. These regions are viewed in the pie chart right of the figure.

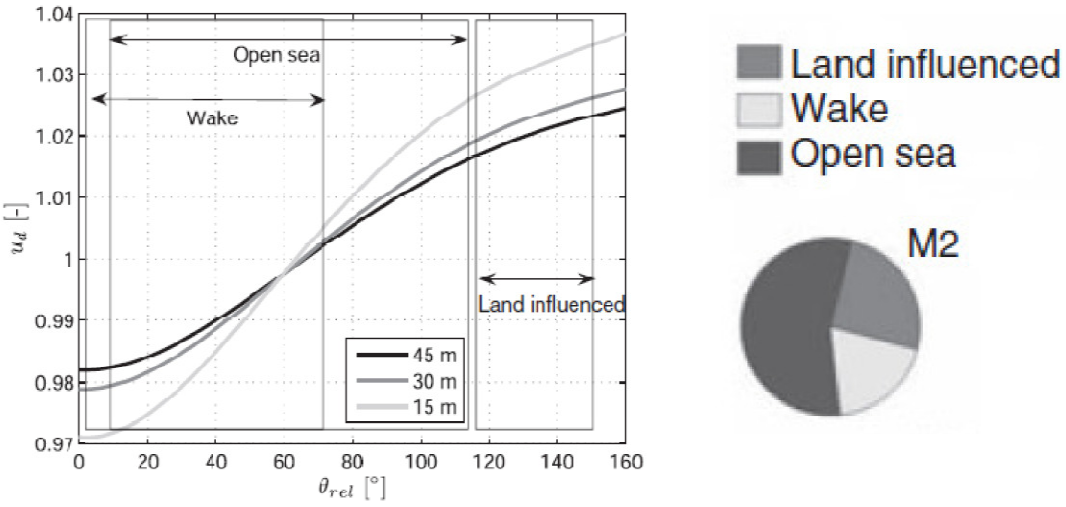

Figure 2.4: Non-direct flow distortion.

2.1.2 Other Measuring Equipment at M2

Other observational equipment on M2 consists of three wind vanes at 28, 43, and 60 m ASL; a 3D sonic anemometer at 50 m ASL that can measure the sensible heat and momentum fluxes directly; thermometers at 4 m BSL and 13 and 55 m ASL; an air pressure sensor at 55 m ASL; an air relative humidity sensor at 13 m ASL; a solar radiation sensor at 13 m ASL; and a rain detector at 13 m ASL. As an aside, the latent heat is not explicitly computed in this paper when determining the atmospheric conditions at Horns Rev using met mast data. The data logged is wind speed, wind direction, temperature, atmospheric pressure, solar radiation, lightning detection, relative humidity, rain, and sensible heat and momentum fluxes. The met mast and sensor setup were shown previously in Figure 2.2 except this figure excludes the temperature sensor at

4 m BSL (Neckelmann & Petersen, 2000). The redundant wind speed, wind direction, and atmospheric pressure sensor at 58 m ASL functions as a secondary measurement set to which validation of the near sensor observations are compared. This sensor is also employed in extreme cases when the primary sensors nearby are malfunctioning or disabled. The cup anemometers sample at a rate of 1 Hz, while the sonic anemometers employ a rate of 20 Hz. It is also noted that all measurement systems demarcate the logged data into 10-minute averages that include minimum, maximum, and standard deviation in each 10-minute recording.

The difference between cup anemometers and 3D sonic anemometers is the ability of the sonic anemometer to collect wind speed fluctuations in three dimensions; thus, the turbulence profiles of u, v, and w are measured (Pedersen & Wagner, 2011). See Figure 2.5 below for another rendition of the observation sensor placement and recall that cup anemometers are mounted on either side of the mast and that a temperature sensor is placed at 4 m BSL since these items are not shown (Hansen, 2001).

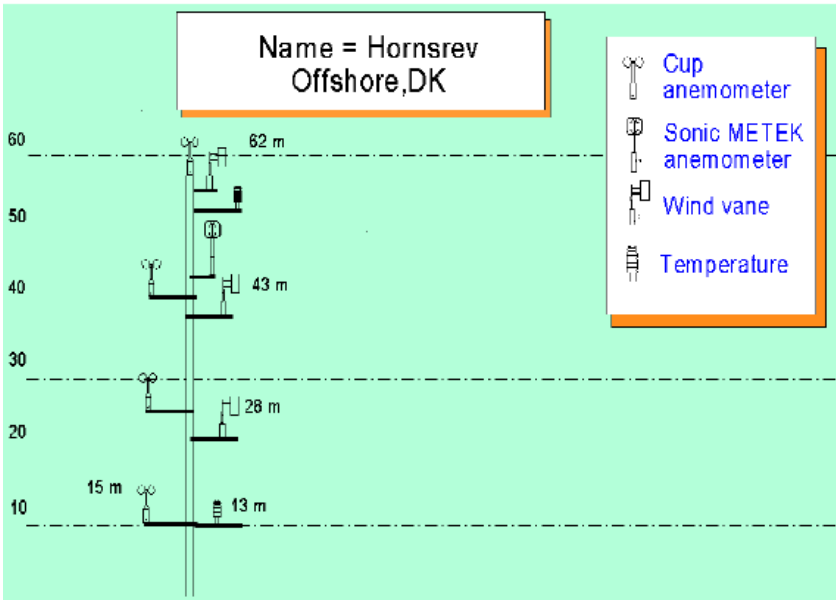

Figure 2.5: Measurement setup on M2.

2.2 A Review of Horns Rev Observations—1999-2007

Observations analyzed by Neckelmann & Petersen (2000) and collected from May 1999 to January 2000 at the Horns Rev met mast M2 establish a basis for evaluation of the wind conditions in the region. It is worth noting that this data set is one of six that will be presented subsequently as a nine-year review of Horns Rev data campaigns which point out the seasonal wind and temperature trends as wells as the thermal stability.

The additional records cover the following periods:

1. September 1999 to May 2001 (Hansen, 2001)
2. May 1999 to November 2002 (Tech-Wise, 2002)
3. October 2001 to April 2002 (Tambke *et al.*, 2003)
4. July to October 2004 combined with May to October 2006 (Peña *et al.*, 2008)
5. 1999-2007 (Larsén *et al*., 2011)

2.2.1 Neckelmann & Petersen (2000) Observations

Notwithstanding a powerful winter storm on December 3, 1999, which forced the mast to go ten days without power, and an inoperable top sensor after a lightning strike in October 1999, the observations from the M2 measurement system are largely available for the entire period. There are more than 6400 hours of data logged at a sampling rate of 1 Hz. Neckelmann & Petersen (2000) claims the following limitations should be considered when perusing the data:

1. The period is not an annual outlook of the site, but about 8 months.

2. Historically, the data collected in 1999 is uncharacteristically "poorer" than usual wind data viewed for the site, i.e., the winds are atypically lower than previous years.
3. No correction for boom flow distortion is conducted on the data since it represents a nominal speedup of less than 1%.
4. As previously mentioned, lattice flow distortion is completely remedied by selecting data from the upwind side of the mounted sensors.
5. Changes in the mean sea level due to the tide at the mast are not accounted for in the data, which could help point out speedups or slowdowns in the wind profile dependent on the sea level.

The following nominal data is processed using 10-minute averaged data bins sampled initially at 1 Hz and is displayed in Table 2.1 from Neckelmann & Petersen (2000). Wind direction is not provided at 15 m ASL since there is no wind vane in the vicinity contrary to the three other measuring heights with neighboring wind vanes nearby.

Table 2.1: Mean data at Horns Rev from May 1999 to January 2000.

Height		62	45	30	15
Mean Wind Speed	[m/s]	9.7	9.2	8.8	8.2
Max. Wind Speed	[m/s]	45.4	43.1	40.7	39.5
Mean Wind Direction	[°]	194.9	194.7	195.3	-
Mean Turbulence Intensity	[-]	0.088	0.097	0.101	0.119
Weibull Scale Parameter	[m/s]	10.9	10.4	10.0	9.3
Weibull Shape Parameter	[-]	2.2	2.2	2.2	2.2
Wind Shear (to nearest)		0.16	0.10	0.10	-

Notably, Table 2.1 illustrates the use of the Weibull distribution since the wind speed statistics of the data set are best described by this shape viewed on the next page in Figure 2.6. The focal points of Figure 2.6 establish the site wind behavior at 62 m ASL: peak winds range from 8-11 m/s and more frequent winds blow out of the westerly

direction sectors. It is noted that each concentric dashed circle represents 5% frequency of occurrence in the wind rose image in Figure 2.6 with the first circle equating to 5% and the last 15%. These characteristics supplement the presupposition that more frequent winds are generated at larger distances from land due to the weakened surface resistance of marine atmospheres, which equates to heightened flow speeds. It is cautioned that the two images in Figure 2.6 from Neckelmann & Petersen (2000) are only a crude representation at best of the most frequent occurrences of wind speed and wind direction.

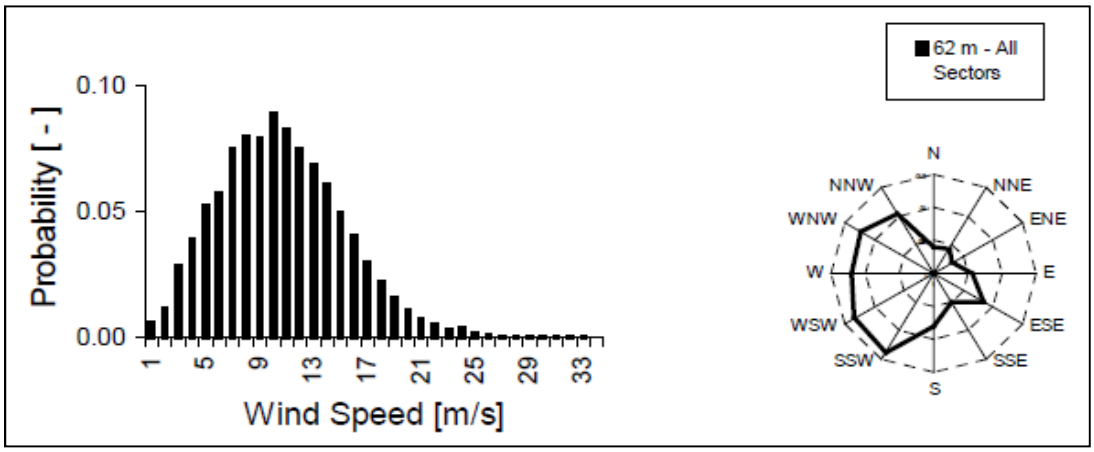

Figure 2.6: (Left) Wind speed probability distribution. (Right) Wind rose at 62 m ASL.

Further delineation of the percentages of occurrence of each wind speed beset in the wind rose has not yet been accentuated by any of the aforementioned authors who have post-processed data from Horns Rev except Tech-Wise (2002), which is viewed in Figure 2.19 detailed in the next section. Neckelmann & Petersen (2000) spotlight the nominal wind speed directional trend in Figure 2.7 as well as the increase in wind speed with height. In the westerly regions, fetches from land in the Baltic Sea from eastern England are thousands of kilometers away and have little effect on the marine surface roughness and wind profile, while the distance from the land in the easterly sectors is about 10 km

from Jutland, Denmark causing a stronger resistance behavior to develop in the wind profile approaching from this direction.

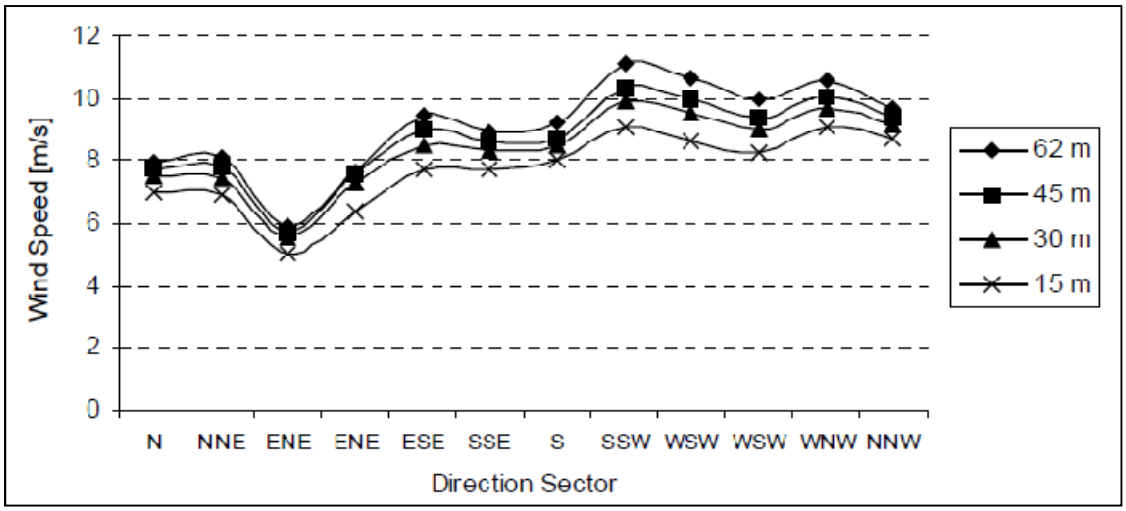

Figure 2.7: Wind speed vs direction sector at all observation heights.

Figure 2.8 below displays the mean wind profile of the observations in a semi-logarithmic plot from Neckelmann & Petersen (2000). To truly follow the token logarithmic profile, the data would exhibit a linear behavior; however, there exist a deviation, a speedup, in the data between the third and fourth measuring heights.

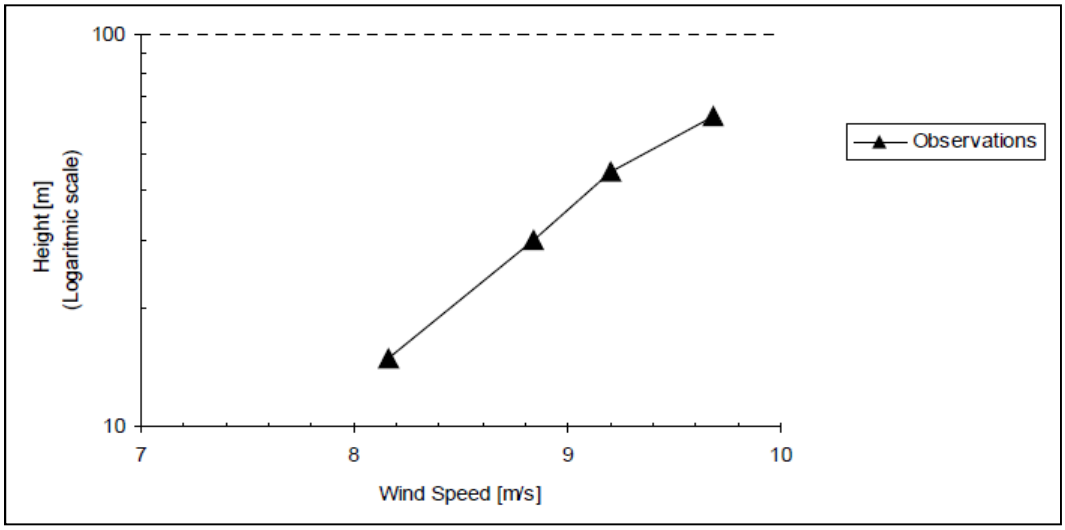

Figure 2.8: Semi-log plot of height vs wind speed.

This speedup meme is found by other Horns Rev research campaigns, such as Tech-Wise (2002), Tambke *et al*. (2003), and Nissen & Gryning (2009). Peña *et al*. (2008) suggests improvements to the logarithmic wind profile, which will be elucidated in greater detail later and include a thermal stability and Charnock roughness correction.

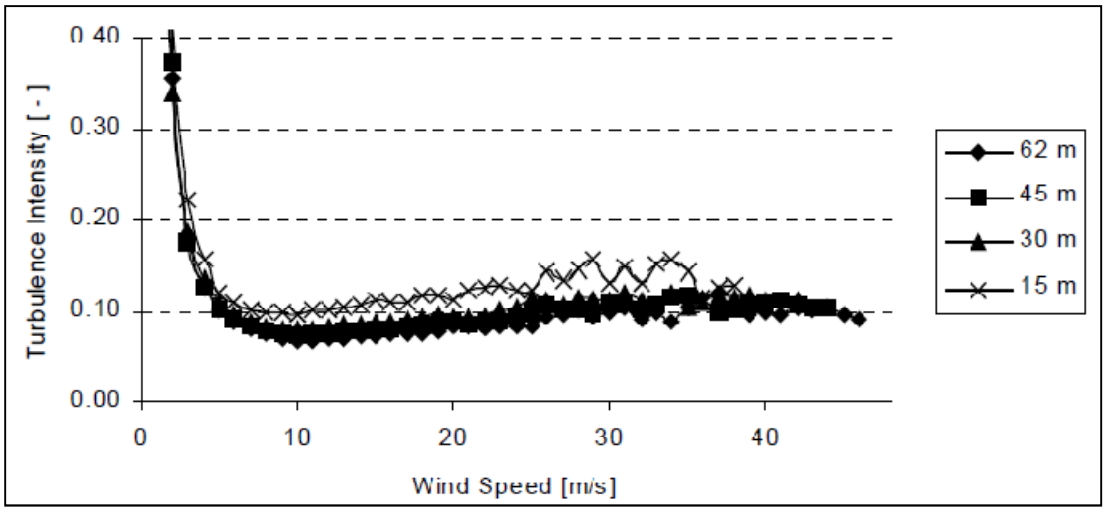

Figure 2.9: Turbulence intensity vs wind speed.

The turbulence intensity at Horns Rev is viewed in Figure 2.9 above from Neckelmann & Petersen (2000). Turbulence intensity is defined as the ratio of the standard deviation of wind speed to the wind speed of each 10-minute averaged recording, and finally these turbulence intensity bins are separated according to height in 1 m/s wind speed intervals. Turbulence intensity is computed from cup anemometer recordings, which have logged the minimum, maximum, and standard deviation of each 10-minute averaged wind speed recording. Illustrating the typical trend for atmospheric flows, the data commences at a maximum intensity for smaller nominal wind speeds, decrease to a minimum between 8-12 m/s, and moderately increases with wind speed after 12 m/s. There is a modicum of difference between the last three measurements at greater heights, while at 15 m ASL an overt but slight rise in the intensity is encountered.

It is proclaimed that this disparity is due to the generation of turbulence caused by the surface roughness. Additionally, the intensity diffuses with greater distance from the surface. The noted scatter at 15 m ASL for the gamut of wind speeds greater than 25 m/s is an artifact of the small number of wind speed records.

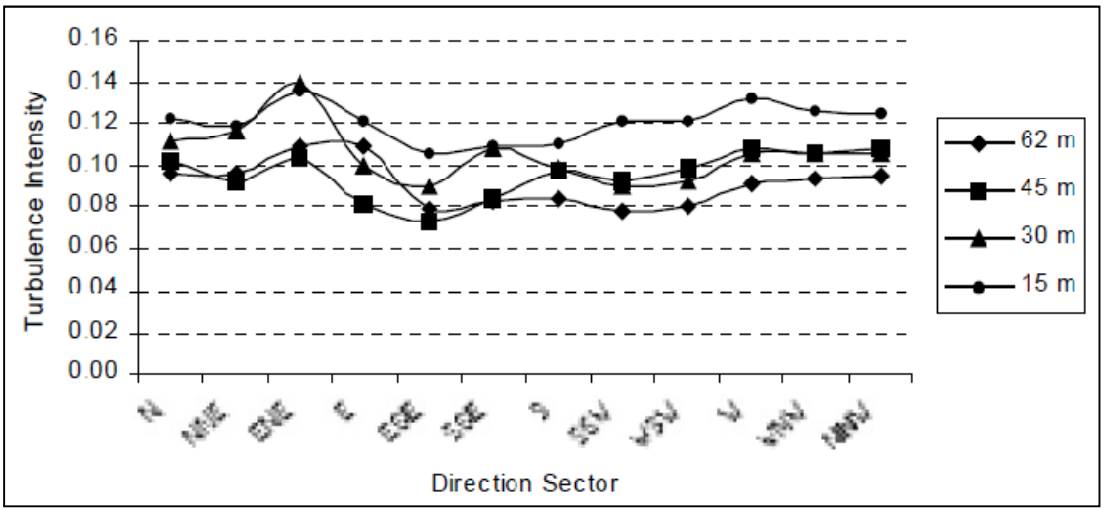

Figure 2.10: Turbulence intensity vs direction sector.

Figure 2.10 above from Neckelmann & Petersen (2000) elucidates that winds traveling from land at shorter fetch distances produce higher turbulence intensities in view of the fact that land tends to comprise larger surface roughness values in contrast to the ocean. Invariably, the winds blowing out of the easterly directions from Jutland show significantly higher intensities, but this trend more often seems to compare similarly to the magnitude of the turbulence intensity in higher wind sectors (see Figure 2.9) such as those characteristic of the westerly directions at 62 m ASL. However, the acclivity in turbulence intensity in the easterly directed sectors is exposed at 30 m ASL measurements and is not comparable to the trend seen in the westerly directions at that same height.

2.2.2 Hansen (2001) Observations

Hansen (2001) prepared an online document of 50 m ASL sonic anemometer observations from M2 for the period September 1999 to May 2001. He includes nominal, probability density, and wind rose plots of the raw data, which is post-processed to highlight sundry site flow characteristics. These plots are given on the next few pages. For nominal plots, each dot is commensurate to 600 seconds.

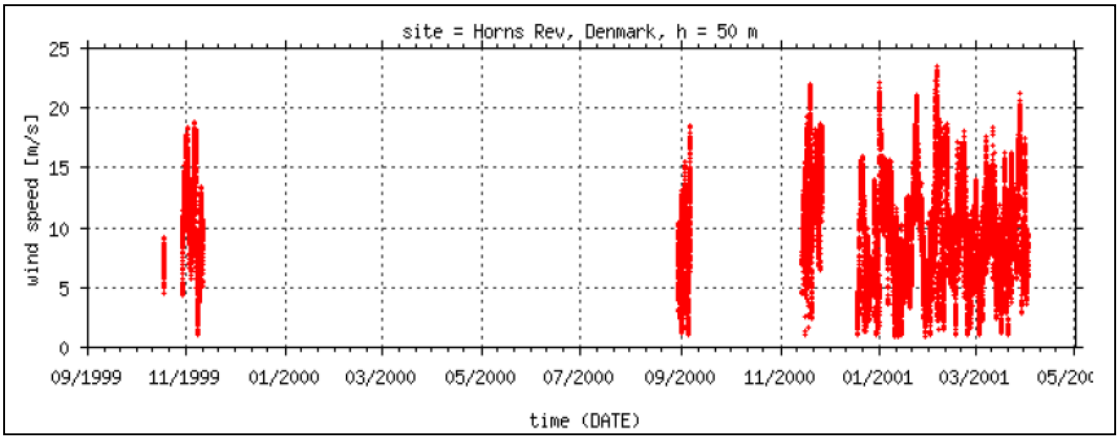

Figure 2.11: Nominal wind speed at 50 m ASL.

After assessing the nominal wind speed at 50 m ASL in Figure 2.11 above from Hansen (2001), the Horns Rev site characteristics for the winter and spring seasons from 12/2001 to 04/2001 are envisioned when considering a crude average behavior of the data highlighted. Recalling that 1999 is referred to as a "poor" wind year by Neckelmann & Petersen (2000) and excluding the data from 2000 since there are fewer measurements in this year, the basic wind speed averages, e.g., roughly the vertical center of the data regions, in 2001 are 13 m/s in early January, 7 m/s in mid-January, 12 m/s in late January, 6 m/s in early February, and a nearly constant 8 m/s from mid February to early April. Therefore, an initial site evaluation of the wind speed trend in winter and spring

seasons at Horns Rev is described as experiencing oscillating periods of local peak to trough winds throughout the winter months with pronounced winds of 13 m/s in early-January and reaching an approximately incessant average through the spring months of 8 m/s.

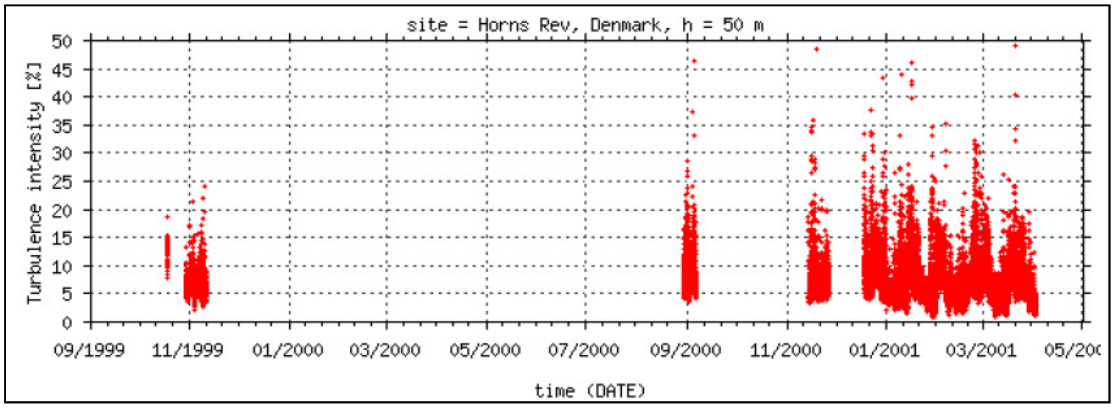

Figure 2.12: Nominal turbulence intensity at 50 m ASL.

Figure 2.12 above from Hansen (2001) describes the nominal turbulence intensity for the same time frame sampled. As is the case with Figure 2.11, oscillating periods from peak to trough commence in the winter during January and February 2001; however, a trough in wind speed in mid-January and early February (see Figure 2.11) corresponds to a peak in turbulence intensity for those same months (see Figure 2.12). Another look at the turbulence intensity versus wind speed proves helpful in explaining why some wind speed troughs may induce larger turbulence intensities.

Figure 2.13 on the next page displays the turbulence intensity versus wind speed for the entire data set at "30 m [sic]"; however 30 m ASL is a typo that should read 50 m ASL since the entire Hansen (2001) collection is solely post-processed for recordings gathered at 50 m ASL. After drawing a solid 10-minute averaged line through the graph whose shape is taken from Tech-Wise (2002), the nominal behavior of the turbulence

intensity at 50 m ASL is premised. It is found that site-specific turbulence intensity at Horns Rev decreases with increasing wind speed from about 10% at 5 m/s, reaches a minimum of 5% at 10 m/s, and then shows a tincture of gain to 7.5% at 15 m/s.

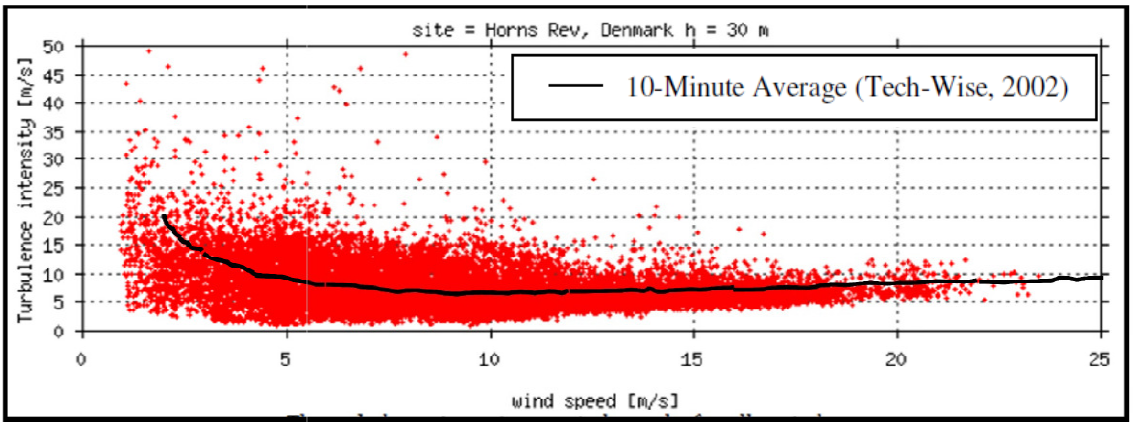

Figure 2.13: Turbulence intensity (Adapted, Hansen, 2001).

Thus, site analysis of the turbulence intensity versus wind speed displays an eccentric condition revealing that some trough wind speeds, i.e., speeds smaller than 10 m/s, generate higher turbulence intensities than the turbulence intensity for wind speeds that are greater than but near 10 m/s. This same shape is illuminated in data collected from May 1999 to January 2000 in Neckelmann & Petersen (2000) shown previously in Figure 2.9.

Figure 2.14 on the following page from Hansen (2001) gives the wind speed distributions for the complete data set at 50 m ASL for speeds greater than and equal to 5 m/s. The aforementioned plot demonstrates that approximately 35% of the wind profile at 50 m ASL (the usual hub height of most wind turbines is 70+ m ASL) corresponds to 6-9 m/s and 20% of the wind profile at 50 m ASL represents speeds between 11-12 m/s, which is where the turbulence intensity is larger than the minimum at 10 m/s and occurs

9% of the time (Hansen, 2001).

Figure 2.15 reinforces the previous plot in addition to Figure 2.13, whereby the Horns Rev wind condition is forecasted to frequently portray a wind profile of 6-9 m/s and 11-12 m/s equivalent to a turbulence intensity between 5 and 7% (Hansen, 2001). These values are slightly lower than those declared in Neckelmann & Petersen (2000), who notes a turbulence intensity between 8 and 10% for wind speeds less than or greater than 10 m/s.

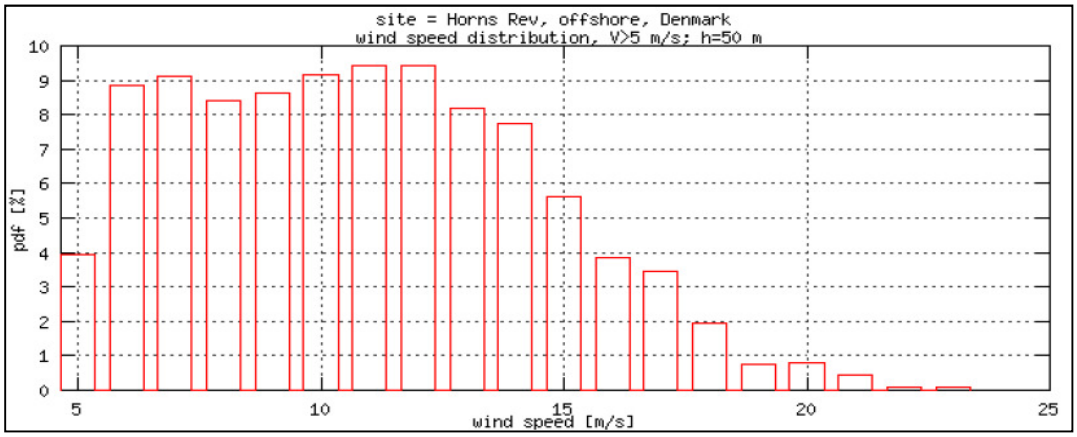

Figure 2.14: Wind speed distribution at 50 m ASL.

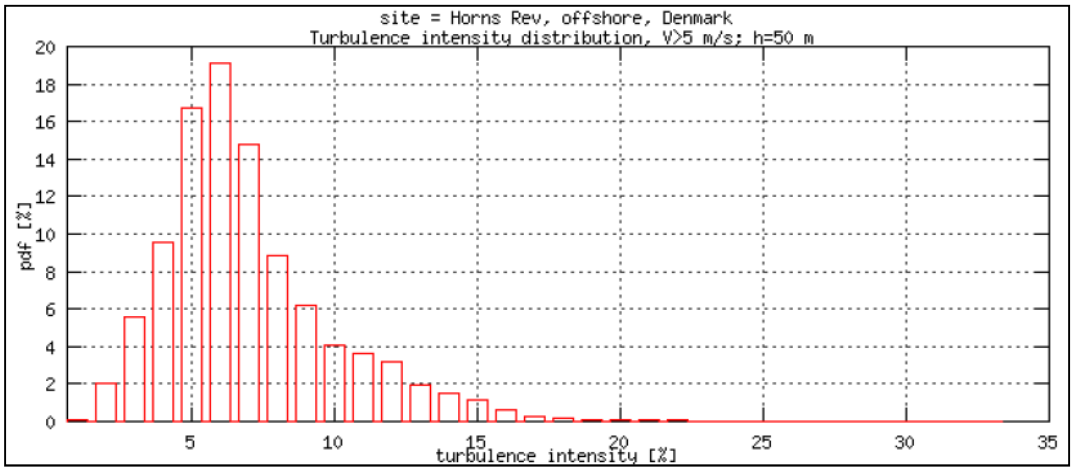

Figure 2.15: Distribution of the turbulence intensity at 50 m ASL.

Finally, Figure 2.16 showcases the wind rose displaying the percent distribution

versus wind direction from Hansen (2001). As previously mentioned, marine winds that are able to develop along the sea surface undisturbed by land and elevation changes, exhibit the highest wind potential. At Horns Rev, these winds blow from the North Sea between the United Kingdom and Norway, approximately 120° with east represented by 0°. The site ambient wind conditions resemble high winds from this angle about 13% of the time. Less frequently, high winds blow in from 150, 180, and 210° (Hansen, 2001).

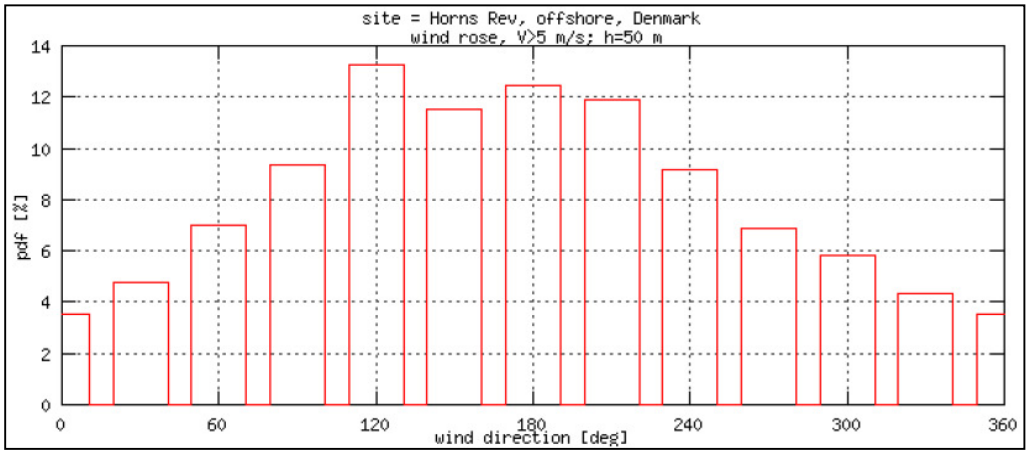

Figure 2.16: Wind rose at 50 m ASL.

2.2.3 Tech-Wise (2002) Observations

Tech-Wise was contracted by Elsam, the owners of M2 at Horns Rev, to assess and report on the data gathered at the site for the period from May 1999 to November 2002. The second of two reports was published in December 2002 and is report number 160949 titled *Wind Resources at Horn Rev*. The data availability is shown in Table 2.2 from Tech-Wise (2002) and highlights a 99.05% primary observational system coverage.

Table 2.2: Data coverage for M2.

Measuring system	Data period	Hours	Data coverage
Primary met. system	May 1999–Nov. 2002	30638	99.05%
Back-up met system	May 1999–Nov 2002	30359	87.99%
Sonic System	October 1999–Nov. 2002	26888	37.35%

The mean 10-minute statistics for the observational period are highlighted below in Table 2.3 from Tech-Wise (2002) at each cup anemometer level.

Table 2.3: Mean 10-minute statistics at M2.

Height		62	45	30	15
Mean Wind Speed	[m/s]	9.46	8.85	8.51	7.89
Max. Wind Speed	[m/s]	45.4	43.1	40.7	39.5
Mean Wind Direction	[°]	254	254	254	-
Mean Turbulence Intensity	[-]	0.079	0.09	0.092	0.107
Weibull Scale Parameter	[m/s]	10.59	10.05	9.64	8.98
Weibull Shape Parameter	[-]	2.3	2.3	2.3	2.2
Wind Shear (to nearest)		0.16	0.10	0.10	-

The average wind speed profile from the observations in Table 2.3 is plotted along with three different logarithmic wind profiles for various surface roughness, z_0, in Figure 2.17 next.

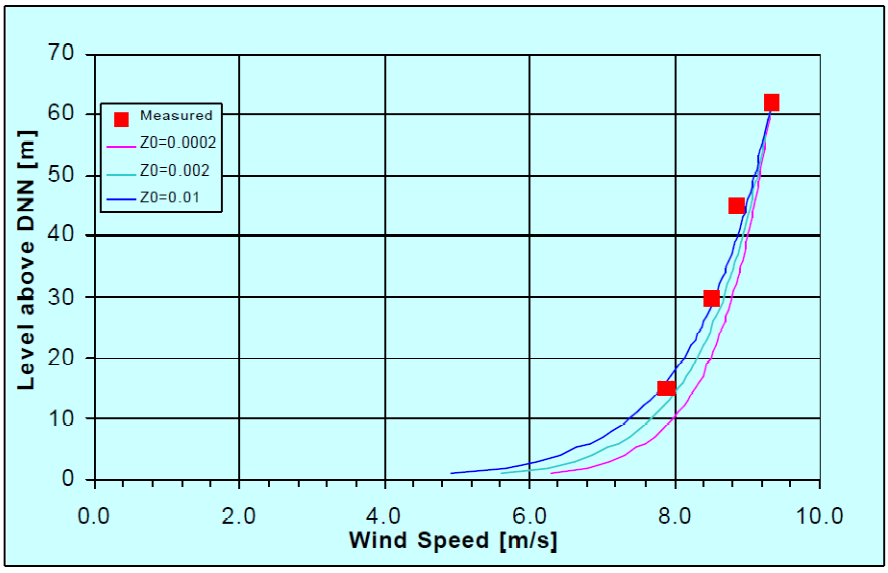

Figure 2.17: Average observed wind speed.

Figure 2.17 illustrates the semblance between observations and the theoretical logarithmic wind profile for $z_0 = 0.01$ m; however, the deviation between theory and observations reveals that the atmospheric data at Horns Rev is not completely explained by logarithmic theory and roughness alone. An error analysis has not been performed.

Additionally, the mean wind speed distribution at 60 m ASL is illustrated concurrently in Figures 2.18 and 2.19 from Tech-Wise (2002). Winds for the most part are out of the westerly directions for the wind speed ambit between 7 to 12 ms^{-1}. In Figure 2.19, each concentric circle represents an increase in frequency of occurrence by 2% with 0% in the center and 14% at the outer-most circle.

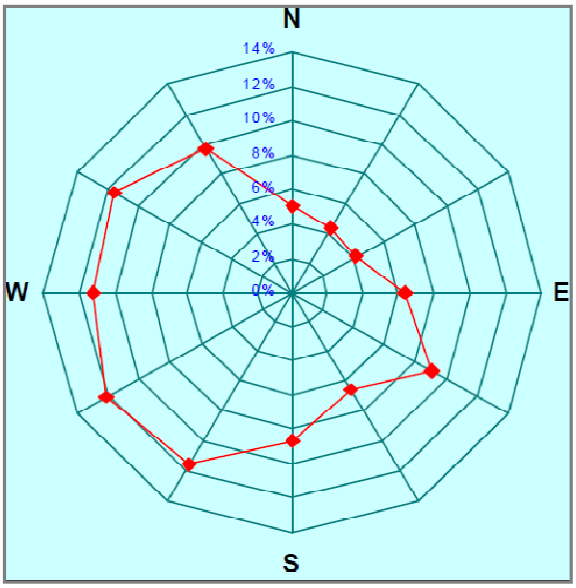

Figure 2.18: Wind direction frequency observed by the wind vane at 60 m ASL.

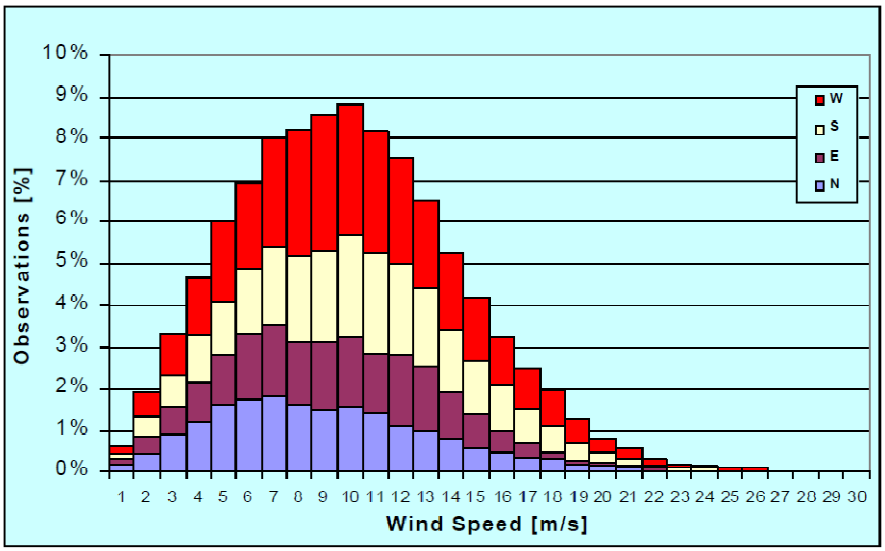

Figure 2.19: Wind speed distribution at 62 m ASL.

The monthly variation of the average wind speed is viewed in Figure 2.20 and reaches a minimum during the spring and summer, April-August, increasing and peaking for the other months in fall and winter. The months comprising October through February are noted as high wind months.

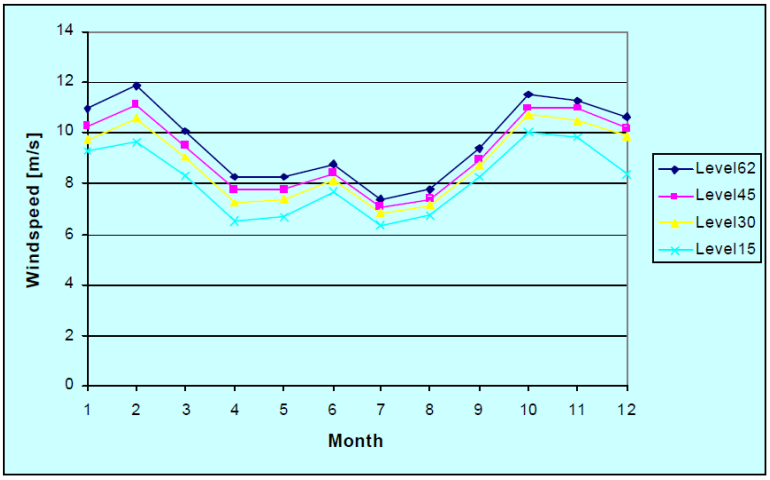

Figure 2.20: Monthly variation of average wind speed.

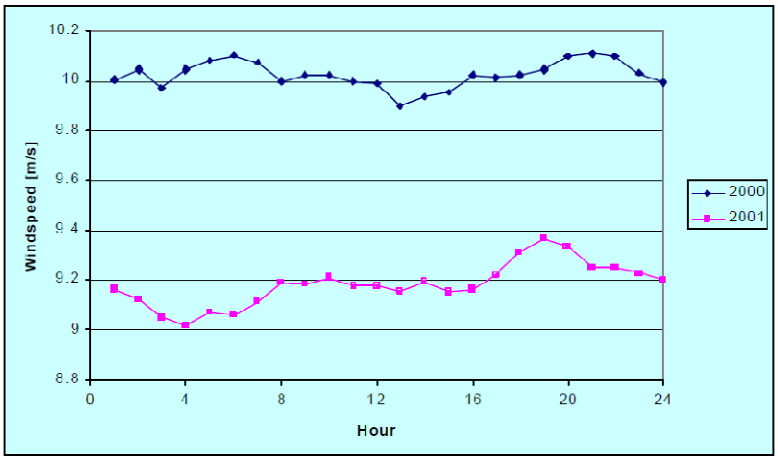

Figure 2.21: Diurnal variation of wind speed at 62 m ASL.

Next, Figure 2.21 above points out the variation in the diurnal average wind speed trend in 2000 and 2001. The Tech-Wise authors did not postulate why the average daily winds were significantly higher in 2000 than those in 2001 by nearly 1 ms^{-1}, but this plot illustrates that some years exhibit poorer winds than other years, which is also indicated

by Neckelmann & Petersen (2000). Additionally, an acclivity in wind speed at night between 5 and 9 pm, or hours 17 through 21, is exposed.

Table 2.4 below from Tech-Wise (2002) displays that the mean turbulence intensity for each wind component, i.e., TI_u, TI_v, and TI_w, follows the trend mentioned in Neckelmann & Petersen (2000) and Hansen (2001) previously. This data represents the average 3D turbulence statistics measured from the sonic anemometer at a sampling rate of 20 Hz processed into 10-minute average data records for a total of approximately 8900 hours. The 3D turbulence intensity is provided in the table below for various wind speeds at a height of 50 m ASL and is computed as the ratio of the standard deviation of each dimension's 10-minute average bin to that same bin's average sonic speed measured in that same dimension. Furthermore, the highest intensities (not shown in Table 2.4), ~11%, are from the northern and northeastern wind directions at 15 m ASL, the first measuring height. The intensities are also high for the northwestern wind directions at 15 m ASL. These results correspond to Neckelmann & Petersen (2000).

Table 2.4: Average 3D turbulence statistics at 50 m ASL.

Turbulence	V=10 m/s	V=15 m/s	V=20 m/s	V=25 m/s
TI_u	6.3%	6.8%	8.2%	8.6%
TI_v	5.4%	5.5%	6.3%	7.0%
TI_w	3.4%	3.6%	4.2%	4.7%

Tech-Wise (2002) also reports on the seasonal temperature variation at Horns Rev, which is later employed to derive the atmospheric stability at the reef. For example, the ambient air temperature distribution at 55 m ASL in 2001 is provided on the next page for 10-minute averaged records. It should be noted that "degree centigrade" is the unit along the abscissa and is a former name for degree Celsius. Also, "pct" stands for

percent or percentage and is the unit along the ordinate. A large number of observations records the ambient temperature as 5-7 and 14-15 °C, which represents winter/spring and summer, respectively. The seasonal and monthly thermal behavior is supplied in Figure 2.23 next. However, Figures 2.22 and 2.23 are only a crude representation of the seasonal temperature trend since the monthly frequency of the temperature is not illustrated by Tech-Wise (2002).

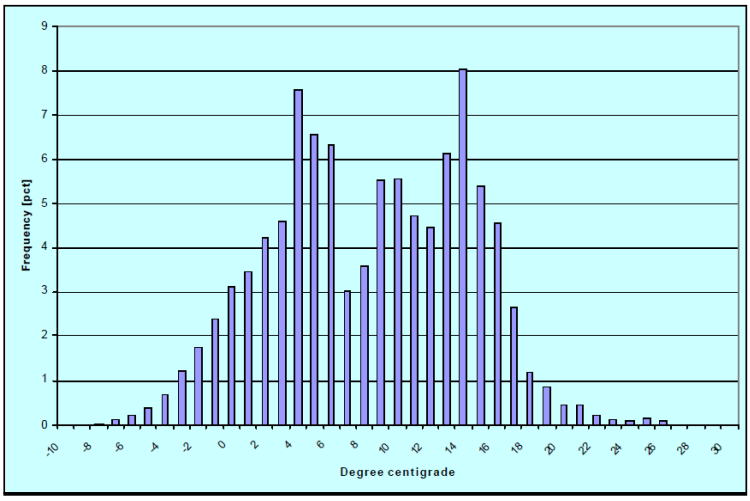

Figure 2.22: Temperature distribution at 55 m ASL for 2001.

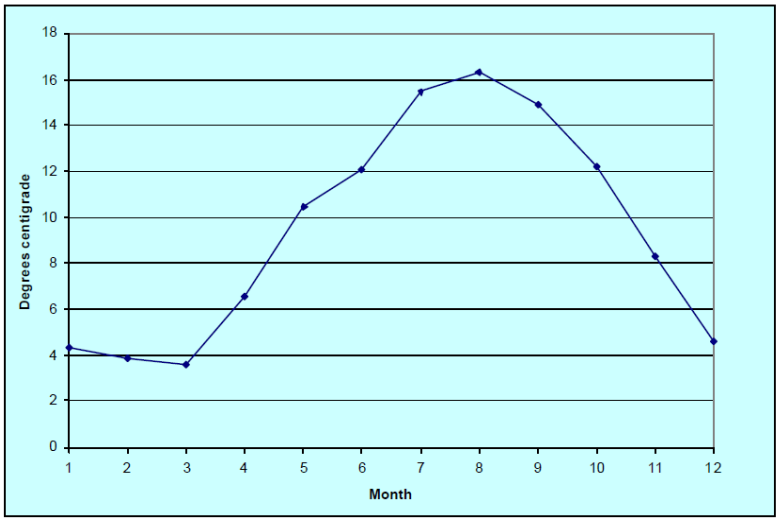

Figure 2.23: Monthly mean temperature at 55 m ASL.

The following figure demonstrates that the daily average temperature increases from sunrise to sunset, 8 am to 5 pm, while the ambient conditions decline after sunset from 5 pm to 8 am.

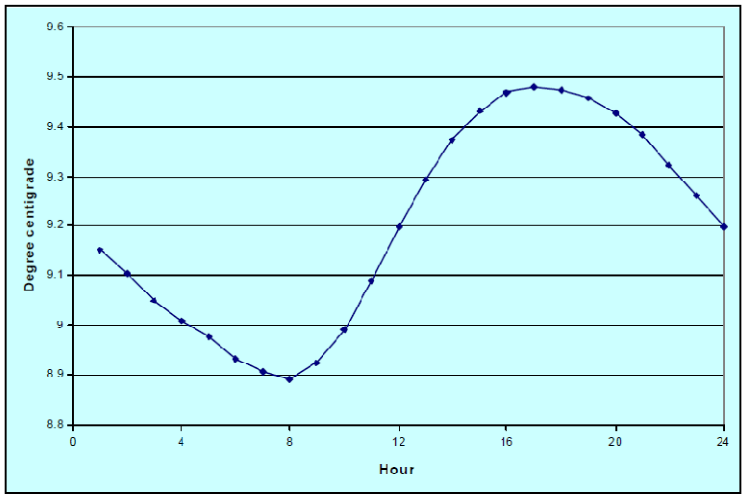

Figure 2.24: Daily variation of mean temperature at 55 m ASL.

With knowledge of the velocity and temperature at various heights at Horns Rev, Tech- Wise performs a stability analysis using the bulk Richardson number, $Ri_{B,Tech-Wise}$, for temperatures measured at 13 and 55 m ASL and wind speeds observed at 15 and 45 m ASL.

The bulk Richardson formulation is given by

$$Ri_{B,Tech-Wise} = \frac{g}{T}\frac{\Delta T}{\Delta z}/(\frac{\Delta U}{\Delta z})^2, \quad (1)$$

where g is the gravitational acceleration, T is the temperature at the greater of the two measuring heights, z is the height, U is the mean wind speed, and Δ is the difference between the associated variable at 15 and 45 m ASL for wind speed and 13 and 55 m ASL for temperature. The stability review is given in the next table and comprises 11,550 hours of wind speeds between 5 and 25 m/s.

Table 2.5: Stability distribution from May 1999 to December 2002.

Stability	Interval	Distribution
Very stable	$0.12 = Ri < 1$	37%
Stable	$0.045 = Ri < 0.12$	11%
Near neutral	$-0.06 = Ri < 0.045$	9%
Unstable	$-0.30 = Ri < -0.06$	12%
Very unstable	$-2.00 = Ri < -0.30$	31%

Results demonstrate that the atmospheric stability is either very stable (37%) or very unstable (31%), which seems to meander from other authors' stability results, i.e., Tambke *et al.* (2003), Peña *et al.* (2008), and Larsén *et al.* (2011). These authors have evidenced a largely unstable, convective atmosphere as characteristic of Horns Rev, but not necessarily very stable. The choice of formulation for the bulk Richardson number in the Tech-Wise report could be the reason for the uncharacteristic results (Sathe, 2010), and auxiliary forms of the equation are provided in Larsén *et al.* (2011) whose stability analysis has established the metric in this manuscript and is discussed in a forthcoming section.

2.2.4 Tambke *et al.* (2003) Observations

Tambke *et al*. (2003) describes the wind condition at Horns Rev as well as performs a stability analysis using M2 measurements collected during the winter and spring seasons from October 2001 to April 2002. This data is supplied as a juxtaposition to the aforementioned observation studies. Displaying the wind directional trend, which is a useful tool to ascertain the directional variations characteristic at Horns Rev, Figure 2.25 on the next page discloses that winds blow predominantly from the westerly directions in the gamut from S to NW, clockwise. The 10-minute averaged wind direction frequency behavior is educed by not only meteorological measurements, but also with the

prescience that winds are less inhibited for longer sea fetches or for the longer undisturbed paths normally seen at Horns Rev in the westerly direction where the wind is blown in from the open North Sea between the United Kingdom and Norway. This pattern is also found by Neckelmann & Petersen (2000) and Hansen (2001). North is represented by 0°.

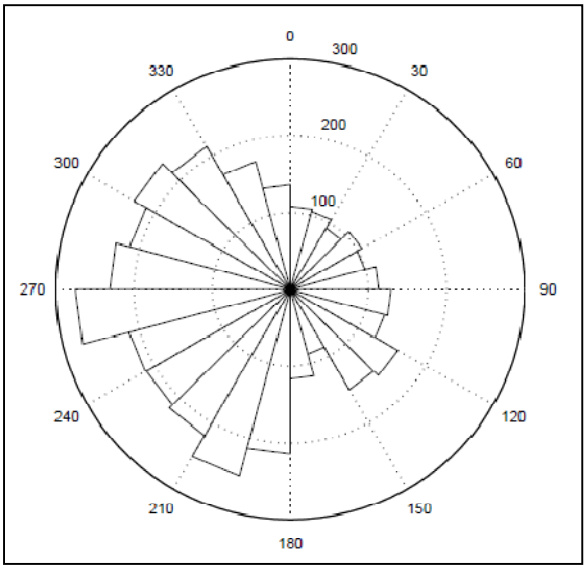

Figure 2.25: M2 wind rose at 43 m ASL.

It is commonly understood that late fall and winter seasons exhibit stronger winds at Horns Rev, whereas the wind speed for the remaining seasons is predominant generated from an ocean surface that is warmer than the ambient air, which typically produces lower wind speeds. The thermal mixing at the sea surface introduces a buoyancy effect where the air is warmed by the sea, and the heat flux is directed upward. This effect is known as unstable stratification.

Tambke *et al*. (2003) uses the gradient Richardson number to denote the atmospheric stability, which is shown on the next page. The equation used to compute the gradient Richardson number is

$$Ri_{g,Tambke} = \frac{g}{\theta}\frac{\Delta\theta}{\Delta z_\theta}/(\frac{\Delta U}{\Delta z_U})^2, \quad (2)$$

where g is the gravitational acceleration, $\theta = T(55\ m) + 0.55K$ is the potential temperature at 55 m ASL, $\Delta U = U(62\ m) - U(15\ m)$, $\Delta\theta = T(55\ m) - T(13\ m) + 0.4K$, $\Delta z_\theta = 55\ m - 13\ m$, and $\Delta z_U = 62\ m - 15\ m$. The added terms 0.55 K and 0.4 K are included to account for the conversion from absolute temperature to potential temperature, θ, or the potential temperature difference, $\Delta\theta$, respectively. The potential temperature is discussed in greater detail in the next section. One clearly deciphers that the majority of the data processed by Tambke *et al*. (2003) embodies the unstable stratification, i.e., $Ri_{g,Tambke} < 0$, viewed in Figure 2.26. It is clarified that the ordinate is the ratio of the measured wind speed at 62 m ASL to the measured wind speed at 15 m ASL.

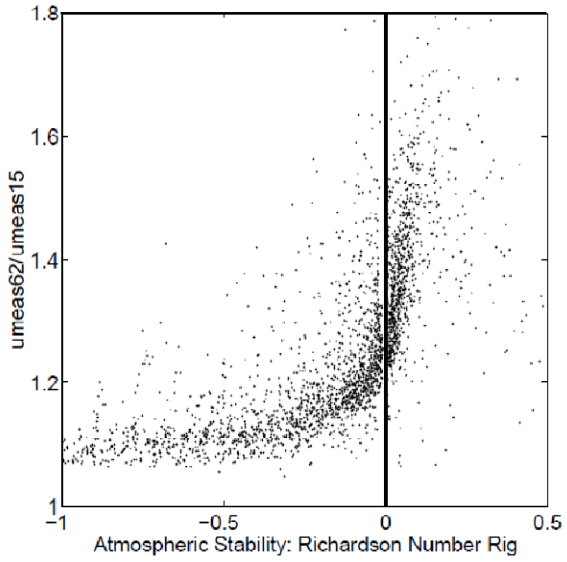

Figure 2.26: Ratio of wind speeds compared with the gradient Richardson number.

Observations of the wind profile from the open sea sector for various potential temperature differences, $\Delta\theta$, at M2 are displayed in Figure 2.27 on the following page

and expose how the logarithmic velocity profile exercises a different behavior for various stability classes. Wind profiles with larger negative potential temperature differences imitate unstable conditions and exhibit a slower-than-logarithmic wind speed as a function of height, while wind profiles with larger positive potential temperature differences represent stable settings and exude a faster-than-logarithmic wind speed as a function of height (Tambke *et al*., 2003).

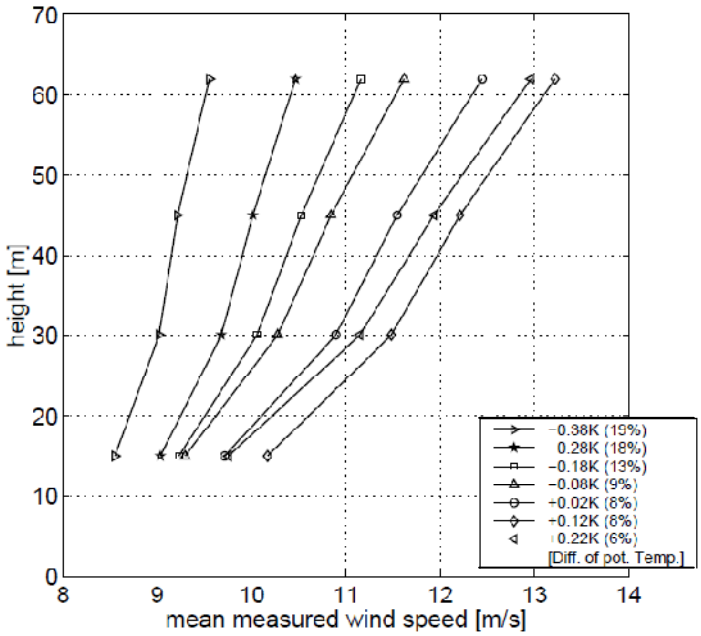

Figure 2.27: Open sea sector wind profiles outlined by potential temperature difference.

2.2.5 Peña *et al.* (2008) Observations

To extend the surface layer observations at M2 previously elaborated, an observational campaign connected to the Danish project "12 MW" was endeavored with the assistance of the owners, DONG Energy. Using field data from a mounted Doppler Laser LiDAR (Light Detection And Ranging) device located about 5.5 km due east of M2 on the Horns Rev transformer/platform, the wind profile at the reef site is portrayed up to 161 m ASL. Wind observations at the heights scanned by LiDAR devices are

characterized as highly homogeneous; it is therefore a robust practice to intercompare observations taken from M2 in the surface layer using cup and sonic anemometers with those taken on the Horns Rev platform using LiDARs. This activity extends the wind profile or fills in temporal gaps that arise during equipment failure (Hasager *et al.*, 2007).

A LiDAR is a ground-based tool that rectifies a signal gathered from reflected waves that are recorded with a focused, eye-safe laser beam along a line of sight. The LiDAR measurement geometry is detailed in the figure below. The line of sight (LOS) is measured 7.8° from the azimuth.

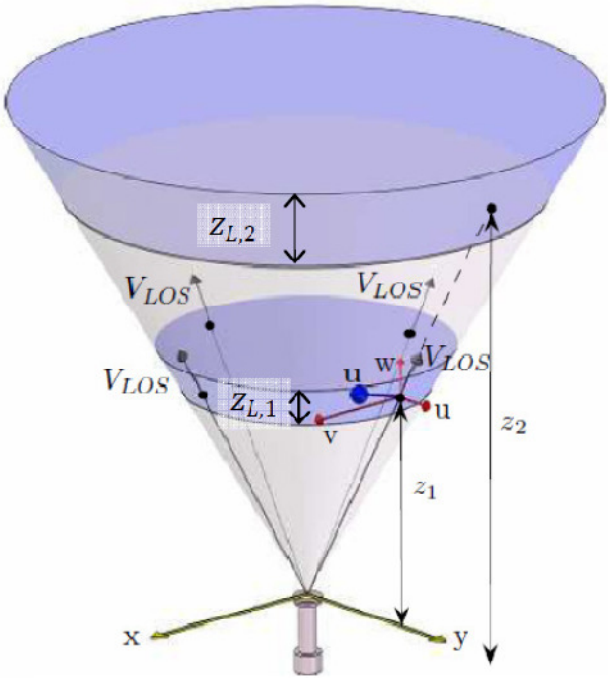

Figure 2.28: LiDAR scanning geometry (Adapted, Peña *et al.*, 2006).

Furthermore, the rectification equation supplied next finds the speed of the atmosphere at various pre-selected heights

$$V_{LOS} = |u\cos(\theta - \theta_d)\sin\phi + w\cos\phi|, \tag{3}$$

where u and w are the horizontal and vertical wind speeds, respectively, θ is the instantaneous azimuth angle, θ_d is the wind direction, and $\phi = 30.6°$ is the angle measured from the zenith.

The installation of the aforementioned LiDAR on the Horns Rev platform (see figure below) complements the "12 MW" data campaign, which lasted from May 3 to October 24, 2006. M2 data for the same period is compared with the platform observations to conclude that the data at both locations, which are 5.5 km apart, is correlated and that the admixture of data is representative of the wind profile up to 161 m ASL for the entire site. The picture on the next page exhibits the logistics of the two data gathering locations, M2 and the transformer/platform, in coincidence with the delineated wind direction sectors.

Figure 2.29: Installation of LiDAR.

LiDAR data acquisition systems are a boon to offshore wind profiling applications because the maximum usable survey height referenced is 160 m ASL on a clear day, but the LiDAR does not measure below 60 m ASL where the top cup anemometer of most met masts is located, and LiDAR observations do not suffer from speed deficit or speedup effects associated with mast-mounted cup anemometers (Hasager *et al.*, 2007).

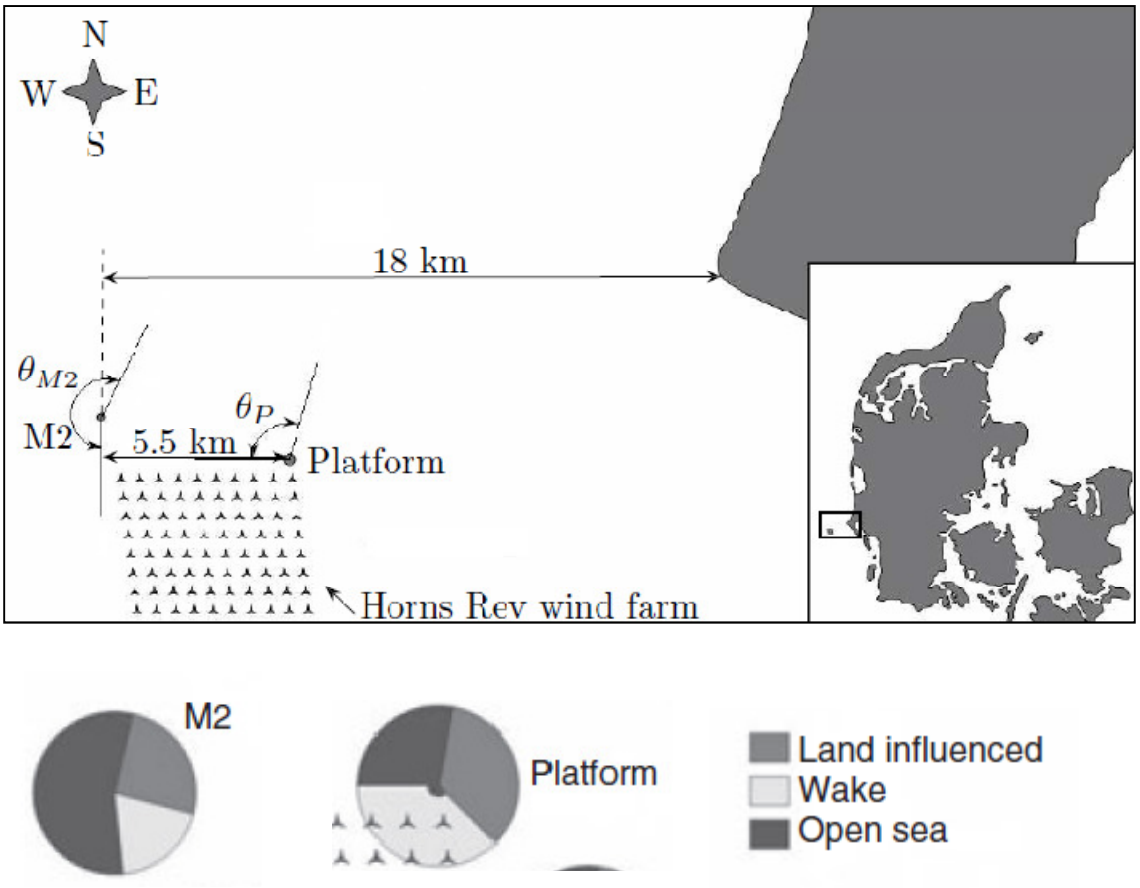

Figure 2.30: Location of M2 and the transformer/platform (Peña *et al.*, 2008). Below the logistic map, the direction sectors for the land influenced, wake, and open sea measurements are shown as pie charts. North corresponds to 0° and the positive direction is taken as clockwise. The open sea sectors associated with each location are θ_P = 270-10° and θ_{M2} = 174-13° (Peña *et al.*, 2009).

The pitfalls connected to Doppler-profiling LiDARs are noted by Hasager *et al*. (2007),

Peña *et al*. (2008), and Pederson & Wagner (2011). The drawback includes a heightened chance of spurious data reproduced with cloud-cover. LiDAR scanning geometry consists of two system parameters: the probe length, Δz_L, and the measurement height, z (see Figure 2.28 for probe length geometry). It has been determined that the probe length increases with the measurement height. Most notable, at measurement heights of 150 m ASL, the probe length is 20 m. At larger heights, the probe length becomes too great and the usable survey height typically cited for the Doppler LiDAR is 160 m ASL. A further measurement imperfection occurs when low lying clouds are present. The water droplets at the base of the cloud have greater speed than the wind at the same height; therefore, in the presence of clouds, the wind speed is overestimated and erroneous. To correct this content, the common practice implemented is to scan for the spectral backscatter at an auxiliary height significantly above the heights of the data set, i.e., 320 m ASL in this campaign. Additionally, if the backscatter coefficient at any two different heights is markedly dissimilar, then the data is excluded from the final data set (Hasager *et al.*, 2007). Peña *et al.* (2009) determined that spurious data totaled 20% of the entire collection. The data availability is shown in the table below, but is not yet filtered to exclude any specious records.

Table 2.6: Data availability for LiDAR and M2 measurements (Adapted, Peña *et al.*, 2009).

Instrument	Availability (%)
M2	99.32
LiDAR	44.85

When compared to the surface layer theoretical logarithmic profile for neutral conditions, the LiDAR systematic deviation amounts to 0.15% at 100 m ASL. Similar to

the calibration technique used to validate cup anemometer recordings, i.e., comparing opposing side-mounted anemometers readings for a near-unity correlation and linear regression trend, the LiDAR measurement at one height are examined for their correlation to cup anemometer data at the same or approximate height as shown in the Figure 2.31 below. LiDAR measurements at 63 m ASL and M2 cup anemometer data at 62 m ASL reveal a 0.97 correlation coefficient as well as a 0.96 linear regression slope and a 0.16 ms^{-1} offset.

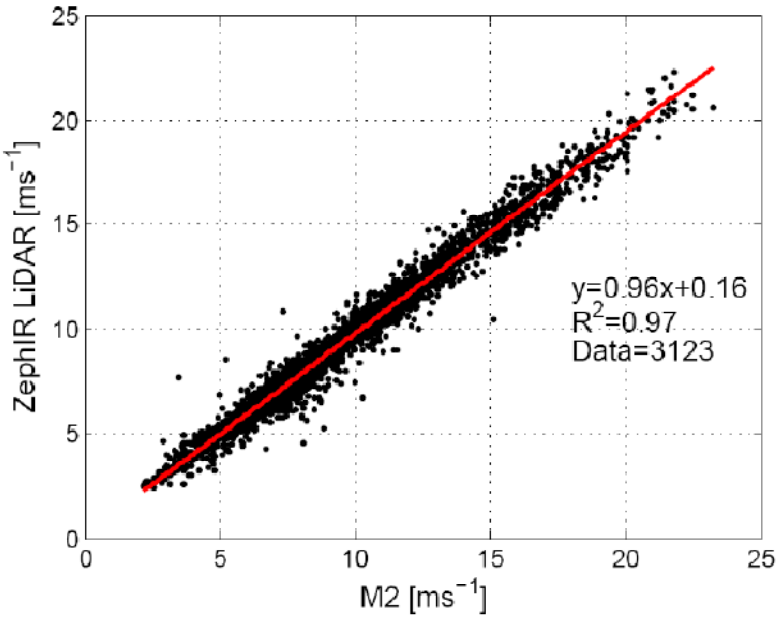

Figure 2.31: Validation of LiDAR observations at 63 m ASL (Hasager *et al.*, 2007).

There is a noted speedup effect at the top anemometer on M2 (refer to Tambke *et al.* (2003), Hasager *et al.* (2007), and Perrin *et al.* (2007)). Tambke *et al.* (2003) simply states that the speedup typically found at the top-mounted anemometer could be minimized by correcting the flow distortion at the lower cups. Likewise Hasager *et al.* (2007) also points out the speedup and similarly interject that corrections to the bottom cup recordings for a 1-2% flow distortion error would increase the wind speed at those

levels yielding a more logarithmic relationship. Perrin *et al*. (2007) focuses solely on quantifying and correcting the speedup effect at the top-mounted anemometer and goes on to say that the error amounts to 1-2%.

The collaborative effort to combine LiDAR and cup anemometer measurements is showcased in Figure 2.32 and is taken from the same data set (May-Oct 2006); however, Hasager *et al.* (2008) excludes the top anemometer readings from M2 and opts to leave a gap in the extended wind profiles.

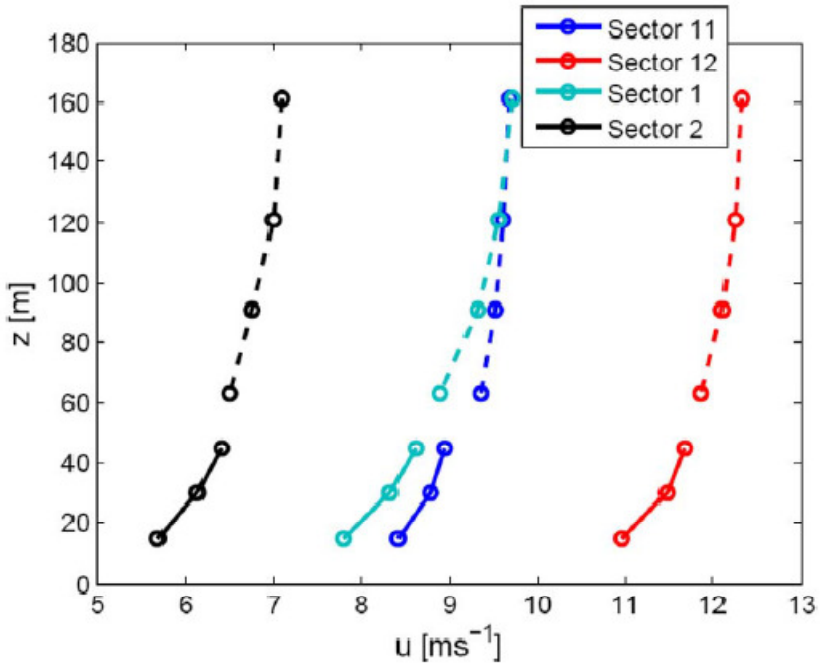

Figure 2.32: Horizontal mean wind speed profiles extended using LiDAR data.

The sectors correspond to 30° wind direction bins, i.e., 1: 0-30°, 2: 30-60°, 11: 300-330°, and 12: 330-360°. Sector 12 shows the highest conformity between LiDAR and cup readings, which signifies the wind blowing from the NW along the largest fetch distance in the North Sea. The correlation, linear regression, and offset for sector 12 are provided below from Hasager *et al.* (2008), but there is a typo for the y-axis that should contain the unit ms^{-1} not "m [sic]" (Hasager *et al.*, 2008).

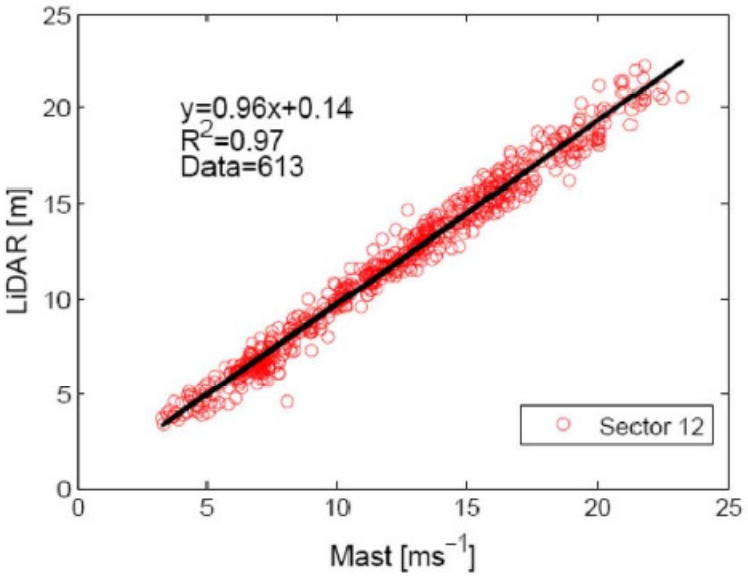

Figure 2.33: Correlation between M2 and LiDAR platform wind speeds.

Peña *et al.* (2009) includes the top anemometer observations along with error bars at all heights for the coupled LiDAR and M2 data segregated by wind sector, shown in the image below.

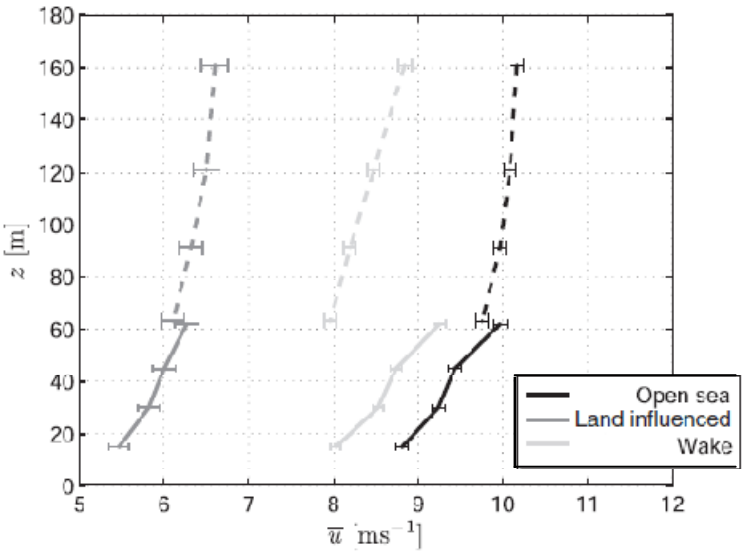

Figure 2.34: Coupled LiDAR and M2 mean wind speed observations.

Furthermore, Peña *et al.* (2008) depicts the wind profile extended to 161 m ASL at Horns Rev, which is delineated by average stability class and informs us that the referenced

corrections to MO theory accounting for atmospheric conditions and sea roughness are valid and well-suited approximations for neutral to very unstable environments. Albeit, there is work still to be done in revealing the appropriate corrections to MO theory for all stable classes. The figure below denotes these findings, where the data markers in the legend represent very stable (VS), stable (S), near stable (NS), neutral (N), near unstable (NU), unstable (U), and very unstable (VU), in that order from the top marker to the bottom marker.

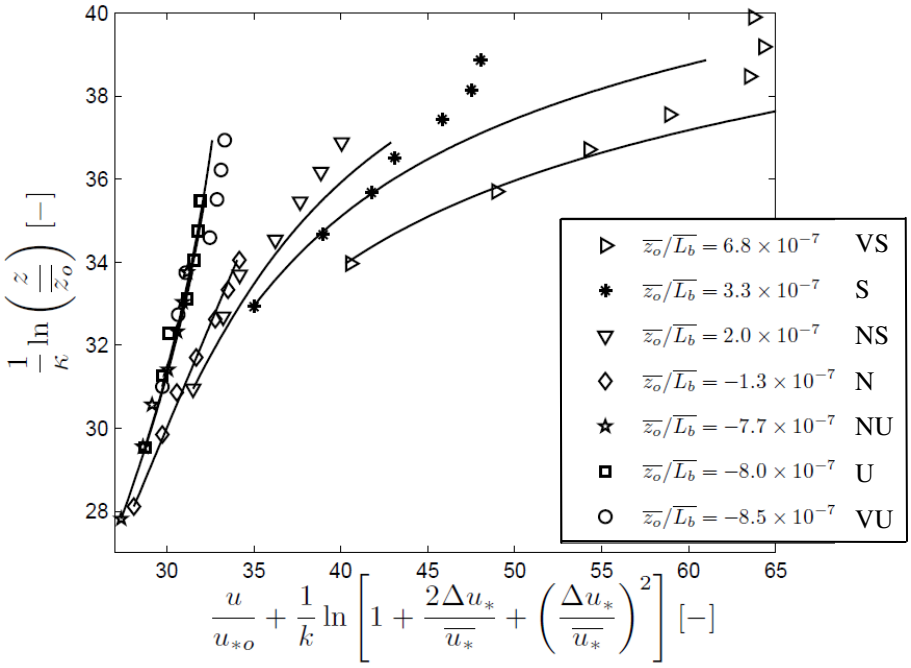

Figure 2.35: Dimensionless averaged wind profiles and stability classes (Adapted).

Peña *et al.* (2008) performs a stability analysis derived from 10-minute averaged temperature recordings at Horns Rev. Observations include the ambient and sea temperatures at three various heights, 4 m BSL and 15 and 55 m ASL from the surface. Displayed below is a newfangled temperature graphic that correlates sea surface temperature (SST) and ambient temperature observations from M2. The SST observations are from a set of satellites whose data is post-processed in a method detailed

by Høyer and She (2007). The daily time series equivalent to May-October 2006 is depicted in the figure below.

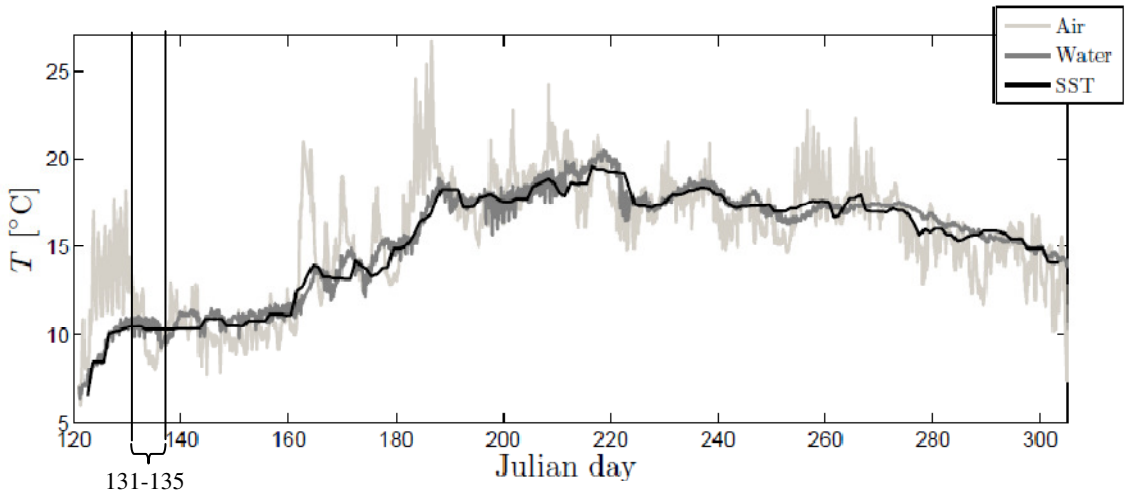

Figure 2.36: Ambient water and air temperature (Peña *et al.*, 2008).

The air temperature is reported from 55 m ASL, while the water temperature is recorded at 4 m BSL. SST is the sea surface temperature, i.e., 0 m or at the surface, which is garnered from satellites. A closeup of the daily range between 131-135 in Figure 2.37 is given next; however, the SST satellite data is not included, and the observations are instead provided for westerly, open sea winds at all thermal measuring heights on M2.

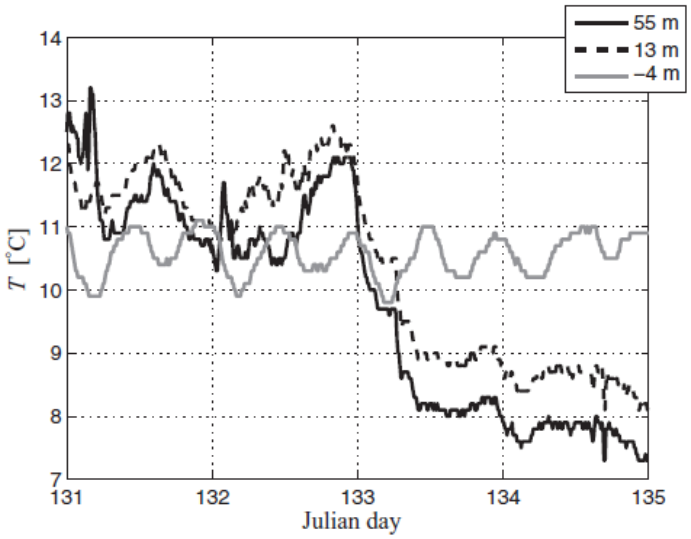

Figure 2.37: Ambient water and air temperature from days 131 to 135 (Peña *et al.*, 2008).

This particular specimen of data illustrates unstable atmospheric conditions from days 133 to 135, i.e., the water temperature at 4 m BSL is warmer than the air temperature at 13 and 55 m. Additionally, it is evident that the SST measurements from satellite shown in Figure 2.36 conform well to the temperature recordings on M2 at 4 m BSL in Figure 2.36. Peña *et al.* (2008) concludes that the M2 temperature data at 4 m BSL can be exchanged with satellite SST data if the need arises after a linear regression analysis of the two data series is generated. A 0.97 correlation coefficient along with a 0.99 linear regression slope and a -0.01 °C offset are found and shown in the figure below.

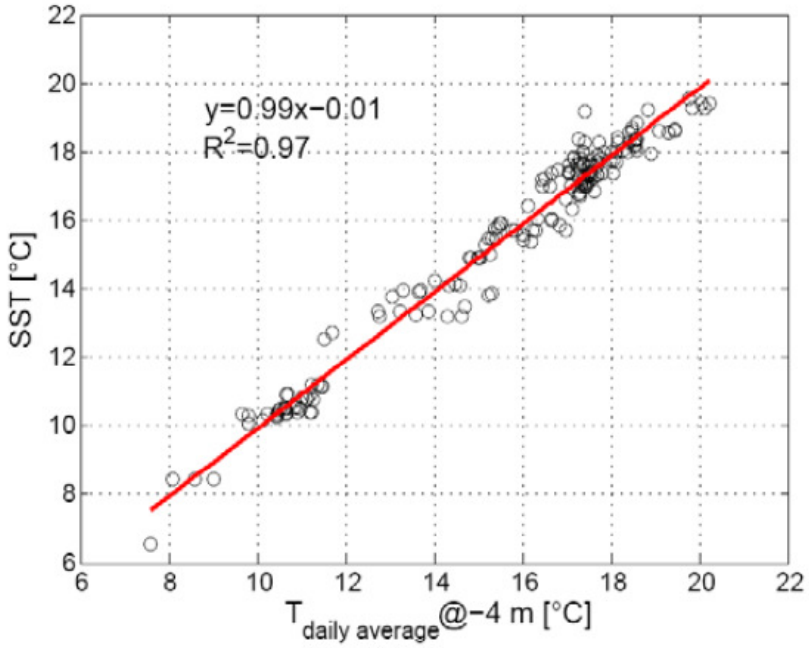

Figure 2.38: Linear regression analysis of daily average temperature (Hasager *et al.*, 2007).

After the temperature data is collected, one performs a stability analysis by choice of gradient or bulk Richardson number. Table 2.7 on the next page from Peña *et al.* (2008) illustrates a stability classification scheme based on the MO length scale, *L*, for Horns Rev. It is noted that the dominant stability class during this data collection phase comprises the neutral and all unstable classes. The usefulness of the averaged data bins

conduces to the selection of the data set from Peña *et al.* (2008) for validation of the customized k-ε code reported on in the 'Results' section. Table 2.8 next displays the averaged stability bins that accommodate Table 2.7.

Table 2.7: Stability classes according to MO length.

Obukhov length interval [m]	Atmospheric stability class
$10 \leq L \leq 50$	Very stable (vs)
$50 \leq L \leq 200$	Stable (s)
$200 \leq L \leq 500$	Near stable/neutral (ns)
$\|L\| \geq 500$	Neutral (n)
$-500 \leq L \leq -200$	Near unstable/neutral (nu)
$-200 \leq L \leq -100$	Unstable (u)
$-100 \leq L \leq -50$	Very unstable (vu)

Table 2.8: Averaged stability classes from Peña *et al.* (2008).

Stability class	$\overline{L_b}$ [m]	$\overline{u_{*o}}$ [m s^{-1}]	u_{15} [m s^{-1}]	$\overline{z_o}$ [m]	z_i [m]	No. of Profiles
vs	28	0.12	4.94	1.9×10^{-5}	122	109
s	85	0.15	5.33	2.9×10^{-5}	150	73
ns	314	0.23	7.08	6.3×10^{-5}	223	18
n	-1531	0.40	11.10	19.6×10^{-5}	393	314
nu	-288	0.42	11.54	22.0×10^{-5}	-	600
u	-139	0.30	8.60	11.1×10^{-5}	-	544
vu	-73	0.22	6.65	6.2×10^{-5}	-	358

The averaged parameters, such as the Monin-Obukhov length scale, $\bar{L}_b$, the friction velocity, $\bar{u}_{*0}$, the velocity at 15 m, u_{15}, and the roughness length, $\bar{z}_0$, are utilized to form the temperature and velocity profiles based on MO theory detailed in the next section. The average MO length scale, $\overline{L_b}$, is found by applying the bulk Richardson method, a modified form of (1), to the temperature data shown in Figure 2.36 and the following equation

$$\frac{z}{L} = C_1 \mathrm{Ri}_{\mathrm{B,Peña}} , \tag{4}$$

where $C_1 = 10$ is suggested by Grachev & Fairall (1997), z is the reference height equal

to 15 m, and $Ri_{B,Peña}$ is a modified form of the bulk Richardson number given in (1). The Peña *et al.* (2008) modified bulk Richardson number is

$$Ri_{B,Peña} = -\frac{gz\Delta\Theta_v}{T_z u_z^2}, \tag{5}$$

where z is the reference height of the recordings of the temperature and wind speed, T_z (observed in K) and u_z , respectively, and $\Delta\Theta_v$ is the mean virtual potential temperature difference between the sea surface and the reference height. It is recalled that the available data recordings highlight reference temperatures at 4 m BSL and 13 m ASL, while the reference wind speed is garnered at 15 m ASL. Finally, the reference height, z, in (5) is taken as 15 m ASL even though the temperature recordings are collected at 4 m BSL and 13 m ASL instead of 0 m and 15 m ASL. The mean virtual potential temperature difference is approximated by Peña *et al.* (2008) with the following relation

$$\Delta\Theta_v = \Delta\Theta + 0.61 T_z \Delta q, \tag{6}$$

where $\Delta\Theta$ is the mean potential temperature difference between the sea surface and reference temperature and Δq is the specific humidity difference between the sea surface and reference height. A simplification for the relative humidity is estimated as 100% at 4 m BSL and 80% at 13 m. The potential temperature is given by

$$\theta(z) = T(z)\left(\frac{P_0}{P(z)}\right)^{R/c_p}, \tag{7}$$

where T is the absolute temperature at a given height in the atmosphere, e.g., 0 m or 13 m ASL, R is the gas constant of air, c_p is the specific heat capacity of air at constant pressure, P_0 is the standard reference pressure typically 1013.25 millibars at the sea

surface or 101,325 Pa in FLUENT, and $P(z)$ is the atmospheric pressure at a given height in the atmosphere, e.g., 0 m or 13 m ASL(Cushman-Roisin, 2012). Taking the difference between the potential temperature at 13 m ASL and that computed at 0 m gives the potential temperature difference, $\Delta\Theta$ in (6). If the atmospheric pressure, $P(z)$, at a given height is not known, then a hydrostatic assumption can be made. The atmospheric pressure becomes

$$P(z) = P_0 - g\rho z, \tag{8}$$

where most of the variables have been defined previously and z is the height of the temperature recording in a neutral atmosphere (Crespo *et al.*, 1985). Vendel *et al.* (2010) demonstrates that the pressure profile is in fact a function of MO length scale for unstable and stable environments, but the integral is quite complex. Thus, potential temperature computations are forgone in this paper.

The modified bulk Richardson number employed by Peña *et al.* (2008) is not without fault. The article goes on to show that there are credible differences between its use of cup anemometer and temperature observations with (4) and (5) to determine the MO length scale and its use of sonic anemometer recordings to derive the MO length scale. The sonic anemometer derivation to compute *L* is not detailed in this paper. The deviations between the two methods are accentuated in the figure on the next page. It is interesting to note that the bulk method approximation gives a reduced number of neutral stability profiles, while gains are revealed in all unstable classes for the bulk Richardson number method. These departures are cited as having a causal relationship with the

approximation of the humidity at the sea surface and at 13 m ASL, i.e., 100% and 80%, respectively. This of course is unrealistic in actual marine atmospheres where the humidity is quite volatile.

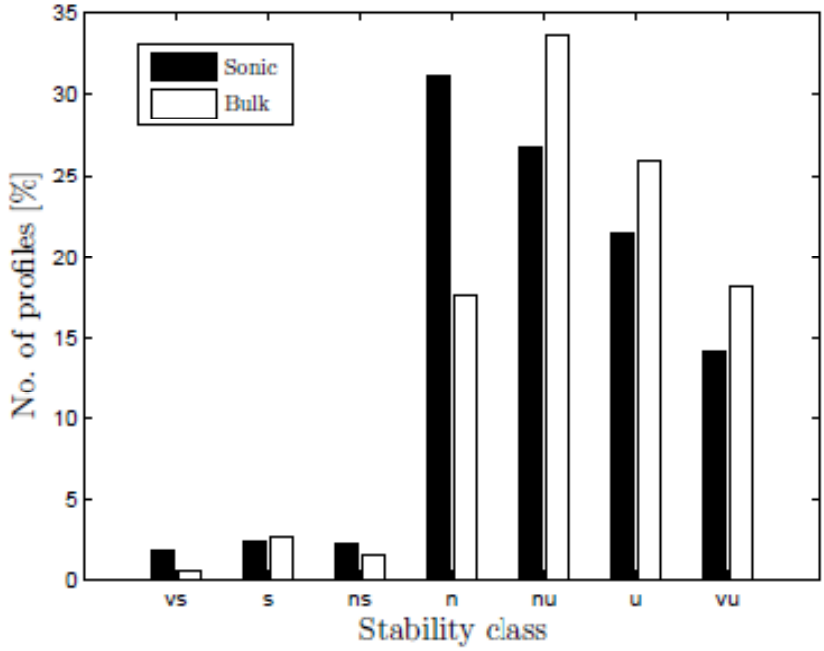

Figure 2.39: Deviation between MO length scale derived using sonic and bulk methods.

2.2.6 Larsén et al. (2011) Observations

Larsén *et al.* (2011) performs an intercomparison from observations beginning in 1999 and lasting until 2007 for all met masts at Horns Rev. These data sets have been discussed in the previous sections for M2 only from Neckelmann & Petersen (2000), Hansen (2001), Tech-Wise (2002), Tambke *et al.* (2003), and Peña *et al.* (2008). Two data sets of interest are a composition of M2 and M7 cup anemometer, sonic anemometer, wind vane, thermometer, and pressure observations. M7 is the met mast located east of M2 a few kilometers closer to Jutland. The table on the successive page from Larsén *et al.* (2011) displays the availability of the two data gathering campaigns at

Horns Rev over the years.

Table 2.9: Data availability at Horns Rev for M2 & M7 (Adapted).

Year	Horns Rev	
	M_2	M_7
1999	60%	
2000	99.975%	
2001	99.979%	
2002	99.9%	
2003	80.2%	46%
2004	99.79%	90%
2005	77%	98%
2006	86%	89%
2007	20%	73%
2008		

The bulk Richardson number is used to characterize the atmospheric seasonal stability at Horns Rev for all data campaigns at M2 from 1999-2005, and the image is rendered below.

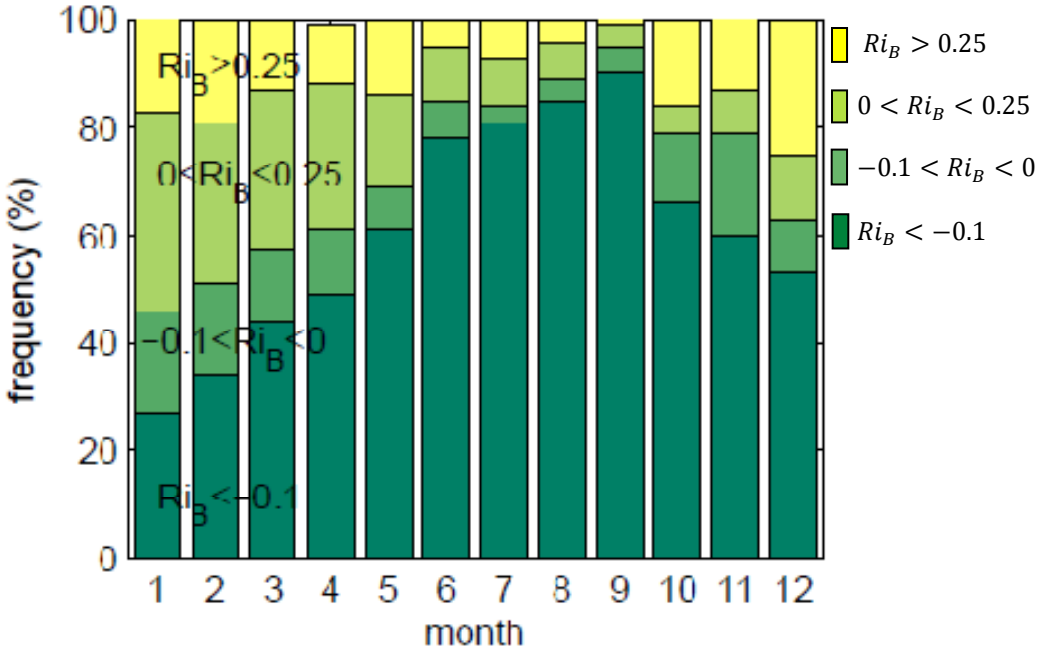

Figure 2.40: Frequency of seasonal stability classes from 1999-2005 (Adapted).

Larsén *et al*. (2011) clarifies that the ambient wind conditions at Horns Rev from the winds blowing westward are predominantly unstable in Figure 2.40, i.e., for $Ri_B < 0$, corresponding to the dark green and green colors. The peak convective months are May to October. The equation used to compute the bulk Richardson number is given by (1) above and has been modified by Larsén *et al.* (2011) to include only potential temperature effects as follows

$$Ri_{B,\text{Larsén}} = \frac{g}{\theta}\frac{\Delta\theta}{\Delta z}/(\frac{\Delta U}{\Delta z})^2, \tag{9}$$

where g is the gravitational acceleration, θ is the potential temperature at the greatest measurement height of a pair of measurements, z is the reference height, U is the mean wind speed, and Δ is the difference between the associated variable at 15 and 45 m ASL. The potential temperature was given by (7) previously. The temperature obtained at 13 and 55 m ASL is linearly interpolated, and the temperature at 15 and 45 m ASL are readily approximated with this approach. Additionally, if the pressure data is known, a linear interpolation simplification is assumed between observational heights and applied to obtain the pressure at 15 and 45 m ASL. The potential temperature computation in (9) using (7) is then found directly.

It is noted in Larsén *et al.* (2011) that the trend in the seasonal ambient wind behavior remains unchanged when parameterized by $Ri_{B,\text{Larsén}}$ between 1999-2005 at M2 and when additionally parameterized by $R_{B,\text{Larsén}}$ between 2003-2007 at M7, the met mast located east of M2 (see Figure 2.41 on next page). As a result, the overgeneralization is formed that either data set and Richardson formulation are characteristic of the ambient wind conditions at Horns Rev as a whole.

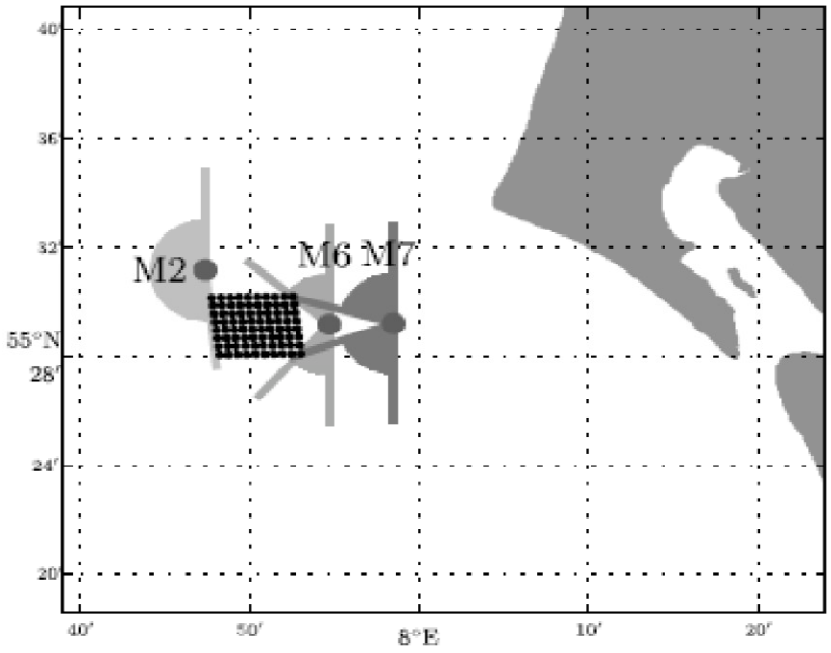

Figure 2.41: Horns Rev showing all met masts and wind farm.

The frequency of seasonal stability class at Horns Rev computed using $R_{B,\text{Larsén}}$ for the data garnered from 2003-2007 at M7 is showcased below.

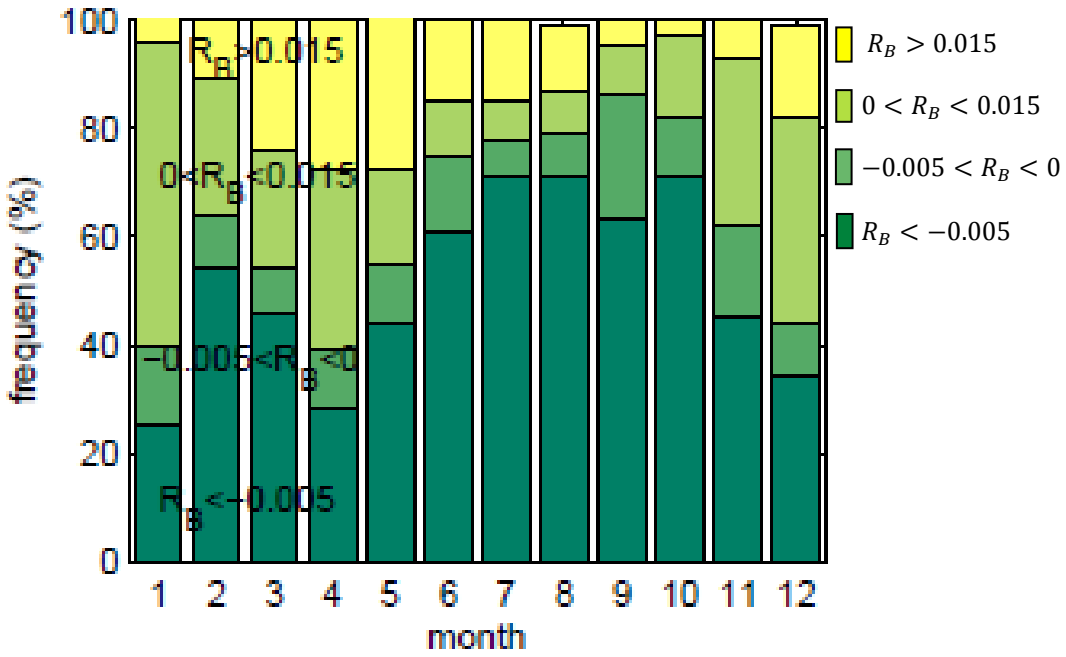

Figure 2.42: Frequency of seasonal stability classes from 2003-2007 (Adapted).

As a point of clarification, for the data processed between 2003-2007 at M7, the second formulation of the bulk Richardson number, which excludes potential temperature differences, is given by

$$R_{B,Larsén} = \frac{g}{T}\frac{(T - T_W)}{z}/(\frac{U}{z})^2, \quad (10)$$

where T is the absolute temperature at the first measuring height, T_W is the water temperature at the sea surface, U is the mean wind speed at the first measuring height, and z is the distance from the sea surface to the first measuring height at M7 (= 20 m ASL) (Larsén *et al.*, 2011). Two forms of the Richardson number are provided in the aforementioned article as a means to accommodate scenarios when data from one met mast is not available or gives specious results. To reiterate, this paper follows the supposition formed by Larsén *et al.* (2011), which states that the formulation of the Richardson number as well as the mast from which the data is post-processed are the choice of the experimenter since the stability analysis of two random samples at Horns Rev are consistent.

3 Atmospheric Boundary Layer Theory

Atmospheric boundary layer theory is detailed in the following sections and includes the theoretical mean profiles of velocity, temperature, turbulent kinetic energy, and turbulent dissipation rate derived from Monin-Obukhov (MO) similarity theory. An extension of MO theory is defined that supplants the surface roughness with the marine surface roughness. The turbulent viscosity taken from a mixing length expression is provided next followed by a brief review of the various ways to quantify the boundary layer height.

3.1 Theoretical Mean Profiles—u(z), T(z), k(z), and ε(z)

Hargreaves & Wright (2007) writes that the Richards & Hoxey (1993) log law velocity corrected for sand grain wall roughness, TDR, and TKE relations are the appropriate inlet initialization profiles for neutral atmospheric boundary layers, where the MO length scale is approximated as infinity, $L \rightarrow \infty$, and the temperature gradient is constant. These conditions are a rarity in reality, which is prone to non-constant gradients in the temperature profile in the surface layer. It should be noted that z in these equations corresponds to the y-dimension, or the height, of the simulation domains. The z-dimension in the simulation domain is the lateral direction. To maintain cohesion with other texts, the theoretical equations have not been modified to represent the simulation domains' coordinate system.

It is revealed that FLUENT, the CFD package employed in this paper to simulate the neutral and unstable ABL at Horns Rev, bases its standard wall function roughness option

from the first of three Richards & Hoxey (RH) equations given below

$$u(z) = \frac{u_*}{\kappa}\ln(\frac{z+ z_0}{z_0}), \tag{11}$$

$$k = \frac{u_*^2}{\sqrt{C_\mu}}, \text{ and} \tag{12}$$

$$\varepsilon = \frac{u_*^3}{\kappa(z+ z_0)}. \tag{13}$$

Equation (11) is the log law velocity profile including a specified wall roughness parameter, z_0, the friction velocity, u_*, the von Kármán constant, κ, and the height, z. Equation (12) is the TKE profile, where the friction velocity and turbulent viscosity constant, C_μ, are the independent variables. Equation (13) is the TDR profile including a specified wall roughness parameter, friction velocity, von Kármán constant, and height. Furthermore, the boundary layer theory relations, (11)-(13), which are noted in the Richards & Hoxey (1993) work, are adapted to include thermal stability and are derived from the Monin-Obukhov (MO) similarity theory originally authored by Monin & Obukhov (1954) and applied by Panofsky and Dutton (1984). These relations become non-linear, intricate, and sometimes lengthy and are shown below

$$u_o(z) = \begin{cases} \frac{u_*}{\kappa}\left[\ln\left(\frac{z}{z_o}\right) + \ln\left(\frac{8\phi_m^4\left(\frac{z}{L}\right)}{\left(\phi_m\left(\frac{z}{L}\right)+ 1\right)^2\left(\phi_m^2\left(\frac{z}{L}\right)+ 1\right)}\right) - \frac{\pi}{2} + 2\arctan\left(\frac{1}{\phi_m\left(\frac{z}{L}\right)}\right)\right], L < 0 \\ \frac{u_*}{\kappa}\left[\ln\left(\frac{z}{z_o}\right) + \phi_m\left(\frac{z}{L}\right) - 1\right], L > 0 \end{cases}, \tag{14}$$

where most of the constants have previously been defined, the von Kármán constant is taken as 0.42 in this simulation, $\phi_m(\frac{z}{L})$ is known as the non-dimensional wind shear, and L is the MO length, which is negative in the convective boundary layer, is a very large

negative value or taken as infinity in the neutral boundary layer, and is positive for stable conditions. The non-dimensional wind shear is given by

$$\phi_m\left(\frac{z}{L}\right) = \begin{cases} \left(1 - 16\frac{z}{L}\right)^{-0.25}, & L < 0 \\ \left(1 + 5\frac{z}{L}\right), & L > 0 \end{cases}, \tag{15}$$

where

$$L = \frac{u_*^2 T_w}{\kappa g T_*}, \tag{16}$$

and

$$T_* = -\frac{\dot{q}_w}{\rho c_p u_*}. \tag{17}$$

The remaining constants are the wall temperature, T_w, the density, ρ, the heat flux at the wall, $\dot{q}_w$, and the specific heat of air, c_p. Expression (17) is called the turbulent temperature and is connected to the temperature profile adjusted for thermal stability and given by

$$T_o(z) - T_w = \begin{cases} \frac{T_*}{\kappa}\left[\ln\left(\frac{z}{z_o}\right) - 2\ln\left(\frac{1}{2}\left(1 + \phi_m^{-2}\left(\frac{z}{L}\right)\right)\right) - \frac{g}{c_p}(z - z_o)\right], & L < 0 \\ \frac{T_*}{\kappa}\left[\ln\left(\frac{z}{z_o}\right) + \phi_m\left(\frac{z}{L}\right) - 1\right] - \frac{g}{c_p}(z - z_o), & L > 0 \end{cases}. \tag{18}$$

Another relation for the TDR is provided below

$$\varepsilon_o(z) = \frac{{u_*}^3}{\kappa z}\phi_\varepsilon\left(\frac{z}{L}\right), \tag{19}$$

where $\phi_\varepsilon\left(\frac{z}{L}\right)$ is the non-dimensional TDR expressed as

$$\phi_\varepsilon\left(\frac{z}{L}\right) = \begin{cases} 1 - \frac{z}{L} & , \; L \; < \; 0 \\ \phi_m\left(\frac{z}{L}\right) - \frac{z}{L} & , \; L \; > \; 0 \end{cases}. \tag{20}$$

The MO TKE is related to the turbulent eddy viscosity (see the left side of the first arrow in (21)), but updated now includes stability effects as follows

$$\mu_t = \rho C_\mu \frac{k^2}{\varepsilon} \rightarrow k = \sqrt{\frac{\mu_t \varepsilon}{\rho C_\mu}} \rightarrow k_o(z) = \sqrt{\frac{\mu_{to}(z)\varepsilon_o(z)}{\rho C_\mu}} = 5.48 u_*^2 \left(\frac{\phi_\varepsilon\left(\frac{z}{L}\right)}{\phi_m\left(\frac{z}{L}\right)}\right)^{0.5}, \tag{21}$$

where Alinot & Masson (2005) have cited the use of $\frac{1}{\sqrt{C_\mu}} = 5.48$, or

$$C_\mu = 5.48^{-2} = 0.0333, \tag{22}$$

and $\mu_{to}(z)$ is given by the expression in (25) discussed in a forthcoming section.

The friction velocity, u_*, is computed from a set of reference flow parameters that are presented in Alinot & Masson (2005). The reference neutral and unstable flow values are the following: $u_{ref} = 10\ m/s$; $z_{ref} = 35\ m$; z_o, which varies for the neutral case and for the unstable case is 0.00188 m and 0.0004 m, respectively; the MO length of infinity for the neutral case and -231 m for the unstable case; and the von Kármán constant, $\kappa = 0.42$. Solving equations (14)-(22) with the reference flow values yields a friction velocity $u_* = 0.427\ m/s$ for the neutral case and $u_* = 0.382\ m/s$ for the unstable case. These values are used in the verification procedure to test if this paper's customized k-ε neutral and unstable codes are performing similarly to Alinot & Masson (2005). This topic is explored later in the 'Results' section and 'Neutral and Unstable Verification Studies' subsection where tables with the reference flow parameters are provided for the

reader to examine.

3.2 Roughness Length—z_0

Hargreaves & Wright (2007), Blocken *et al.* (2007), and O'Sullivan *et al.* (2011) consent that it is easier to modify the sand grain roughness height, ε_R, while maintaining FLUENT's default value for the roughness constant, $C_S = 0.5$. Additionally, when given the reference surface roughness length, e.g., $z_0 = 0.00188\ m$, the sand grain roughness height, ε_R, is found as follows

$$\varepsilon_R = \left(\frac{E}{C_S}\right) z_0 \approx 20 z_0, \tag{23}$$

where E is an empirical constant with the default value of 9.793 in FLUENT (Hargreaves & Wright, 2007).

Although sand grains seem to be a couple of orders of magnitude smaller than most surface roughness lengths associated with ABLs, current theory and experimental results continue to uphold the standard log law of the wall for fully rough surfaces having surface roughness length scales in the complete spectrum of micrometers to meters. Surface roughness lengths manifest themselves as waves in marine environments and terrain changes, rocky surfaces, various soil types, leaf-covered ground, forested canopies, and city buildings in land environments. Attempts have been made by the European Wind Atlas to quantify and categorize these various surface roughness length scales in order to apply a standard surface roughness parameterization to ABL simulations (Troen & Petersen, 1989). Furthermore, Blocken *et al.* (2007) reiterates that for accurate simulation of rough turbulent ABL flows, the length to the center of the first

cell, y_P, along the vertical edge of the domain must be designed greater than the sand grain roughness height, ε_R, i.e., $y_P > \varepsilon_R$, or else specious results are obtained because an internal boundary layer (IBL) is generated that yields an acceleration of the flow near the surface. An IBL is secondly formed if relation (23) is not followed, i.e., if $\varepsilon_R < 20z_0$; a speedup in the near wall region is introduced. Thus, for this paper's purpose and to avoid generating unintended, increasing velocity gradients near the surface, this prescription is as follows: $0.5\Delta y = y_P > \varepsilon_R = 20z_0$, where Δy is the height of the first cell in the discretized domain. The design of the domain and discretization elected for the 2D and 3D meshes are discussed following this section.

3.2.1 The Charnock Parameter—α_c

The surface roughness, z_0, is defined as that common in marine applications, $z_0 \approx 0.1 - 0.15\, mm$, or one chooses to relate the sea surface roughness to the surface wind stress and a constant named after the relation's developer, Charnock (1955). Charnock's relation is

$$z_0 = \alpha_C \frac{u_*^2}{g}, \tag{24}$$

where α_C is the Charnock parameter, g is the gravitational acceleration, and u_* is the friction velocity. In Peña *et al.* (2008), the Charnock parameter is taken as 0.012. Placing (24) into (11), (13), (14), (18), and (23) yields values dependent on the sea roughness length. Hasager *et al.* (2007) declares that by utilization of Charnock's relation to find the sea roughness length, the logarithmic profile is "always good for the cup measurements which are in the surface layer." Additionally and concurrently, the

logarithmic wind profile corrected with Charnock's relation for surface roughness displays a slight deviation compared to LiDAR measurements which are taken in the outer layer indicating that the LiDAR data may be better defined with another roughness length scale.

3.3 Theoretical Turbulent Viscosity—μ_t

The turbulent viscosity is found using a mixing length expression as follows

$$\mu_t(z) = \frac{\rho \kappa u_* z}{\phi_m\left(\frac{z}{L}\right)}, \tag{25}$$

where the density, von Kármán constant, friction velocity, vertical height, MO length scale, and non-dimensional wind shear relation should be familiar to the reader (Alinot & Masson, 2005). It is interesting that when performing simulations of ABLs, Crasto (2007) suggests increasing the value of the turbulent viscosity ratio in the 'Limits' pane and moreover implies that this value is set to the maximum available in FLUENT for ABL flows, i.e., 1e20.

Lastly, on this topic, FLUENT solves directly the turbulent viscosity by employing the following relationship

$$\mu_t = \rho C_\mu \frac{k^2}{\varepsilon}, \tag{26}$$

which was mentioned before in (21) (Fluent Inc., 2006b). The expression involves the density, a flow modeling constant, C_μ, the TDR, and the TKE. This equation is an important link between the TDR, TKE, and the k-ε model constant, C_μ. One explores the

freedom in attempting to correct and perfect ABL simulations by specifying user defined functions (UDFs) that control the simulation values of the turbulent viscosity, TDR, and TKE. Also, a UDF can be devised that allows C_μ to follow a non-constant profile. UDFs are an advanced subject, and the author of this paper has not included any for reference (Fluent Inc., 2006a). However, an attempt to correct the turbulent viscosity, C_μ, TDR, and TKE profiles in the 'Results' section using custom field functions (CFFs) is specified. These CFFs could be implemented in future simulations as UDFs.

3.4 A Caveat on the Theoretical Convective Boundary Layer Height, z_i

The earliest relation of the ABL height is given below, which states that the boundary layer height is proportional to the ratio of the friction velocity to the Coriolis parameter as

$$z_i = C \frac{\overline{u_*}}{|f_c|}, \tag{27}$$

where $C = 0.12$ and f_c is the Coriolis force (Rossby and Montgomery, 1935). The use of the boundary layer height, z_i, as a scaling parameter allows for ABL similarity theory to be generalized by stability class. However, consistent parameterization of the convective boundary layer (CBL) has evaded historic and current research efforts, such as Rossby & Montgomery (1935), Deardorff (1972), Stull (1988), Garratt (1992), Seibert *et al*. (2000), and Peña *et al*. (2008). Seibert *et al.* (2000) expresses this mystifying quantity as "often a rather unspecified parameter whose definition and estimation is not straightforward." Further, Seibert *et al.* (2000) provides a general definition for the boundary layer height, calling it the mixing height, as follows:

> The mixing height is the height of the layer adjacent to the ground over which pollutants or any constituents emitted within this layer or entrained into it become vertically dispersed by convection or mechanical turbulence within a time scale of about an hour.

The aforementioned explanation of the boundary layer height is moreover separated into two classes: 1-the height of the stable boundary layer (SBL) and 2-the height of the CBL. An example found in Moeng & Sullivan (1994) clearly illustrates the demarcation of the BL height, which is positioned where the total heat flux gradient reverses its sign displayed in Figure 3.1 below. The height for the SB1 simulation is $z_i = 498\ m$, and the height for the SB2 simulation is $z_i = 493\ m$.

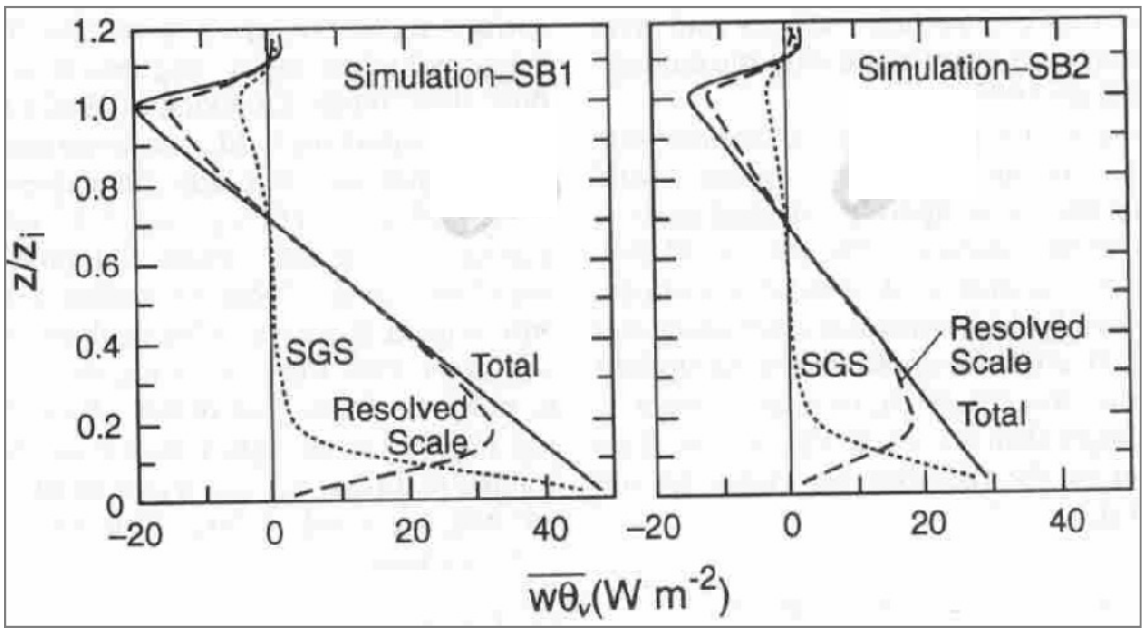

Figure 3.1: Virtual potential temperature fluxes of two moderately buoyant LES simulations.

Others in the ABL research community model the height of the boundary layer by specifying component velocity and temperature profiles taken from observational data and experience, such as Nieuwstadt *et al*. (1992), Moeng & Sullivan (1994), and

Churchfield *et al*. (2010). One example of this approach is found in Deardorff (1972) where the boundary layer height is explicitly modeled as the height of the computational domain with a capping inversion layer—a development based from the author's experience with ABL observations. More recently, Vincent *et al.* (2011) examines how the boundary layer height changes by varying the profiles of potential temperature and water vapor mixing ratio in a simplified mesoscale Weather Research & Forecasting (WRF) model of open cellular convection (OCC).

In spite of the variety of ways to determine the ABL height, this paper assumes that the BL height is identical to the height of each simulation domain. It is also noted that the common non-dimensional parameterization z/z_i is substituted by y/H, where H is the reference height, to avoid confusion.

4 FLUENT 6.3 Governing Equations

The details of the governing equations solved by FLUENT 6.3 using the finite volume method for the RANS equations of mass, momentum, and energy applied in conjunction with the steady k-ε method are provided in the subsections of this chapter.

4.1 Reynolds Time-Averaged Navier-Stokes (RANS) Equations

The instantaneous Navier-Stokes equations for continuity and momentum of an incompressible fluid for both neutral and unstable flows are formed below

$$\frac{\partial \tilde{u}_i}{\partial x_i} = 0 \text{ and} \tag{28}$$

$$\frac{\partial \tilde{u}_i}{\partial t} + \tilde{u}_j \frac{\partial \tilde{u}_i}{\partial x_j} = -\frac{1}{\rho}\left(\frac{\partial \tilde{p}}{\partial x_i} - \frac{\partial \tau_{ij}}{\partial x_j}\right). \tag{29}$$

The tilde represents the instantaneous quantities. The first equation is the continuity equation. The second equation is the momentum equation. The left hand side of the second equation is the substantial derivative. The first term on the right hand side is the pressure gradient, and the second term is the partial derivative of the stress tensor (Tennekes & Lumley, 1972 & Fluent Inc., 2006b).

Turbulence is considered in the governing equations by decomposing any instantaneous solution flow variable into a mean flow variable and a turbulent fluctuating component as follows

$$\tilde{u}_i = U_i + u_i' , \tag{30}$$

where $i = 1, 2, 3$ is equivalent to the axes x, y, and z, respectively, and where the index $i = 2$ is the vertical direction denoted y for this simulation of a three-dimensional flow. The decomposition of instantaneous scalars, such as pressure, are observed as

$$\tilde{\phi} \;\; = \Phi \;\; + \phi' \, . \tag{31}$$

After replacing each instantaneous quantity in (28) and (29) with the appropriate turbulent decomposition noted in (30) and (31), (28) and (29) become

$$\frac{\partial U_i}{\partial x_i} + \frac{\partial u_i'}{\partial x_i} = 0, \text{ and} \tag{32}$$

$$\frac{\partial U_i}{\partial t} + \frac{\partial u_i'}{\partial t} + \; U_j \; \frac{\partial U_i}{\partial x_j} + U_j \; \frac{\partial u_i'}{\partial x_j} + u_j' \; \frac{\partial U_i}{\partial x_j} + u_j' \; \frac{\partial u_i'}{\partial x_j} = -\frac{1}{\rho}\left(\frac{\partial P}{\partial x_i} + \frac{\partial p'}{\partial x_i} - \frac{\partial \tau_{ij}}{\partial x_j}\right). \tag{33}$$

The stress tensor is left unaltered for simplicity of the derivation in (33). Further reductions are considered by taking the time average of each term to produce the final ensemble RANS equations (Fluent Inc., 2006b & Crasto, 2007)

$$\nabla \cdot U_i = 0 \text{ , and} \tag{34}$$

$$\frac{\partial U_i}{\partial t} + \frac{\partial (U_i U_j)}{\partial x_j} + \frac{\partial (\overline{u_i' u_j'})}{\partial x_j} = -\frac{1}{\rho}\frac{\partial P}{\partial x_i} + \frac{\partial}{\partial x_j}\left[\nu\left(\frac{\partial U_i}{\partial x_j} + \frac{\partial U_j}{\partial x_i} - \frac{2}{3}\delta_{ij}\frac{\partial U_k}{\partial x_k}\right)\right]. \tag{35}$$

The kinematic viscosity is ν in (35) and the operator δ_{ij} is the Kronecker delta. The ∇ in (34) is the gradient operator. The last term in (35) is another form of the partial derivative of the stress tensor and is also known as the partial derivative of the stress due to the kinematic viscosity. Looking at (35), it is noted that there are too many unknowns to solve the time-averaged RANS equations, i.e., the fluctuations in the third term on the

left are unknown. These additional quantities are the turbulence contributions to the flow and are either modeled using subgrid scale (SGS) approximations, which are common when employing unsteady solvers in FLUENT, or are modeled directly in FLUENT, e.g., the k-ε steady solver allows the user to input the TDR and TKE turbulence quantities directly into the simulation. Additionally, the turbulent kinetic energy, k, and turbulent dissipation rate, ε, are related to the turbulent viscosity. Thus, the k-ε steady solver is employed to "close" the RANS equations when the turbulent fluctuations noted in (35) are not known (Ferziger & Perić, 2002). This method is used to reach a steady-state solution of the flow. Furthermore, the term containing the fluctuations on the left hand side of (35) is related to the generation of TKE, G_k, via the relation

$$G_k = -\rho\overline{u_i' u_j'}\frac{\partial U_i}{\partial x_j} \text{ (Fluent Inc., 2006b).} \tag{36}$$

Lastly, it is recalled that when employing the steady k-ε method, terms containing time in (35) are neglected.

4.2 The Governing Energy Equation

The energy equation is activated for both neutral and unstable ABL simulations, and new terms exist to model buoyancy in the momentum equation compared to the general RANS equation expressed in the previous section for momentum. The inclusion of buoyancy arises when the density is changed from constant to Boussinesq in the 'Materials' panel, when the 'Energy Equation' is activated in the 'Models' panel, and with the selection of the gravity option in the 'Operating Conditions' panel. The energy equation is as follows

$$\frac{\partial}{\partial t}(\rho E) + \frac{\partial}{\partial x_i}[u_i(\rho E + p)] = \frac{\partial}{\partial x_j}\left[\left(k + \frac{c_p \mu_t}{Pr_t}\right)\frac{\partial T}{\partial x_j} + u_i(\tau_{ij})_{eff}\right] + S_h, \quad (37)$$

where $(\tau_{ij})_{eff}$ is the deviatoric stress tensor defined by

$$(\tau_{ij})_{eff} = \mu_{eff}\left(\frac{\partial u_j}{\partial x_i} + \frac{\partial u_i}{\partial x_j}\right) - \frac{2}{3}\mu_{eff}\frac{\partial u_k}{\partial x_k}\delta_{ij}. \quad (38)$$

In these equations, k is the thermal conductivity, E is the energy per mass, t is the time scale and is neglected in steady simulations, T is the absolute temperature, μ_t is the turbulent dynamic viscosity, Pr_t is the turbulent energy Prandtl number, μ_{eff} is the dynamic viscosity given in the deviatoric stress tensor relation (38), and the other constants and variables have been detailed previously (Fluent Inc., 2006b).

The momentum equation (29) is adapted to contain buoyancy and is displayed below

$$\frac{\partial \tilde{u}_i}{\partial t} + \tilde{u}_j \frac{\partial \tilde{u}_i}{\partial x_j} = -\frac{1}{\rho}\left(\frac{\partial \tilde{p}}{\partial x_i} - \frac{\partial \tau_{ij}}{\partial x_j}\right) - \delta_{i2} g \frac{\tilde{\vartheta}}{\theta}. \quad (39)$$

The tilde represents the instantaneous quantities, which have not been decomposed. The left hand side of the equation is the substantial derivative; however, the term containing time is neglected. The first term on the right hand side is the pressure gradient. The second term is the mechanical deformation gradient, and the third term is the buoyancy effect where $\tilde{\vartheta}$ is the difference between the actual temperature and the adiabatic temperature, or θ, and θ is the adiabatic temperature. The adiabatic temperature is also nominated the potential temperature (Tennekes & Lumley, 1972).

4.3 The Standard k-ε Method

The k-ε method is the typical CFD flow solver implemented for ABL simulations. This method is normally applied in research and industry since it is readily available in many CFD software packages, yields accurate solutions that have been verified and validated in numerous publications, and reduces the use of computer resources compared to other turbulent flow solvers such as DNS, LES, and DES (Hargreaves & Wright, 2007). The k-ε method is additionally well-suited to compute the RANS average variables of ABL flows in the surface layer, i.e., the lower 10% of the domain of an ABL, and adapts to various surface roughness heights. In particular, the surface layer is important since this is near the hub height of wind turbines and where met mast flow data collection equipment is located. Obtaining correct and robust solutions of the ABL at these heights, between 15 and 200 m, is attractive for many applications such as wind farm planning that seeks to quantify a site's available wind power (Moskalenko *et al*., 2010) and the expected turbulence intensity exerted on the wind turbines at various heights.

The standard k-ε model is employed to find a steady and consistent solution from the specified boundary and initial conditions of a neutral and unstable ABL flow using the RANS equations with a two-equation turbulence closure approximation. The closure approximations are two separate transport equations that independently determine the turbulent velocity and length scales. The model is semi-empirical and framed on the transport equations for turbulent kinetic energy, k, and turbulent kinetic energy dissipation rate, ε. Turbulent kinetic energy (TKE) and turbulent dissipation rate (TDR) are given by theoretical relations (12), (13), (19) and (21) discussed previously; however,

the transport equation for the TKE solved in FLUENT has a different look and is provided next

$$\frac{\partial}{\partial t}(\rho k) + \frac{\partial}{\partial x_i}(\rho k u_i) = \frac{\partial}{\partial x_j}\left[(\mu + \frac{\mu_t}{\sigma_k})\frac{\partial k}{\partial x_j}\right] + G_k + G_b - \rho\varepsilon - Y_M + S_k, \quad (40)$$

where k is the TKE, ρ is the density, u is the velocity component, μ is the dynamic viscosity, μ_t is the turbulent dynamic viscosity, t is the time scale, x is the dimension scale, σ_k is the turbulent Prandtl number associated with the turbulent kinetic energy equation, G_k is the generation of turbulent kinetic energy mentioned in (36) and evolved from the mean velocity gradients, G_b is the generation of turbulent kinetic energy evolved from buoyancy, ε is the TDR, Y_M is the effect of compressible turbulence found between the fluctuating dilatation and the total dissipation rate, and S_k represents other contributing kinetic energy source terms. The term containing time is neglected. Furthermore, the transport equation for the TDR solved in FLUENT is

$$\frac{\partial}{\partial t}(\rho\varepsilon) + \frac{\partial}{\partial x_i}(\rho\varepsilon u_i) = \frac{\partial}{\partial x_j}\left[(\mu + \frac{\mu_t}{\sigma_\varepsilon})\frac{\partial \varepsilon}{\partial x_j}\right] + C_{1\varepsilon}\frac{\varepsilon}{k}(G_k + C_{3\varepsilon}G_b) - C_{2\varepsilon}\rho\frac{\varepsilon^2}{k} + S_\varepsilon, \quad (41)$$

where $C_{1\varepsilon}$, $C_{2\varepsilon}$, $C_{3\varepsilon}$, and σ_ε, or the turbulent Prandtl number associated with the dissipation rate equation, are model constants, whose values are listed in the next subsection. The term containing the time is neglected in steady simulations. Other sources that contribute to the dissipation rate equation are contained in the S_ε term. The ancillary terms are the same as those detailed in (40). The generation of turbulent kinetic energy evolved from buoyancy, G_b, is highlighted in the upcoming subsection 'Choice of Turbulent Energy Prandtl Number, Pr_t.'

The turbulent, or eddy, viscosity is calculated by combining (40) and (41) and solving for μ_t, which yields the following relationship previously mentioned in (26). The constant, C_μ, is a model constant quantified in the next subsection. FLUENT provides default values for C_μ, $C_{1\varepsilon}$, $C_{2\varepsilon}$, σ_k, and σ_ε, which are derived experimentally from results of a variety of laboratory shear flows with air and water. These values are altered to fit the user's purpose and to include other flows such as free shear and wall-bounded flows (Fluent Inc., 2006b).

4.3.1 Choice of k-ε Method Model Constants

A review since 1972 of elected k-ε method model constants is provided in Table 4.1 on the next page. Illustrated is the change in the TDR Prandtl number model constant, σ_ε, after general usage of the following equation

$$C_{1\varepsilon} = C_{2\varepsilon} - \frac{\kappa^2}{\sqrt{C_\mu}\sigma_\varepsilon}, \tag{42}$$

where κ is the von Kármán constant and the other constants are related to the k-ε model constants. From the table, it is more common to fix C_μ, $C_{1\varepsilon}$, and $C_{2\varepsilon}$, and then solve (42) to find the value for σ_ε. The TDR Prandtl number in Martin's k-ε codes differs from that proposed by Duynkerke (1988) by choice of the von Kármán constant, $\kappa = 0.42$, in the Martin code and the use of three significant digits for the value of C_μ. Whereas, Duynkerke (1988) utilizes $\kappa = 0.4$ in coincident with one less significant digit for his value of C_μ. It is noticed that Crespo *et al.* (1985) and Alinot & Masson (2005) alter the value of $C_{3\varepsilon}$ to generate greater compatibility in their working codes for neutral and unstable ABLs. In FLUENT, this constant is only redefined through the implementation

of a UDF, which is an advanced topic and proves too difficult for some users. The default constant in FLUENT is 1.0 and remains unchanged in the Martin code.

Table 4.1: Review of k-ε Method Constants since 1972.

Author	Stability Class	Study	C_μ	$C_{1\varepsilon}$	$C_{2\varepsilon}$	$C_{3\varepsilon}$	σ_ε	σ_k	Pr_t	$Pr_{t,wall}$
Jones & Launder(1972)	Neutral	-	0.09	1.44	1.92	1.0	1.3	1.0		
Crespo et al.(1985)	Neutral	-	0.0333	1.21	1.92	0.8				
Duynkerke(1988)	Neutral/Unstable	-	0.033	1.46	1.83	1.0	2.38	1.0		
Alinot & Masson(2005)	Neutral	-	0.0333	1.176	1.92	1.0	1.3	1.0	1.0	
Alinot & Masson(2005)	Unstable	-	0.0333	1.176	1.92	-4.4	1.3	1.0	1.0	
Hargreaves & Wright(2007)	Neutral	-	0.09	1.44	1.92	1.0	1.11	1.0		
Martin 2D Domain	Neutral/Unstable	Verification	0.0333	1.176	1.92	1.0	1.3	1.0	1e20	1
Martin 3D Domain	Neutral/Unstable	Verification	0.0333	1.176	1.92	1.0	1.1	1.0	1e20	1

Lastly, when a value of $C_\mu = 0.09$ is chosen for both neutral and unstable simulations in connection with the energy equation, Boussinesq approximation, and gravity option activated, an incompatibility arises yielding heightened inaccuracies. However, if a purely adiabatic neutral ABL without thermal mixing is the desired simulated outcome, Hargreaves & Wright (2007) successfully runs this type of neutral ABL using $C_\mu = 0.09$ in combination with the energy equation deactivated in FLUENT. Reproduction of a diabatic neutral or unstable ABL seems to only be amenable with prescription of $C_\mu = 0.0333$ and is the opted type of flow modeled in this manuscript.

4.3.2 Choice of Turbulent Energy Prandtl Number, Pr_t

Two references assign a turbulent energy Prandtl number, Pr_t, between 0.85 (Fluent Inc., 2006b) to 1 (Alinot & Masson, 2005). Others have not mentioned this value (Crespo *et al.*, 1985; Hargreaves & Wright, 2007; Blocken *et al.*, 2007; O'Sullivan *et al.*, 2011; Vendel *et al.*, 2010). The turbulent energy Prandtl number is found using the expression below

$$Pr_t = \frac{c_p \mu_t}{k_t}, \tag{43}$$

where c_p is the specific heat of air, μ_t is the turbulent viscosity given by relation (25) or (26), and k_t is the turbulent thermal diffusivity of air. It was noted previously that Crasto (2007) recommends electing a turbulent viscosity ratio limit of 1e20 since the turbulent viscosity is "naturally very high" for ABL flows. One recalls that the turbulent viscosity ratio is the ratio of the turbulent viscosity to the laminar viscosity. Then it directly follows that the turbulent energy Prandtl number should be set to the maximum allowed in FLUENT, 1e20, in response to the expected large value of the turbulent viscosity, which is in the numerator in (43). Moreover, the TDR equation (41) contains a term known as the generation of turbulence due to buoyancy, G_b, which is given by the following relation

$$G_b = \beta g_i \frac{\mu_t}{Pr_t} \frac{\partial T}{\partial x_i}, \tag{44}$$

where β is the thermal expansion coefficient, g_i is the gravity vector in the i-th direction, $\frac{\partial T}{\partial x_i}$ is the partial temperature differential in the i-th direction, μ_t is the turbulent viscosity given by relation (25) or (26), and Pr_t is the turbulent energy Prandtl number given by (43). It is now clear that the turbulent energy Prandtl number is housed inside the turbulence generation due to buoyancy term, G_b, which is also connected to one of the k-ε model constants, $C_{3\varepsilon}$, in the TDR equation (41). The constant, $C_{3\varepsilon}$, is the "degree" that the TDR equation (41) is affected by buoyancy (Fluent Inc., 2006b). Efforts by Alinot & Masson (2005) and Crespo *et al.* (1985) to adjust their ABL simulations proceeded with alteration of the $C_{3\varepsilon}$ value, i.e., -4.4 and 0.8, respectively, for unstable boundary layers

(see Table 4.1 above). On the other hand, the FLUENT 6.3 User's Guide sets the default $C_{3\varepsilon}$ value as 1 and informs users of the ability to employ UDFs if they wish to change the default settings.

Following the useful research exposed by Alinot & Masson (2005) that improves the accuracy of unstable ABL simulations by altering $C_{3\varepsilon}$, one can claim that leaving the default value of $C_{3\varepsilon}$ unchanged and instead modifying the G_b term by varying the turbulent energy Prandtl number would similarly fix any erroneous behavior found in thermally stratified ABL simulations. As well, the FLUENT 6.3 User's Guide indicates that "customizing the turbulent Prandtl numbers" by utilizing a UDF is an option for perfecting a user's flow simulations (Fluent Inc., 2006a). With that said, this paper's mechanism for improving the accuracy of thermally stratified neutral and unstable ABL simulations is to set the turbulent energy Prandtl number to the maximum allowed in FLUENT, i.e., 1e20. Since this type of solution is a tuning device similar to curve fitting, sensitivity testing will ensue for a variety of turbulent energy Prandtl numbers and illustrate the effect on the average flow variables such as the velocity, temperature, TDR, and TKE. The energy Prandtl number sensitivity test is illustrated in the 'Results' section below for the neutral verification study.

4.4 FLUENT 6.3 Finite-Volume Method

FLUENT 6.3 uses the finite-volume (FV) method when solving the k-ε method. Other CFD software such as ANSYS uses the finite-element (FE) method. With regard to the FV method, the governing equations are thus put in an integral form applied to the control volume of each cell to obtain the instantaneous solution variables at each cell in

the mesh as compared to nodal solution variables obtained with FE solvers. Instantaneous solution variables are computed directly at cell centers with the integral FV solver. Solution values for faces are attained by interpolation (Bhaskaran & Collins, 2002). To find the solution of the instantaneous velocity in a 1D cell employing the FV integral for example, use the following formulation

$$\bar{u}_i = \frac{1}{\Delta}\int_{x-\Delta/2}^{x+\Delta/2} u_i(\xi)d\xi, \tag{45}$$

where $\bar{u}_i$ is the cell-averaged velocity in the i-th direction, Δ is the distance from cell centers, $x + \Delta/2$ is an unknown node value downstream the cell center, $x - \Delta/2$ is an unknown node value upstream the cell center, u_i is the instantaneous velocity in the i-th direction, and ξ is an element in the 1D cell. The cell centers are taken as x in this derivation. Then the approximation is employed that relates the cell-averaged values to the cell center values, such as $\bar{u}_i \approx u_i(x)$, where x is taken as the location of any cell center. By interpolation, nodal values are approximated using an expression similar to $u_i(x + \Delta/2) \approx \frac{u_i(x+\Delta)+ u_i(x)}{2}$ (Laurence & Uribe, 2011).

5 Mesh Characteristics

In this paper, three non-uniform grids are generated—two in 2D and a third in 3D. The 2D domains are built from a rectangular plane with dimensions 425 m x 180 m and 5000 m x 500 m in the x- and y-direction, respectively, where the x-direction is streamwise and the y-direction is vertical. The small 2D domain is nominated the 2D(S) domain, while the large 2D domain is called the 2D(L) domain. The z-direction mentioned later is taken lateral or cross-stream. The 2D(S) mesh is discretized with a 2.5 uniform spacing for a total of 170 quadrilateral cells in the streamwise direction. At the bottom surface the vertical gradients are large and various vertical mesh sizes are considered to accommodate the vertical gradient sensitivity present in all boundary layers (Andrén *et al.*, 1994; Alinot & Masson, 2005; Hargreaves & Wright, 2007; Blocken *et al*., 2007). The vertical length discretization for the 2D(S) domain is non-uniform consisting of 110 quadrilateral cells. The first cell has a spacing of 0.6 m, and the last cell has a spacing of 5.6 m. This particular mesh scheme is identified in the Alinot & Masson (2005) paper with which the author of this paper compares results. Therefore, it is advantageous to utilize the same mesh characteristics. Although it is common knowledge that non-uniform meshes can be commuted for those with uniform vertical cell spacing between 15-30 m when employing unsteady LES solvers, e.g., Moeng & Sullivan (1994), Andrén *et al.* (1994), and Churchfield *et al*. (2010), maximum accuracy in the surface layer necessitates a fine discretization. Met mast are constructed 60 to 100 m and taller containing flow measuring equipment at various heights, e.g., 15, 30, 45, and 55 m, for the processing of site-specific wind profiles and other flow variables. Thus, the

performance of a simulation using a domain with a boundary layer or non-uniform vertical mesh spacing within the surface layer is pursued and reported in this paper.

The 3D mesh is a novelty amalgamated from Hargreaves & Wright (2007), O'Sullivan *et al.* (2011), and Moeng *et al.* (2007). The novel 3D mesh is constructed from a rectangular brick with the dimensions 5000 m x 500 m x 5000 m in the x-, y-, and z-direction, respectively. The streamwise and lateral lengths are uniformly spaced hexahedral cells. The vertical edge is comprised of 50 non-uniform hexahedral cells with a vertical stretching ratio of 1.076 and the first cell set 1 m from the ground. The specifications in the bottom panel of Figure 5.1 are taken from an intercomparison between Hargreaves & Wright (2007) and O'Sullivan *et al.* (2011). Both follow the same consistency practice for boundary conditions, i.e., velocity inlet, bottom rough wall, 0 Pa pressure gradient outlet, sidewall symmetry, and specified shear top condition. However, following the precondition to avoid generating an IBL, Hargreaves & Wright (2007) selects the first cell height of 1 m and the boundary mesh stretches at a ratio of 1.076 for a total of 50 cells and total length of 500 m. The lengthwise edge is shared by both authors extending 5000 m with 500 cells given a uniform spacing of 10 m, but this uniform spacing is doubled to reduce the number of computational cells and processing time. Thus, the streamwise uniform spacing is 20 m, and this spacing is set for the lateral edge also. Care should be taken when selecting the lateral edge's length. For example, the lateral edge comprising the O'Sullivan *et al.* (2011) domain is noted as quite thin and contains only 1 cell in the cross-stream span; thus, this domain is not suitable for steady and unsteady simulations due to the fact that the 3D lateral flow dynamics and turbulence is prevented from reaching a steady and authentic nature. The remedy to this issue is to

alter the horizontal dimensions of the domain until they are greater than or equal to five times the expected boundary layer height or larger (Moeng *et al*., 2007). In general, the boundary layer height of a CBL at Horns Rev is taken as 500 m (Gryning *et al.*, 2007); therefore, a proposed 3D domain that meets the Moeng *et al.* (2007) specifications is 5000 m x 500 m x 5000 m.

Additionally, a second 2D domain, 2D(L), is built so that any downstream or vertical sensitivity or numerical error due to the boundary conditions can be identified before expanding the 2D(L) mesh to a 3D domain. The 2D(L) domain has the same spatial discretization as the vertical and lengthwise dimensions of the 3D domain aforementioned. Each domain's characteristics are summarized in the table below. The images supplied next illustrate each domain's discretization scheme.

Table 5.1: Domain characteristics.

Mesh Name	Lx, Lz (m)	Ly (m)	Δx, Δz (m)	Δy (m)	Total Cells	Total Nodes	Disk Space (Kb)
2D(S)	425, 0	180	2.5, 0	110 cells; 0.6m at ground; 5.6m at top	18,700; Quadrilateral	18,981	1,573
2D(L)	5000, 0	500	20, 0	50 cells; 1m at ground; 1.076 ratio	12,750; Quadrilateral	13,052	1,068
3D	5000, 5000	500	20, 20	50 cells; 1m at ground; 1.076 ratio	3,187,500; Hexahedral	3,276,052	668,377

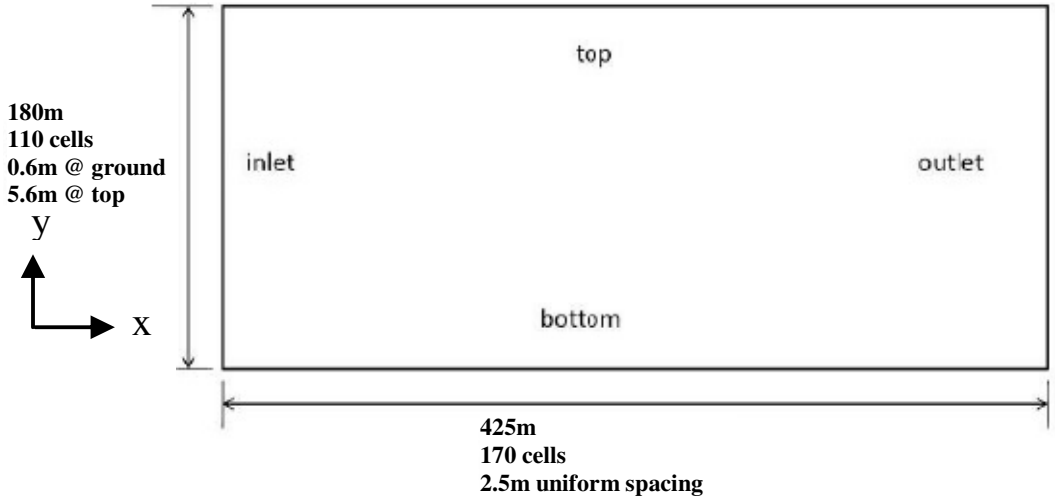

Figure 5.1: Illustration of 2D(S) domain.

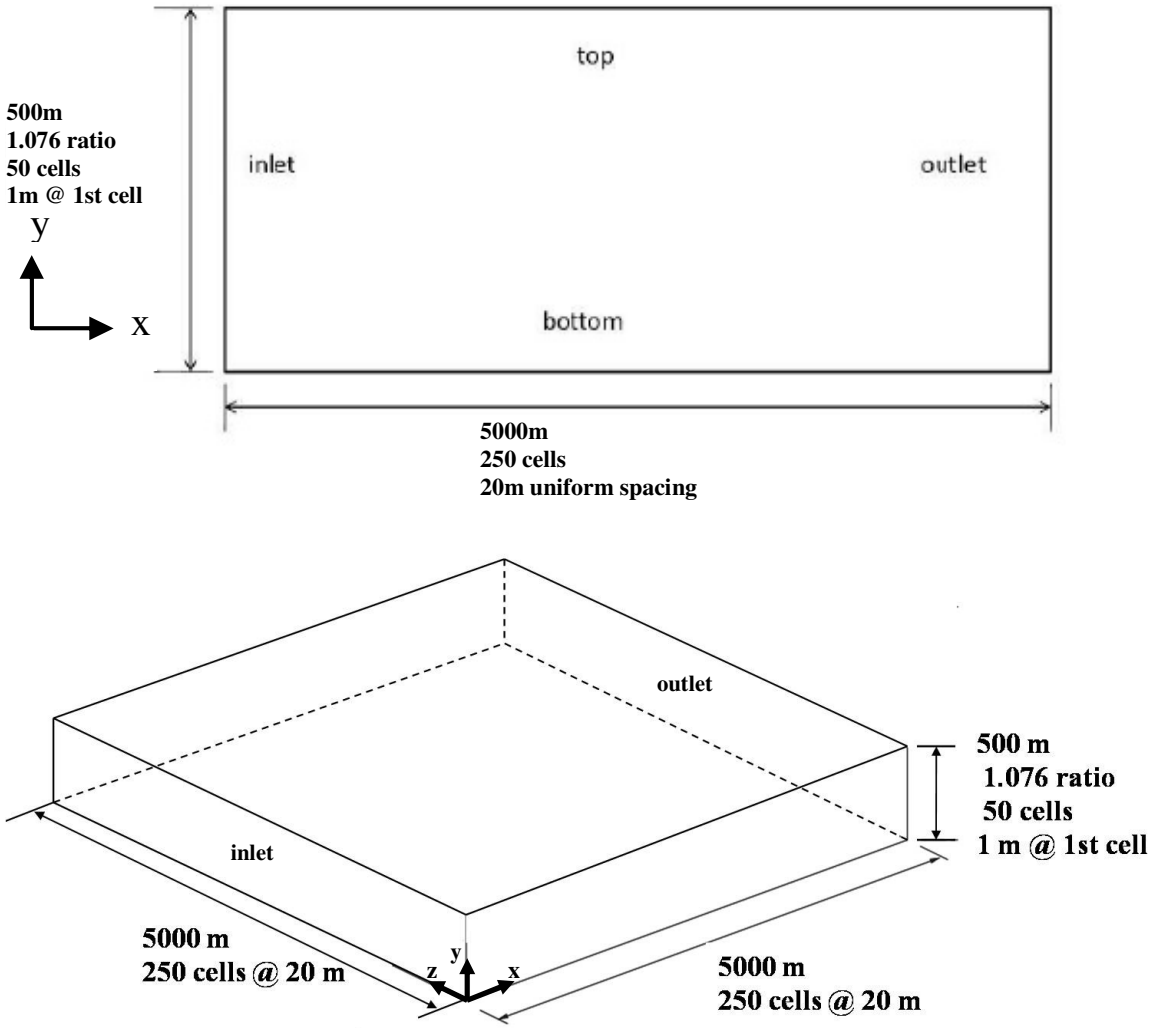

Figure 5.2: Illustrations of 2D(L) and 3D domains.

The 2D(L) domain is only used to explore the consistency of the velocity inlet boundary conditions and initial conditions, and simulations run on this domain are not reported on in any other subsection in the 'Results' section except for the 'Consistency of Velocity Inlet Boundary Conditions' subsection. The results of the neutral and unstable verification simulations obtained from the 2D(S) domain are utilized instead to see how well this paper's solutions align with Alinot & Masson (2005) results employing the same 2D domain.

6 Flow Characteristics

The flow is modeled as incompressible, subsonic, turbulent, thermally diffusive and buoyant. The Boussinesq approximation assumes the following relation

$$\Delta\rho = 0, \tag{46}$$

where Δ is the gradient operator. This approximation states that with respect to inertial terms the density remains unchanged, i.e., the flow is incompressible. The Boussinesq approximation is an additional flow condition considered since this simplification is commonly applied to buoyant and radiative flows, e.g., CBLs (Fluent Inc., 2006b). However, density gradients are not neglected with the gravitational acceleration terms in the energy equation, TDR, and TKE equations. Additional flow quantities computed to characterize the ABL flow are the Mach number, Reynolds number, Prandtl number, bulk Richardson number, and the boundary layer height. It is noted that u_∞ is not explicitly known in ABL simulations because the velocity profile is given as a function of height and non-constant. Thus to compute the Mach and Reynolds numbers, u_∞ is taken as a range of velocities found at the first cell height and at the top height of the 2D(S), 2D(L), and 3D domains. These velocities are calculated using (14) and the reference data cited in Alinot & Masson (2005) for the neutral verification simulation. The subsequent table next presents the flow characteristics and their computed quantities for the neutral verification case for all meshes.

Table 6.1 Flow quantities and parameters for the neutral verification case.

Flow Condition or Flow Parameter	Quantity	
	2D(S) Domain - Neutral	**2D(L) & 3D Domains - Neutral**
Boussinesq Approximation, i.e., Incompressible	$\Delta\rho = 0 \rightarrow \rho = \text{const} = 1.225\ \text{kg/m}^3$	
Subsonic & Incompressible	$\text{Ma} \approx 0.0172 - 0.0343$	$\text{Ma} \approx 0.0188 - 0.0373$
Turbulent	$\text{Re} \approx 1.695\text{e}8 - 3.374\text{e}8$	$\text{Re} \approx 2.171\text{e}8 - 4.323\text{e}8$
Thermally Diffusive	$Pr \approx 0.748$	
Buoyant – Neutral or Near Unstable	$R_B \approx -6.024e-4$	
Boundary Layer Height	$y_i \approx 180\ m$ (height of domain)	$y_i \approx 500\ m$ (height of domain)

In more detail, *Ma* is the Mach number and is found using the relation below

$$Ma = \frac{u_\infty}{a}, \tag{47}$$

where $a = 340.3\ m/s$ is the speed of sound (Tennekes & Lumley, 1972). This parameter indicates if a flow is incompressible, i.e. $Ma < 0.2 - 0.3$. Also, for Mach numbers less than one, the flow is subsonic, incapable of producing shock waves. The constant *Re* is the Reynolds number defined below as

$$Re = \frac{\rho L u_\infty}{\mu}, \tag{48}$$

where *L* is the characteristic length scale equivalent to the length of the domain, 425 m in the 2D(S) mesh and 5000 m in the 2D(L) and 3D meshes. The other constants have been previously discussed (Tennekes & Lumley, 1972). The flow is obviously turbulent, and in fact this range is unable to be modeled in the laboratory, thus leading to the usefulness of CFD to simulate these high Reynolds number flows, i.e., 10^8 and higher. The constant *Pr* is the Prandtl number given by the following equation

$$Pr = \frac{c_p \mu}{k}, \tag{49}$$

where the constants have been aforementioned. The Prandtl number is the measure of the viscous diffusivity to the thermal diffusivity. For air, the Prandtl number is generally 0.7-0.8, thereby signifying this fluid is more thermally diffusive (Tennekes & Lumley, 1972). A formulation of the Richardson number commonly employed to examine unstable ABLs is the bulk Richardson number expressed below as

$$R_{B,\text{Larsén}} = \frac{g}{T}\frac{(\mathrm{T}-\mathrm{T_W})}{z}/(\frac{U}{z})^2, \tag{50}$$

and was previously mentioned by equation (10) in its simplest form (Larsén *et al.*, 2011), where $T = T(15\ m)$, $U = U(15\ m)$, and $z = 15\ m$. If $R_B \leq 0$, then buoyancy should be taken into account. Furthermore, if $R_B \sim 0$ and negative, the flow is neutral and buoyant, or near unstable, which is verified in Table 6.1. For larger negative R_B values, the flow is solely unstable and strongly buoyant. If $R_B > 0$, the flow is stable. The last constant is the boundary layer height and was discussed previously. This quantity is taken as the height of the domain since no distinguishable change in the sign of the gradient of the total heat flux at the top of the boundary layer is noticed.

7 Boundary Conditions and Prescribed Quantities

The flow is initialized at the inlet from the MO theory equations of velocity, temperature, TDR, and TKE computed from reference data provided in Alinot & Masson (2005) or averaged data in Peña *et al.* (2008) applied to equations (14), (18), (19), and (21). The inlet, outlet, top, and lateral boundaries are prescribed as velocity inlets. The u, T, TDR, and TKE components are prescribed using a boundary .txt profile file (an example is supplied in Appendix D), while the y-component of velocity, v, and z-component, w, are set equal to zero. The FLUENT 6.3 User's Guide reveals that it may be amenable for some simulations to supplant the typical outflow or pressure outlet boundary conditions with a velocity inlet condition if the flow variables are known beforehand, which is true for this paper's simulations. This is a limited aspect of the solution approach. If the user would like to model flow around structures such as wind farms, then the typical nomination of outflow as the outlet boundary condition is necessary because obviously the flow at the inlet will not be the same as the flow at the outlet once it is fed through the wind farm. But for this manuscript, the flow variables at the outlet and top are known beforehand and are not expected to change due to impingement of an obstacle downstream. The velocity inlet prescription at the outlet is similar to a strong outflow condition. It is a strong condition since FLUENT imposes the user input normal velocity component, e.g., the u component entered by the user at the outlet is retained. It is also an outflow condition since FLUENT applies the upstream solution of the remaining components at the outlet, e.g., v, w, T, TDR, and TKE. A similar approach is taken at the lateral edges and the top of the domain, which are specified as velocity inlets, except that the normal velocity component is now retained for

the user input velocity, w, at the lateral edges and for the user input velocity, v, at the top. Additionally, any reverse flow scenarios are not impeded from developing, e.g., the flow may still exit out the outlet. To reiterate, when the normal flow variables are not known beforehand, such as cases of flow around structures, the velocity inlet condition at the outlet should be changed to the typical outflow condition, while the velocity inlet condition at the lateral edges can be set to a symmetry condition (Alinot & Masson, 2005; Fluent Inc., 2006b; & Hargreaves & Wright, 2007).

The bottom surface is specified as a no-slip boundary. The roughness height is set without the use of the Charnock constant when implementing the Alinot & Masson (2005) reference data because this data is not delineated as marine. However, when employing the Peña *et al.* (2008) data, it is pertinent to set the roughness height value inclusive of the Charnock constant since this data is marine. Also, the temperature at the bottom wall is fixed to that computed by the theoretical MO equations and reference data. For the neutral simulations, the elected wall temperature is 290 K and is not explicitly supplied in Alinot & Masson (2005).

A note on the prescription of consistent boundary conditions at the top—it is well-established that ABL simulations using a top symmetry boundary condition yield incorrect flow profiles. Nevertheless, as Hargreaves & Wright (2007) writes:

> Richards and Hoxey state that a shear stress should be applied at the top of the domain, but since many practitioners ignore this requirement, it was decided that a symmetry condition would suffice for this demonstration. A shear stress condition is implemented later in this work.

Attempts were made to compute the shear at the top outlined in a second publication, O'Sullivan *et al.* (2011); however, heightened accuracy could not be gained compared to that obtained when setting the top as a velocity inlet and secondly after fixing the top 4 m to the corresponding velocity, temperature, TDR, and TKE values for the entire interior of each domain. "Fixing the values of variables" in the interior of the domain is explained in the FLUENT 6.3 User's Guide (Fluent Inc., 2006). This methodology produces a turbulent viscosity profile that is sustained from the inlet to the outlet, which consequently assures a heightened accuracy in the TKE and TDR profiles since the turbulent viscosity is linked to the TKE and TDR, but at the tradeoff of a larger magnitude in the interior for the unintended vertical velocity gradient, V(y), which is discussed in detail in the 'Results' section. Additionally, when using the 3D domain, symmetry conditions are commonly applied to the lateral sides complementing the boundary prescription proposed by Hargreaves & Wright (2007) and O'Sullivan *et al.* (2011). Similar accuracy is simulated when utilizing the velocity inlet condition at the lateral edges and is the elected lateral boundary specification chosen by this paper's author. The numerical error and unintended gradients encountered while employing the velocity inlet boundary conditions are highlighted in the 'Results' section. Recall that when the application of an ABL simulation is to model flow around a structure that the velocity inlet condition at the top and the fixed cells should be changed to a symmetry condition that "will suffice" without any fixed cells to accommodate the change of the flow variables after striking the obstacle (Hargreaves & Wright, 2007).

The operating conditions are a reference pressure of 101,325 Pa and an operating density of 1.225 kg/m^3. To account for any effects due to thermal stratification of the

domain, the gravity and Boussinesq options are activated. The auxiliary material properties for air are the following:

- $C_p = 1006.43\, Jkg^{-1}K^{-1}$
- $k = 0.0242\, Wm^{-1}K^{-1}$
- $\beta = \frac{1}{T_w}\, K^{-1}$
- $\mu = 1.8e-5\, kgm^{-1}s^{-1}$

8 Solution Approach and Numerical Schemes

The solution approach utilized in FLUENT 6.3 implements the steady, standard k-ε solver with the energy, gravity, and Boussinesq options activated on two meshes until a convergence criteria of 1e-6 for all residuals is met. To achieve second order accuracy, the numerical schemes chosen for the steady solver are SIMPLEC for the pressure-velocity coupling solving scheme, PRESTO! for the pressure solving scheme, and second order upwind differencing for the momentum, energy, and turbulent transport solving scheme. PRESTO!, PREssure Staggered Option, is the preferred pressure discretization method that is conducive for convergence of ABLs since it is able to advance the solution by using a staggered grid (Crasto, 2007). It is interesting that Crasto suggests increasing the value of the maximum turbulent viscosity ratio in the 'Limits' pane, and furthermore he implies that this value is set to the maximum available in FLUENT, i.e., 1e20.

This paper's k-ε method is considered 'novel' because of the author's use of modifications to the standard code, such as altering the turbulent energy Prandtl number, which is detailed in the 'Results' section; revising the TDR Prandtl number, which is discussed in Appendix B; utilizing the k-ε method constants mentioned in Table 4.1; specifying the velocity inlet boundary condition for most edges; and setting the values of the variables in the top 4 m of the domain. Other novel modifications to the standard k-ε code are the use of a boundary profile .txt file that contains the MO theory profiles derived using (14), (18), (19), and (21) and the use of CFFs to correct the erroneous behavior of the TDR simulated profile. An example of the .txt file is supplied in Appendix D. These modifications remedy the associated anomalies originating from the

use of typical solution approaches and default k-ε method model constants. Thus, any customizations that lead to improvements in comparison to a default k-ε simulation are proposed as benchmarks for thermally stratified ABL CFD models.

9 Results

The simulated data collected is the mean velocity and temperature profiles in the streamwise direction, the TDR profile, and the TKE profile in the 2D(S) and 3D meshes. Similar results are noticed at 2500 m and 4000 m downstream of the 3D domain with a slightly weakened accuracy at larger distances downstream due to a minor deceleration of the flow in very large domains (Hargreaves & Wright, 2007). Consequently, it is elected to garner simulation results at 2500 m for heightened accuracy in the 3D mesh and at 200 m downstream in the 2D(S) mesh.

Comparison of the aforementioned output variables proceeds for the neutral and unstable flow by utilizing the Alinot & Masson (2005) dimensionless relations for the verification studies. However, at times these measures are not fitting for other simulations. Specifically, for the validation cases, new dimensionless parameterizations are created. All dimensionless relations along with their case study are grouped accordingly in the tables on the next two pages. It is noted that H is also the reference height, z_{ref}, whereas L is the MO length scale depicted in the relations. The first equation of each group is the dimensionless velocity profile, the second equation of each group is the dimensionless temperature profile, and the third and fourth equation of each group is the dimensionless TKE and TDR profiles, respectively.

After viewing the dimensionless relations, it is noticed that the dimensionless velocity and TKE are unchanged between the neutral and unstable simulations; on the other hand, the dimensionless temperature takes a different form between the unstable and neutral simulations. A point of clarification is that there are two distinct neutral validation

simulations performed in this paper—one considers an adiabatically neutral atmosphere for which $L = \infty$ and a second case represents a neutrally stratified ABL with a large negative MO length scale, i.e., $L = -1531\ m$. In the first scenario, the temperature profile maintains a constant slope, also known as the dry adiabatic lapse rate, and there is no heat flux addition at the surface. Conversely, the second case has strong thermal mixing in the surface layer that is initiated by a stiff condition, $T_w = T_0(55\ m)$, in the $T_0(z)$ profile that produces a non-zero T_*. It is desirable to illustrate how an adiabatic neutral ABL ($L = \infty$) suggested by Alinot & Masson (2005) and a non-adiabatic neutral ABL ($L \neq \infty$) detailed by Peña *et al.* (2008) perform side by side and in comparison to Horns Rev averaged wind profile data. These cases are illustrated in the following sections. Additionally, the dimensionless TDR relations have a different expression in all simulations, except in both verification and validation studies of the neutral simulations where $L = \infty$.

Table 9.1: Dimensionless relations for neutral simulations.

NEUTRAL DIMENSIONLESS RELATIONS USED FOR VERIFICATION OR VALIDATION WHEN L = ∞

$$\frac{u_o(z)}{2u_*}, \tag{51}$$

$$\frac{c_p(T_w - T_o(z))}{5(1000gz_0)} \; \boldsymbol{OR} \; \frac{c_p(T_w - T_o(z))}{20(1000gz_0)}, \tag{52}$$

$$\frac{k_o(z)}{u_*^2}, \text{ and} \tag{53}$$

$$\frac{\varepsilon_o(z)H}{u_*^3}. \tag{54}$$

NEUTRAL DIMENSIONLESS RELATIONS USED FOR VALIDATION ONLY WHEN L ≠ ∞

$$\frac{u_o(z)}{2u_*}, \tag{55}$$

$$\frac{2(T_o(z) - T_w)}{3T_*}, \tag{56}$$

$$\frac{k_o(z)}{u_*^2}, \text{ and} \tag{57}$$

$$\frac{\varepsilon_o(z)L}{10u_*^3}. \tag{58}$$

Table 9.2: Dimensionless relations for unstable simulations.

UNSTABLE DIMENSIONLESS RELATIONS USED FOR VERIFICATION ONLY

$$\frac{u_o(z)}{2u_*}, \quad \textbf{(59)}$$

$$\frac{T_o(z)-T_w}{3T_*}, \quad \textbf{(60)}$$

$$\frac{k_o(z)}{u_*^2}, \textbf{ and} \quad \textbf{(61)}$$

$$\frac{-\varepsilon_o(z)L}{u_*^3}. \quad \textbf{(62)}$$

UNSTABLE DIMENSIONLESS RELATIONS USED FOR VALIDATION ONLY

$$\frac{u_o(z)}{2u_*}, \quad \textbf{(63)}$$

$$\frac{T_o(z)-T_w}{8T_*}, \quad \textbf{(64)}$$

$$\frac{k_o(z)}{u_*^2}, \textbf{ and} \quad \textbf{(65)}$$

$$\frac{-\varepsilon_o(z)L}{2u_*^3}. \quad \textbf{(66)}$$

9.1 Convergence of Solution

The 2D(S), 2D(L), and 3D neutral verification k-ε codes converge between 600-675 iterations, respectively, for all residuals set to 1e-6. Taking more than 420 times longer than the 2D simulations, the 3D neutral simulation reaches convergence after 14 hours. The 2D neutral and unstable verification simulations converge after 2 minutes regardless of the change in the dimensions and the stability class. Meanwhile, the 3D unstable simulation takes over 16 hours to converge. The total number of iterations for the unstable cases increase by about 100 compared to the neutral cases, i.e., 700 iterations. The energy Prandtl number is fixed at the maximum value, $Pr_t = 1e20$, while the TDR Prandtl number is found using a sensitivity test of the simulated TKE results spanning the gamut of TDR Prandtl numbers from 0.5 to 1.5 to verify which TDR Prandtl number

provides the best fit in comparison to the inlet TKE simulation curve (see Appendix B for more details). The 3D domain neutral and unstable cases illustrate the best TKE results for σ_ε = 1.1, while the 2D domain displays better TKE performance at σ_ε = 1.3. The verification results are the benchmarks for the Martin k-ε validation methodology, which uses the data averaged by Peña *et al.* (2008) to rate the performance of the novel codes when weighed against genuine atmospheric data. If in fact the TDR Prandtl number is in need of more tuning, then accommodations are made in order to obtain greater accuracy. All simulations are run on one Quad-Core AMD Opteron Processor 2354. The convergence results, simulation time, Pr_t, and σ_ε values are listed in the table below.

Table 9.3: Convergence details for the neutral and unstable 2D and 3D verification simulations.

Domain	Stability Class	Pr_t	σ_ε	Iterations	Convergence	Simulation Time (hr:min)
2D(S)	Neutral Verification	1e20	1.3	600	1e-6	00:02
2D(L)	Neutral Verification	1e20	1.3	675	1e-6	00:02
3D	Neutral Verification	1e20	1.1	650	1e-6	14:20
2D(S)	Unstable Verification	1e20	1.3	700	1e-6	00:02
2D(L)	Unstable Verification	1e20	1.3	700	1e-6	00:02
3D	Unstable Verification	1e20	1.1	700	1e-6	16:00

9.2 Neutral and Unstable Verification Studies

It is elected to verify the Alinot & Masson (2005) neutral and unstable flow cases for which the flow properties, k-ε constants, and MO theory profile relation constants are found in the article. Utilization of the expressions (14), (18), (19), and (21) produces the MO theory profiles that are implemented in FLUENT as boundary profile .txt files (see Appendix D) at most of the boundaries in the 2D(S) and 3D domains.

9.2.1 Neutral Verification Study

The neutral verification simulations are performed by considering first that there is a

constant gradient in the temperature profile and no effect of the temperature, T_*, or heat flux at the wall, $\dot{q_w}$. Thus, for L=∞, the neutral stability temperature profile is modeled as adiabatic, i.e., no heat flux is generated at the wall ($\dot{q_w} = 0$ W/m^2). After reviewing the convergence details in Table 9.3 and the k-ε constants in Table 4.1, it is apparent that all simulations are run using an energy Prandtl number, Pr_t, of 1e20, which is the maximum allowed in FLUENT. The reference flow properties are issued in Table 9.4.

Table 9.4: Neutral verification study flow parameters.

Flow Parameters & Properties	Value
L	∞ m
$u_{ref}(z_{ref})$	10 ms^{-1}
$H = z_{ref}$	35 m
u_*	0.427 ms^{-1}
$T(z_{ref1}) = T_{ref1}$	290 K
z_{ref1}	0 m
$T_w = T_{ref1} = T_{op}$	290 K
T_*	0 K
κ, von Karman constant	0.42
z_0, surface roughness length	0.00188 m
E	9.793
ε_R, roughness height	$20 \cdot z_0$ = 0.0376 m
C_S, roughness constant	0.5
σ_k	1
σ_ε	2D Domain – 1.3 3D Domain – 1.1
$C_{\varepsilon 1}$	1.176
$C_{\varepsilon 2}$	1.92
C_μ	0.0333
Energy Prandtl Number	1e20
Wall Prandtl Number	1
ρ_0	1.225 kg/m^3
c_p	1006.43 J/kg-K
μ_0	1.8e-5 kg/m-s
k_0, thermal conductivity	0.0242 W/m-K
$\beta = \frac{1}{T_w}$	0.00345 K^{-1}

In summary, Martin's k-ε constants closely resemble the Alinot & Masson (2005) neutral selection except alterations are made to the energy Prandtl number, Pr_t, and the TDR Prandtl number, σ_ε, in order to correctly simulate the MO theory temperature and TKE profiles, which has a tendency to become under and over approximated, respectively, after application of the default k-ε method proceeds with the Alinot & Masson (2005) specifications listed in Table 4.1. In general, the 2D(S) domain performed best at $\sigma_\varepsilon = 1.3$, while the 3D domain functioned more precisely at $\sigma_\varepsilon = 1.1$

for both neutral and unstable verification studies (see Appendix B for more details on how to approach altering the σ_ε constant in the 3D simulations).

9.2.1.1 Tuning Pr_t

It was stated previously that ABL flows naturally tend to contain a very high turbulent viscosity, which leads to a large turbulent energy Prandtl number via relation (43) (Crasto, 2007). To verify this conclusion, tuning of the turbulent energy Prandtl number, Pr_t, occurs for the neutral verification study only and behaves as the benchmark for the future unstable verification and neutral and unstable validation studies. The performance of the simulated TKE profile for the 2D(S) neutral verification study 200 m downstream is provided in the figure below and elucidates that at larger values of Pr_t, the simulated TKE profile approaches the theoretical TKE profile.

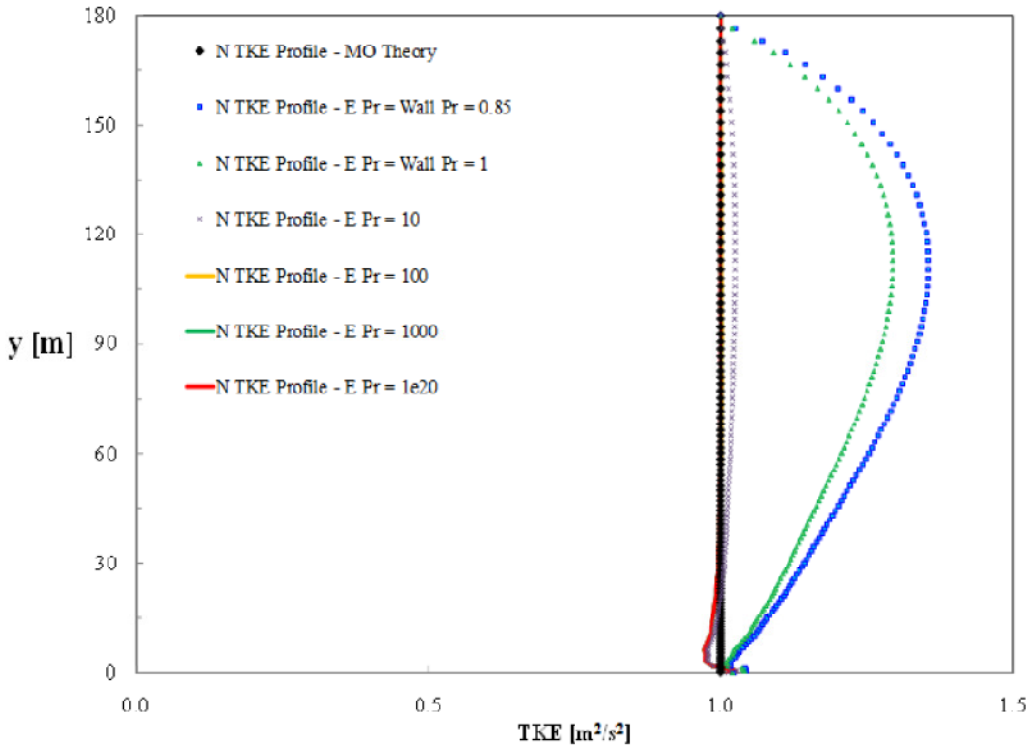

Figure 9.1: Neutral TKE profile for assorted Pr_t values.

It is clear that as Pr_t tends to infinity, the TKE simulation results reach an asymptotic maximum in accuracy. There is a slight tradeoff in the TKE simulated accuracy. In other words, the TKE profile moderately shifts to weaker values of TKE on the left of the MO TKE profile in the surface layer, i.e., 10% of the height of the domain (or 18 m). The under approximation is quite small and on the order of O(-3); therefore, it is concluded that for infinite values of Pr_t, there is only a weakly under approximation in the resultant TKE profiles at the SL. Choice of $Pr_t = 1e20$ is advised.

Furthermore, the greatest benefit after altering the turbulent energy Prandtl number is illuminated in the following image of the neutral ABL temperature profile.

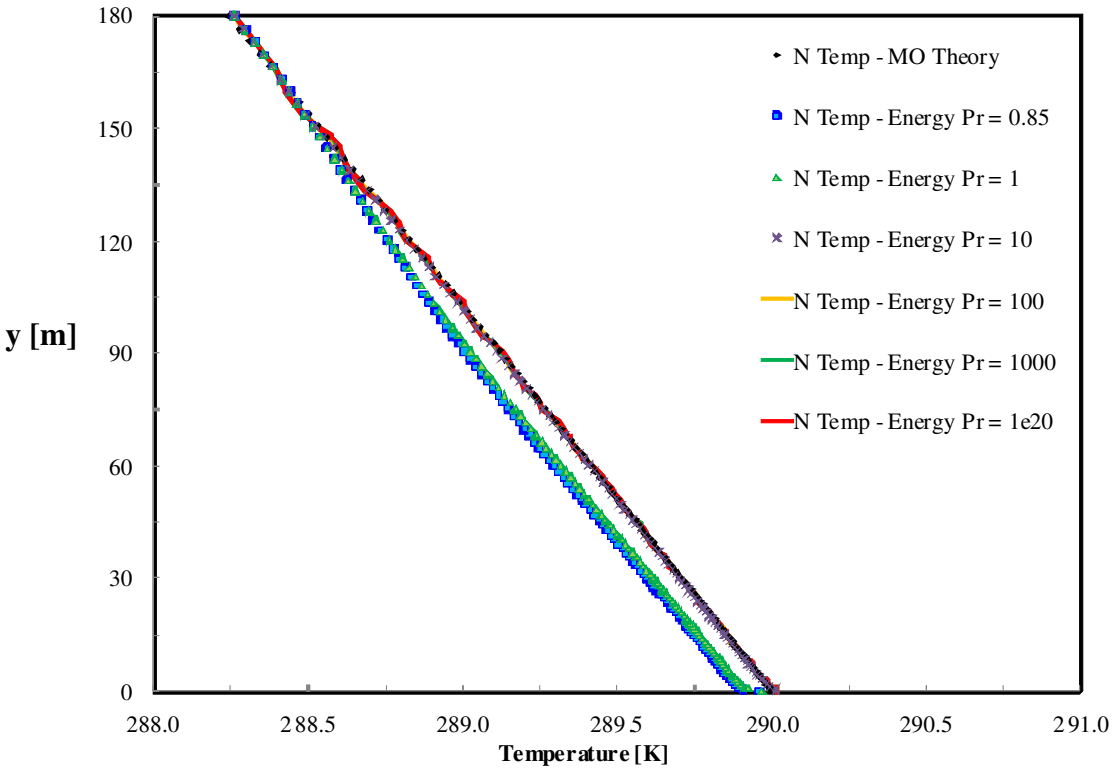

Figure 9.2: Neutral temperature profile results for assorted Pr_t values.

It is unequivocal that values in the spectrum of 10 to 1e20 yield closer approximations of the theoretical MO temperature profile, which is shown as black diamonds. Obviously,

turbulent energy Prandtl numbers of 0.85, the FLUENT default, and 1, the choice implemented by many authors prior to this paper (see Table 4.1.), simulate the temperature profile with lower values than those theorized by MO relations. Again, choice of $Pr_t = 1e20$ is advised. It should be stated that the velocity profile remains negligibly affected by varying the turbulent energy Prandtl number. Though, the TKE, temperature, and TDR profiles have trends that illustrate the need to modify Pr_t when intending to simulate neutral and unstable ABLs.

Lastly, the tendency of the dimensionless TDR profile to become more representative of the theoretical MO dimensionless TDR profile as Pr_t grows is revealed in the next image, where the x-axis is the dimensionless TDR parameter, $\frac{\varepsilon_o(z)H}{u_*^3}$, the y-axis is the dimensionless quantity, $\frac{y}{H}$, and the values of H and u_* are found in Table 9.4.

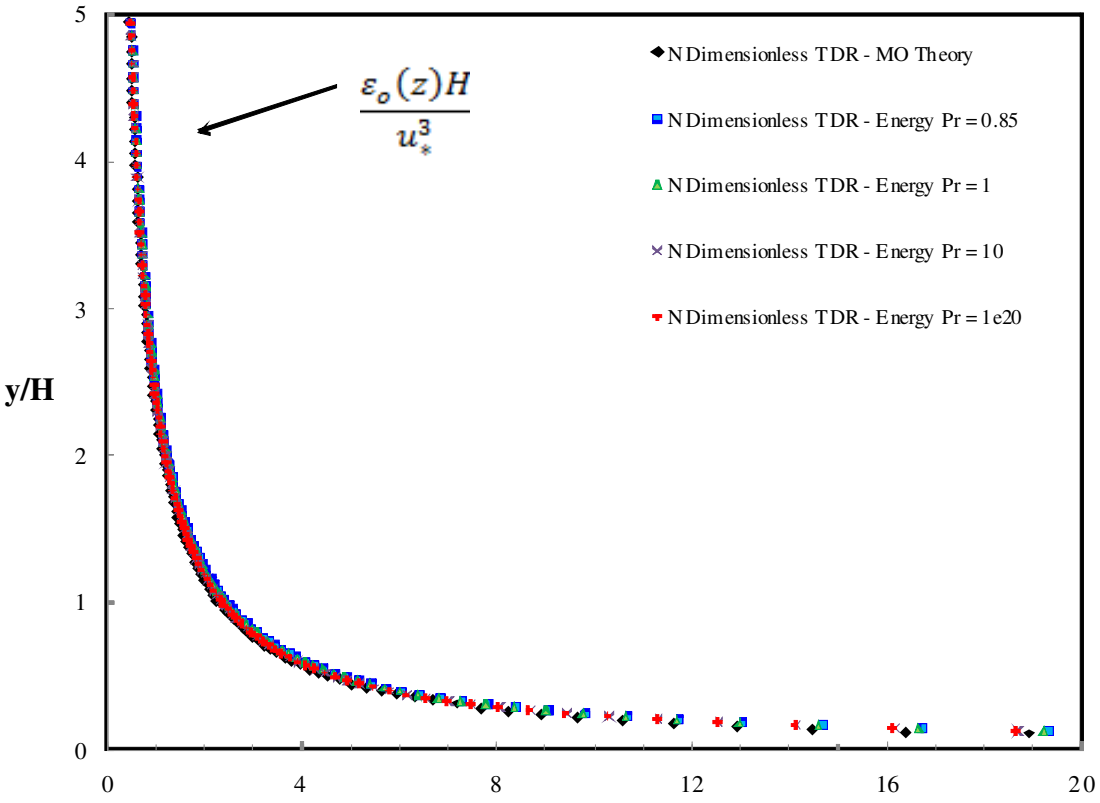

Figure 9.3: Dimensionless neutral TDR profile results for assorted Pr_t values.

9.2.1.2 Consistency of Velocity Inlet Boundary Conditions

In CFD modeling there is a constant need to minimize the unintended gradients encountered in a customized domain as a result of the spatial discretization scheme, initial conditions, and boundary conditions. It is Blocken *et al.* (2007) who claims that for accurate simulation of turbulent ABLs, the length to the center of the first cell, y_P, along the vertical edge of the domain must be designed greater than the sand grain roughness height, ε_R, and that the sand grain roughness height should be equal to 20 times the surface roughness length, i.e., $0.5\Delta y = y_P > \varepsilon_R = 20z_0$, or an IBL is generated near the surface. Application of this specification reduces the gradients at the surface. Further diminution in the surface gradients, where the shear is the strongest due to the no-slip wall condition, occurs with the implementation of the Hargreaves & Wright (2007) or the Alinot & Masson (2005) vertical edge non-uniform spatial discretization. However, complete reduction of developing gradients is not feasible, and thus, it is important for a computational fluid dynamicist to understand and quantify these gradients because they will alter the momentum through the interior of the domain having a heightened magnitude near the edges. The quantification of the unintended gradients in the vertical velocity is illustrated in both 2D domains to see how the boundary conditions might affect the solution variables. Additionally, the trend of the vertical velocity when the 2D domain is expanded in the lateral dimension in the 3D domain is investigated. It is essential to demonstrate that in spite of the enlarged length in the 2D(L) domain and the introduction of the lateral dimension in the 3D domain, the velocity inlet boundary conditions are consistent and spatial steadiness is maintained while the unintended gradients have the greatest impact at the edges.

Although the vertical velocity, V(y), is initially set to 0 m/s, this initial condition cannot be entirely satisfied throughout the whole domain due to the vast downstream and vertical size, and a small magnitude in the vertical velocity develops of O(-3) m/s in the 2D(S) and O(-2) m/s in the 2D(L) domain. The velocity contours are illustrated for both 2D domains in Figures 9.4 and 9.5. Figure 9.5 portrays the 2D(S) domain beset in the 2D(L) domain to view the pattern of the unintended gradients at the edges and within the interior of the domain in the expanded 2D domain. The small magnitudes of vertical velocity are observed in the dominant region of the interior of the 2D(L) domain in various hues of blue and detail the steadiness and consistency of the initial and boundary conditions. These velocity gradients increase slightly as a function of height, but remain constant downstream in the 2D(L) case.

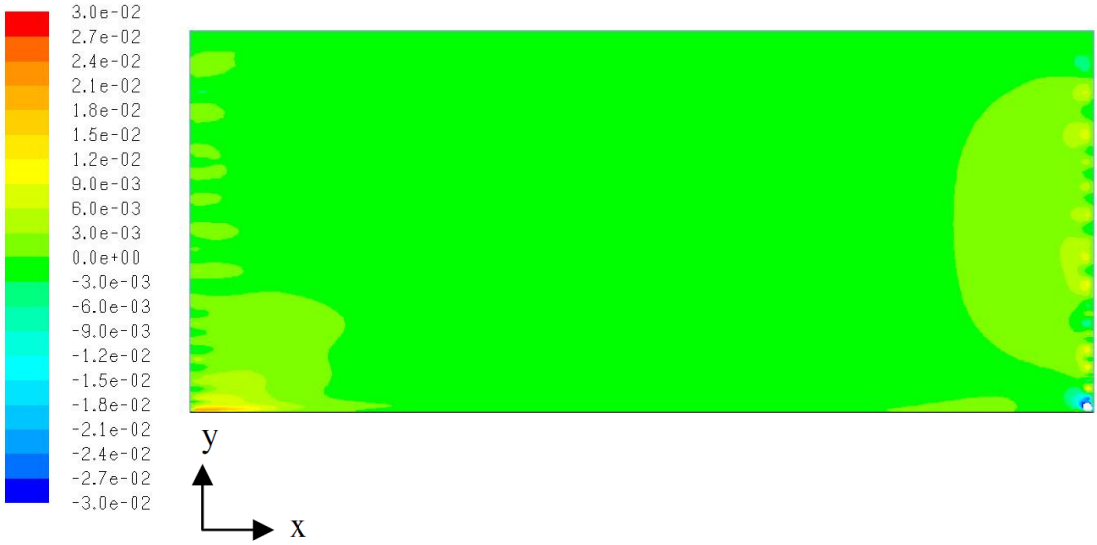

Figure 9.4: 2D(S) contours of vertical velocity, V(y), inhibiting regions near edges.

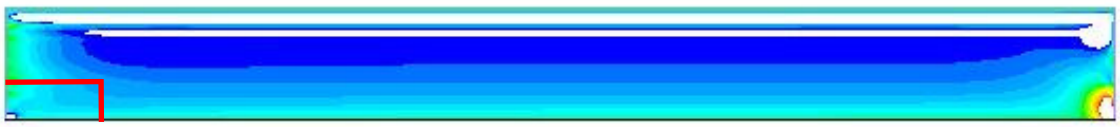

Figure 9.5: 2D(L) contours of vertical velocity. The 2D(S) domain is outlined in red at the inlet.

One may expect that the unintended vertical velocity gradients have the largest impact

for the first and last 100 m from the inlet and outlet, respectively, of the 2D(S) domain, which is verified by Figure 9.4. The heightened contour activity at the edges in the 2D(S) domain is due to the smaller geometry. The contour legend is to the left of Figure 9.4 and has been clipped to include the range -0.03 to 0.03 m/s. White regions in the contour plots represent magnitudes of velocity outside of the clipped range. The coordinate system is provided where y is the vertical direction and x is the downstream direction. The inlet is the left vertical edge, the outlet is the right vertical edge, the bottom edge is the wall surface, and the top edge is the top boundary. The coordinate system and legend are shared by Figures 9.4 and 9.5.

When the user increases the height of the domain and the length, the gradients affect a minor region near the boundaries. This is displayed in Figure 9.5 highlighting a greater region of vertical velocity development between -0.012 m/s to -0.03 m/s in various tones of blue within nearly the entire interior of the 2D(L) domain from the surface to 400 m. Meanwhile, there are regions at the inlet, outlet, and top that indicate larger magnitude gradients materialize 425 m downstream of the inlet and upstream of the outlet and 100 m from the top in the 2D(L) domain. Also viewed in Figure 9.5 is the 2D(S) geometry outlined in red and beset at the inlet. Enlarging a domain to illustrate the gradients at boundaries and within the interior is a necessary pre-processing step when constructing CFD simulations. Modeling flow in regions near boundaries can yield erroneous flow variables and minimizing gradients in the interior is desirable.

It is imperative to understand how the velocity inlet boundary conditions affect the unintended vertical velocity component when the 2D(L) domain is expanded to represent the 3D domain by including the z-dimension in the spanwise direction. It is presupposed

that the x-y plane mid-span will exhibit the same or nearly the same behavior as Figure 9.5 since the lateral velocity inlet boundary conditions are felt least at the middle of the spanwise dimension, i.e., mid-span. The mid-span x-y plane vertical velocity contours are provided in Figure 9.6 along with 100 m from each lateral edge where the unintended gradients are expected to affect the interior of the domain the most. The color contour legend is the same as that given in Figure 9.4, and the 2D(S) domain is outlined in red at the inlet of each figure.

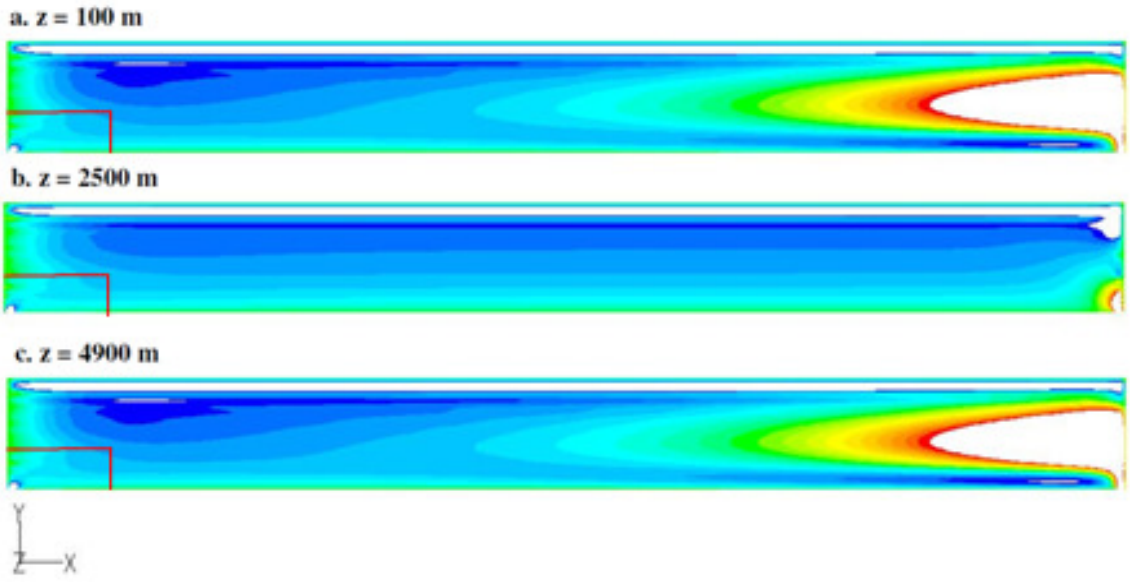

Figure 9.6: 3D domain x-y planes of vertical velocity, V(y), contours at various lateral positions.

As suggested, the middle graphic in Figure 9.6 exhibits the same trend in the vertical velocity developments as the 2D(L) domain in Figure 9.5. One can deduce immediately that the velocity inlet boundary conditions at the inlet, outlet, and top are consistent for 2D and 3D domains and supply an ample region marked by blue from which flow variables can be accurately simulated. It is important to also understand how the unintended vertical velocity gradients affect the regions away from each lateral sidewall. After viewing Figure 9.6 a. and c., it is noted that a considerably larger region is impacted

by vertical velocity gradients amounting to approximately one-third of the domain upstream from the outlet, but at 100 m from each lateral sidewall. A look at the x-z plane at various heights in the 3D domain will prove how large this region is. Figure 9.7 below provides the vertical velocity contours of x-z planes at 10, 50, 100, and 425 m altitudes.

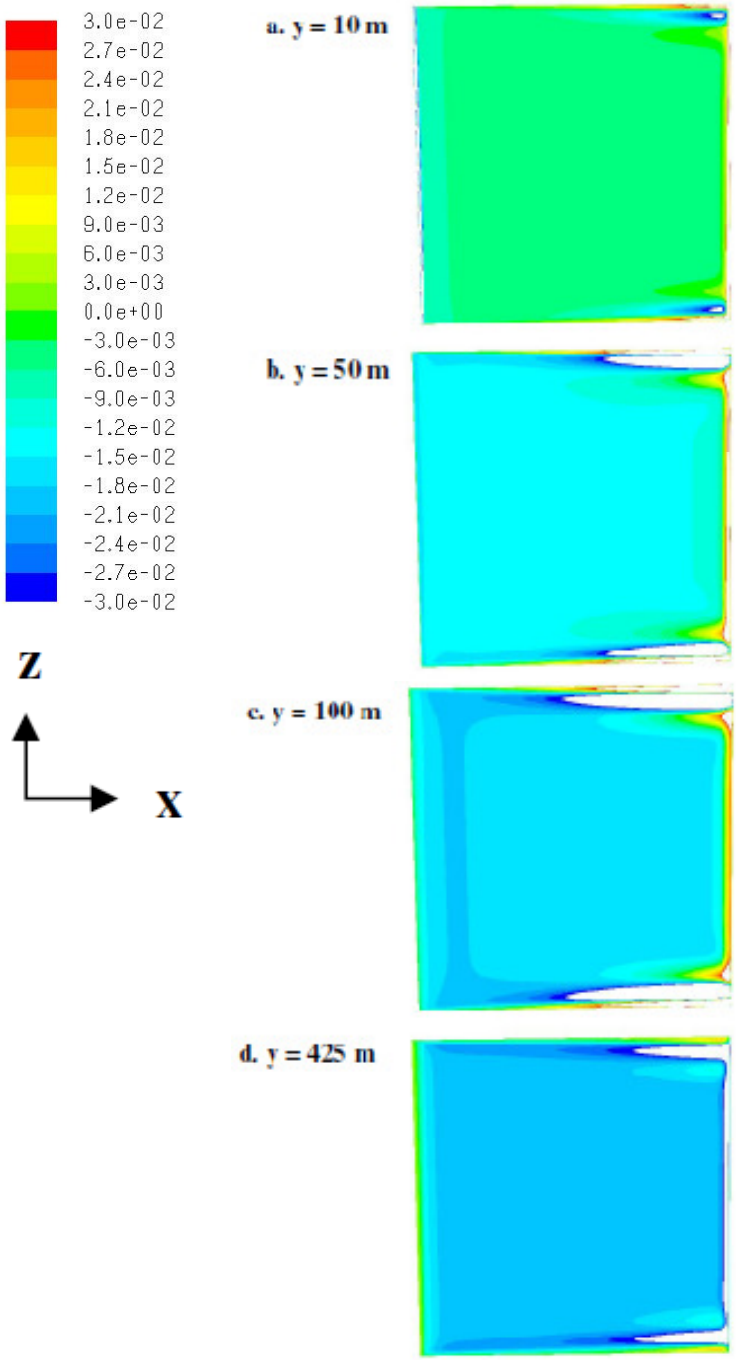

Figure 9.7: 3D domain x-z planes of vertical velocity, V(y), contours at various heights.

It is obvious from Figure 9.7 that the velocity developments only impact a fraction of the 3D domain near the lateral sidewalls for about 100 m from each edge, which can barely be viewed at the top right and bottom right of each graphic as the white regions in a. through d. These heightened velocity contours are very thin, and they do not impact much of the interior of the domain.

Next, it is noteworthy to point out a secondary instability that is only revealed in the 3D domain. This secondary development is evident in Figure 9.7 a. through c., and must be due to the effect of the velocity inlet boundary condition at the lateral sidewalls. These secondary peak velocity developments extend upstream of the outlet to about 1/20 to 1/6 of the domain from a. to c., but are non-existent in d. This means that the boundary conditions affect a larger area in the interior domain than was once thought, i.e., 100 m from each velocity inlet boundary is affected by vertical velocity development as the primary source of unintended gradients. This is still true; however, it should be clarified that these unintended gradients remain present a distance that is approximately 500 m upstream from the outlet and begin near the surface extending upward to the middle of the domain a distance of approximately 100-250 m high. The secondary peak velocities occur about 500 m from each lateral edge and range in color from green, yellow, red, and white. The white areas, which are approximately 500 m upstream from the outlet, are the hazardous regions where flow variables are impacted the most. Utilizing simulation results from these areas could lead to erroneous quantities that include the effects of the unintended vertical velocity gradients.

Finally, views of the vertical velocity behavior in the y-z planes at 100, 1000, 2500, 4000, 4300, 4500, 4700, and 4900 m are supplied in Figure 9.8 below. The color contour

legend is the same as previously shown in Figures 9.4 and 9.7 and comprises the range of velocities from -0.03 to +0.03 m/s, where green represents 0 m/s, the initial flow condition.

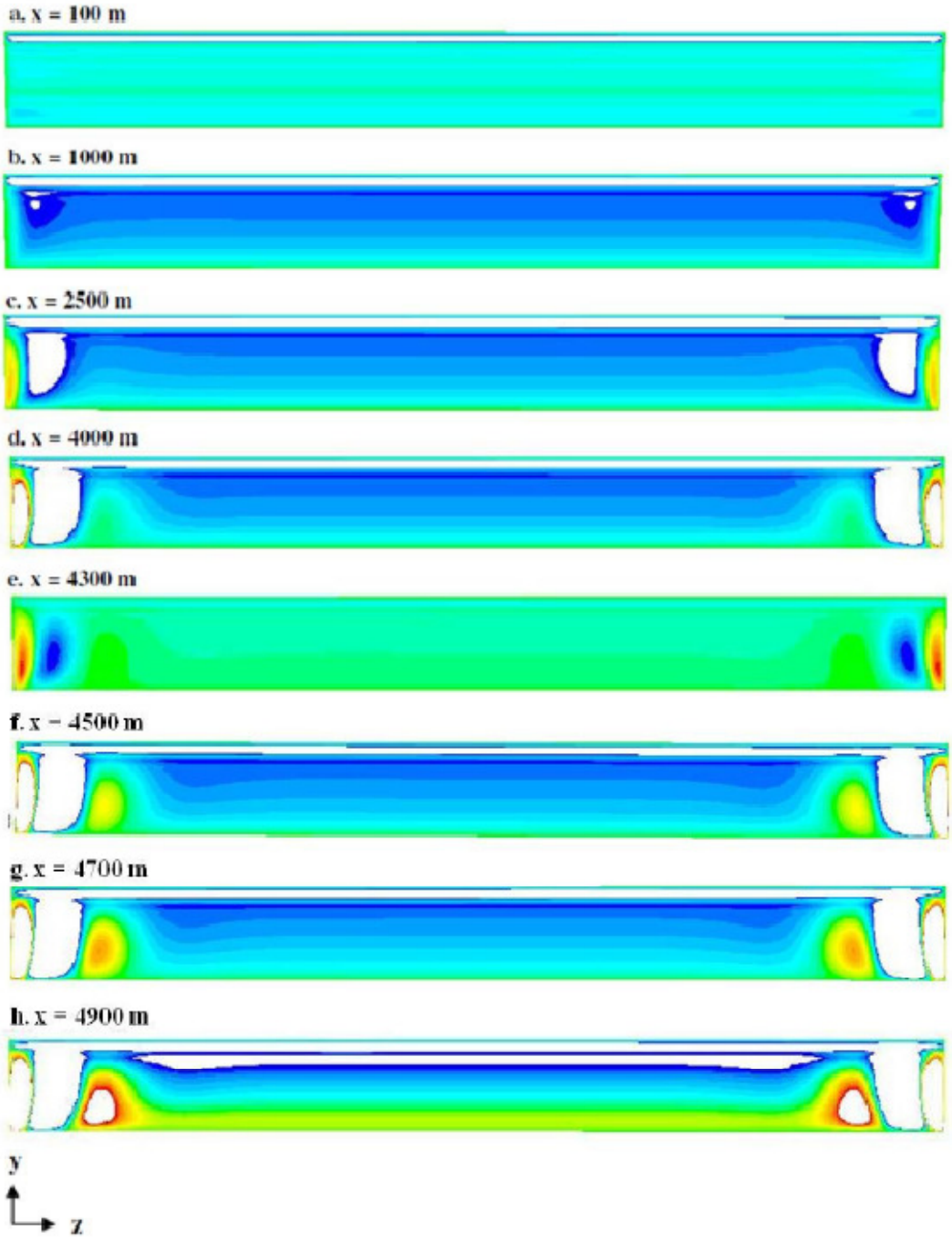

Figure 9.8: 3D domain y-z planes of vertical velocity, V(y), contours at various downstream positions.

Figure 9.8 illustrates that for the most part the interior of the domain from the inlet to 4500 m downstream gives a vertical velocity consistent with previous results that is between -0.03 and 0.03 m/s. Thereafter, from approximately 400-500 m from each lateral edge and at downstream distances between 4500 and 5000 m, the secondary peak vertical velocity component affects the interior of the domain and could add error to a user's CFD simulation of flow variables. Additionally, the primary outer velocity developments are illustrated from 2500-4900 m downstream at 100 m from each lateral edge. These unintended gradients formed as primary structures and are first discussed in Figure 9.6 a. and c.

Lastly, it is noted that these unintended gradients amount to the range -0.03 to 0.03 m/s, which is an O(-2) value and include O(-3) velocity magnitudes. This small of a scale of momentum should not cause large deviations in the flow. However, it is wise for a CFD user to verify that their 2D and 3D domain discretization scheme, initial conditions, and boundary conditions are consistent, maintain a steady nature of the flow, and sustain the original initial conditions as close as possible. It is also noted that these simulations do not develop 3D turbulent structures such as vortices and streaks. To illustrate these details, one turns to a turbulent unsteady flow solver, e.g., LES, and commences the generation of turbulence from a random turbulence generator such as the Spectral Synthesizer or the Vortex Method presently employed in FLUENT's LES unsteady solver. These two random turbulence generators disperse realistic 3D turbulent structures from the inlet throughout the entire domain. The turbulence has a velocity scale larger than the unintended gradients cited in this section, but the turbulence is smaller than the original initial velocity components themselves (Fluent Inc., 2006b).

9.2.1.3 Dimensionless Neutral Simulated Profiles

After tuning the turbulent energy Prandtl number, the Alinot & Masson (2005) neutral constants viewed in Table 9.4 are employed for the neutral ABL verification using the 2D(S) and 3D domains (see Appendix B for details on achieving a more accurate 3D simulation by altering σ_ε). The results of the dimensionless velocity, temperature, TKE, and TDR are plotted to see how well the boundary conditions, solution approach, and k-ε model constants pair with theoretical MO dimensionless profiles. It is noted that all profiles obtained using the 3D domain are laterally averaged profiles that are taken at the 2500 m downstream position. The Martin code results are compared with the Alinot & Masson (2005) proposed methodology, as well as Crespo *et al*. (1985) and Jones & Launder (1972) results and is visualized below.

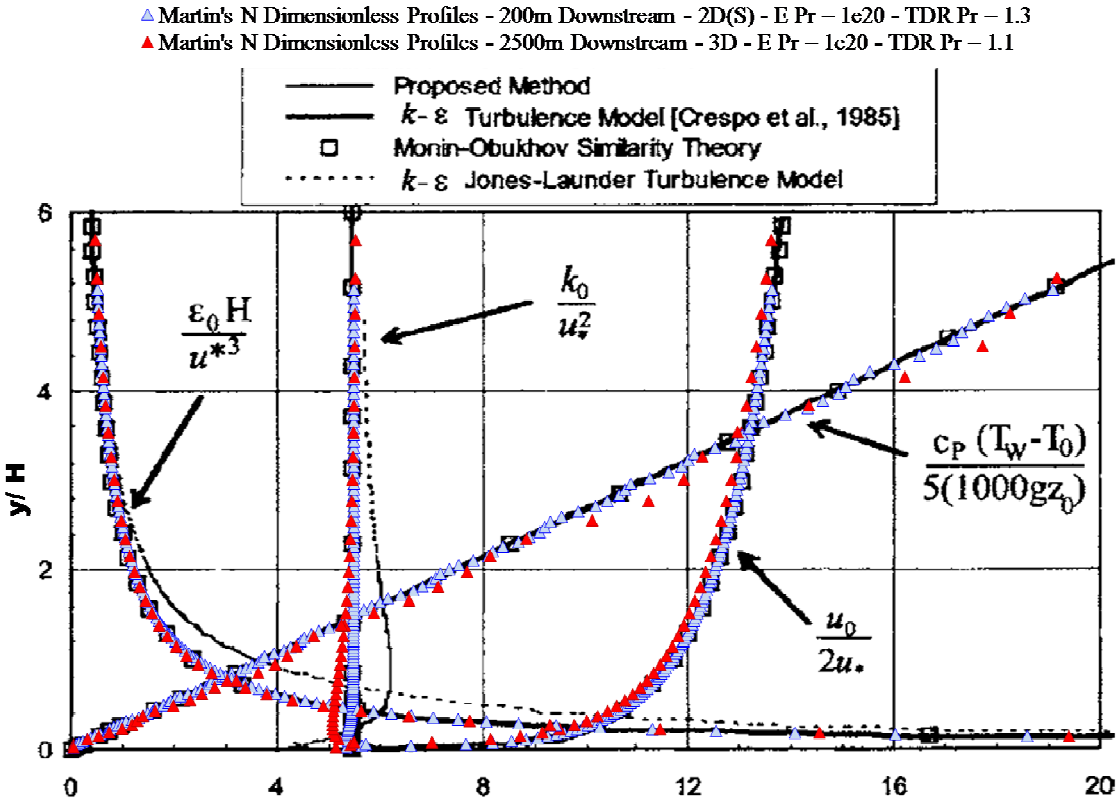

Figure 9.9: Martin's 2D(S) & 3D simulated dimensionless neutral verification results.

Although the 2D(S) domain simulation results are more accurate than those acquired with the 3D domain, it is important to note that the 3D domain, and other 3D domains fitting the Moeng *et al.* (2007) domain specifications, can bring to light the lateral flow dynamics such as vortices and streaks when applying an unsteady CFD solver like LES in combination with a random turbulence generator like the Spectral Method to the domain. The 3D simulation results expose a small overshoot in the TKE profile in the first few cells, from the surface to $y/H \approx 1.6$ that cannot be removed with the current 3D grid spacing. Grid refinement is not considered since the processing time is around 14 hours for the neutral simulation and because the TKE error between the 3D simulation results and MO theory is modest. Additionally, the simulation results for the dimensionless TKE profile outperform the k-ε Jones-Launder Turbulence Model results. There is a noticeable but minor slowdown in the velocity profile compared to MO velocity profile.

It is secondly commented that the 3D dimensionless temperature profile is over approximated after a value of $y/H \approx 2$, which leads to an under approximation of the temperature profile, T(y). The vertical cell ratio is approximately 5 2D(S) cells to 1 3D cell in this region, so the tradeoff between accuracy and vertical mesh density is acknowledged as a potential reason for the meandering of the values in the temperature profile for the 3D domain at higher values of y/H. Grid refinement for the 3D domain is not attempted since the maximum error in the temperature profile amounts to 0.16 K, while the average error is 0.02 K. The dimensionless quantities are highlighted next to the profile they represent and have been previously mentioned as (51)-(54). The data legend and original plot are taken from Alinot & Masson (2005) whose proposed code and solution approach yield more accurate results than the Martin simulations.

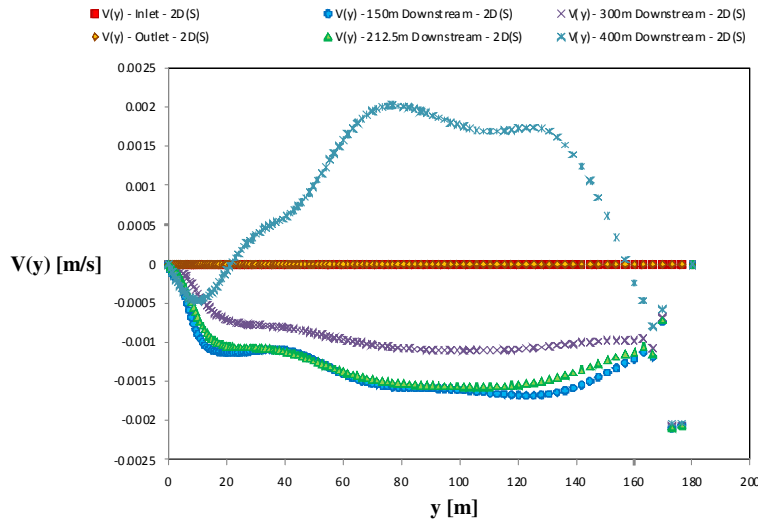

Figure 9.10: Unintended y-velocity component generated in the 2D(S) neutral simulation.

Further, the y-velocity component remains as a small anomaly caused by the boundary conditions and solution methodology that arises in both the 2D(S) and 3D models mentioned previously. The anomaly is displayed in the above plot for the 2D(S) model and exhibits a maximum velocity magnitude of O(-3), i.e., -0.002 to $0.002\ m/s$.

The y-velocity component, V(y), produced in the 3D simulation amounts to O(-2) and remains a constant negative profile as a function of height throughout the inner domain from 1000 m to 4000 m downstream, which is displayed in the next image for $\sigma_\varepsilon = 1.1$.

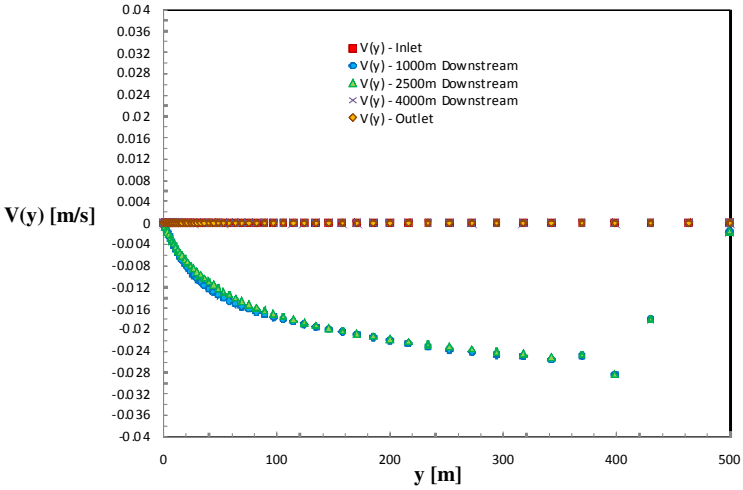

Figure 9.11: Unintended y-velocity component generated in the 3D neutral simulation.

Further, the 3D simulation generates a z-velocity component, W(y), along the height of the domain that is non-constant throughout the downstream positions 1000, 2500, and 4000 m exhibiting a maximum velocity magnitude of O(-6) at 4000 m displayed below.

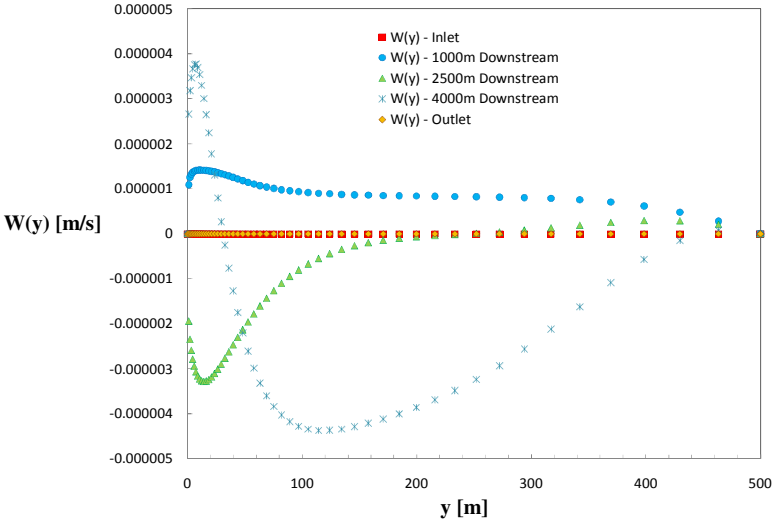

Figure 9.12: Unintended z-velocity component generated in the 3D neutral simulation.

Finally, the 3D simulation run at $\sigma_\varepsilon = 1.1$ is selected as the best suited model of a neutral ABL based on the reference flow provided by Alinot & Masson (2005) whose parameters are listed in Table 9.4 and portrayed in Figure 9.8 below.

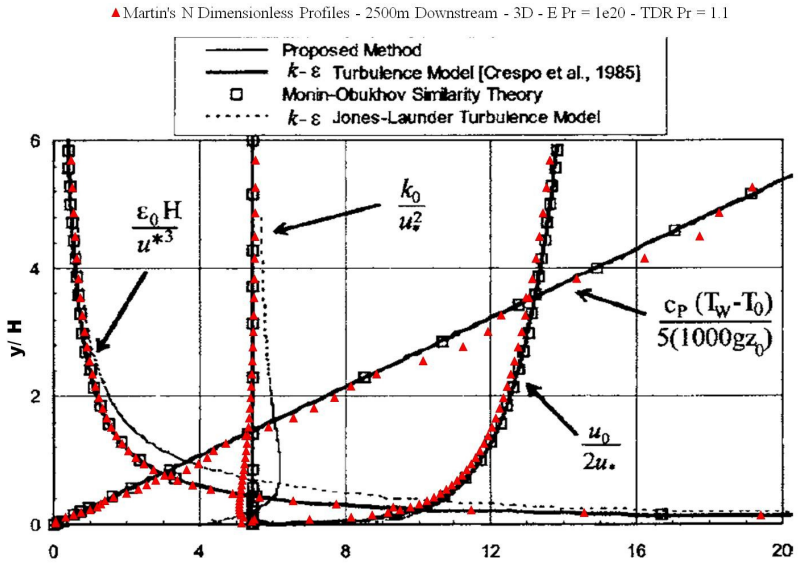

Figure 9.13: 3D neutral verification simulated dimensionless profiles for $\sigma_\varepsilon = 1.1$.

The 3D domain is employed in all validation cases studied next because of its noted accuracy and ability to model 3D ABL flow behavior when activated with an unsteady solver like LES.

9.2.2 Unstable Verification Study

Verification of the Alinot & Masson (2005) unstable data set is attempted next. The flow parameters, properties, and model constants are listed in the subsequent table.

Table 9.5: Unstable flow parameters.

Flow Parameters & Properties	Value
L	-231 m
$u_{ref}(z_{ref})$	10 ms^{-1}
$H = z_{ref}$	35 m
u_*	0.382 ms^{-1}
$T(z_{ref1}) - T_{ref1}$	287.245 K
z_{ref1}	0 m
$T_w = T_{ref1} = T_{op}$	287.245 K
T_*	-0.044 K
κ, von Karman constant	0.42
z_0, surface roughness length	4e-4 m
E	9.793
z_R, roughness height	$20 \cdot z_0 = 0.008$ m
C_S, roughness constant	0.5
σ_k	1
σ_ε	2D Domain – 1.3 3D Domain – 1.1
$C_{\varepsilon 1}$	1.176
$C_{\varepsilon 2}$	1.92
C_μ	0.0333
Energy Prandtl Number	1e20
Wall Prandtl Number	1
ρ_0	1.225 kg/m^3
c_p	1006.43 J/kg-K
μ_0	1.8e-5 kg/m-s
k_0, thermal conductivity	0.0242 W/m K
$\beta = \frac{1}{T_w}$	0.00348 K^{-1}

Martin's simulated dimensionless results are illustrated in the following figure using the dimensionless quantities (59)–(62) alongside the Alinot & Masson (2005) proposed methodology, the Crespo *et al*. (1985) results, and the MO theoretical profiles. Here again, the 2D(S) simulation is more accurate than the 3D case. But the 3D domain is a truer representation of the flow behavior of an ABL when used with unsteady CFD solvers. It is noted that all profiles obtained using the 3D domain are laterally averaged values that are taken at the 2500 m downstream position. The dimensionless velocity matches MO theory with only a weak slowdown noticed. Moreover, the dimensionless

temperature, TKE, and TDR show weak divergences in the 3D simulation compared to MO theory. The dimensionless temperature profile somewhat over approximates the MO dimensionless temperature profile with the largest errors present after *y/H*≈*2*, and it is postulated that this error could be expunged with grid refinement, but because of the long processing times and general accuracy of the simulations, grid refinement is foregone in this paper. The over approximation in the dimensionless temperature profile leads to an under approximation in the temperature profile, T(y), and it is recalled that T_* is negative. The dimensionless TKE is under approximated from the surface to *y/H*≈*1.6*, and there is a tincture of over approximation in the TKE dimensionless profile thereafter. Moreover, the dimensionless TDR profile displays the largest anomaly yet and tends to fall below the theoretical TDR profile. This leads to the need for an approach to correcting the TDR simulation results, which is expounded on in the next section.

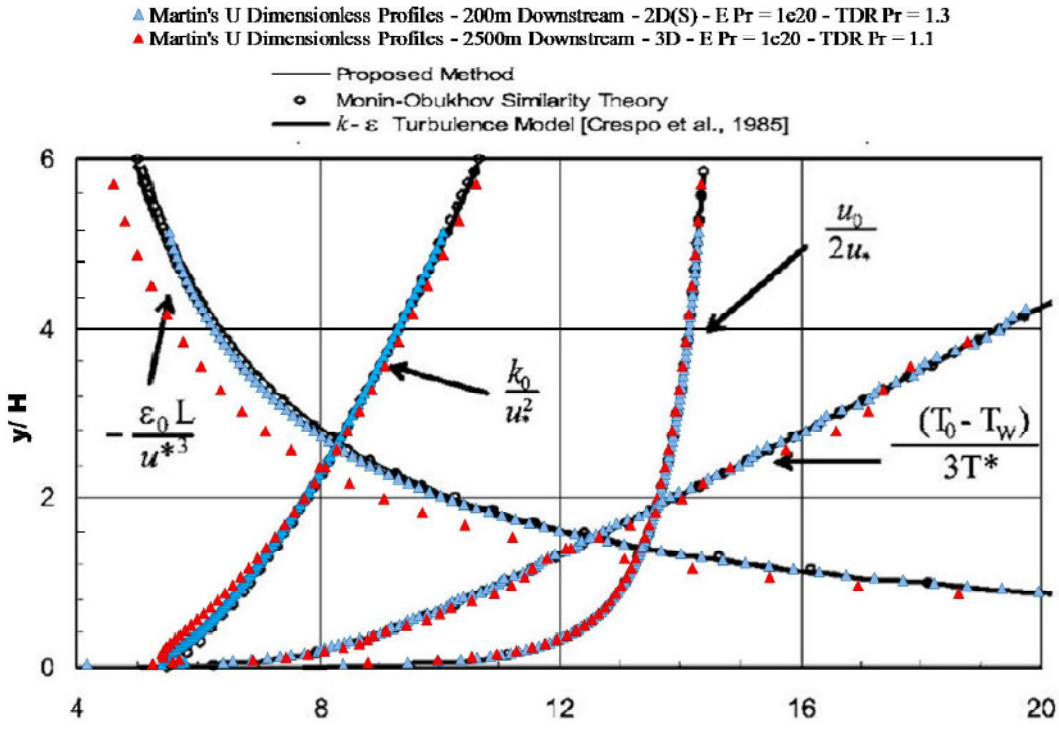

Figure 9.14: Unstable verification simulated dimensionless profiles for the 2D(S) & 3D domains.

Election of the 3D simulation methodology compared to the 2D(S) solution approach is chosen since these simulations are capable of modeling the full spectrum of average flow quantities including the lateral flow developments if exposed to a random turbulence generator. The final outcome of the 3D unstable verification simulation along with the Alinot & Masson (2005) proposed methodology, the Crespo *et al*. (1985) results, and the MO theoretical profiles are supplied in the next graphic.

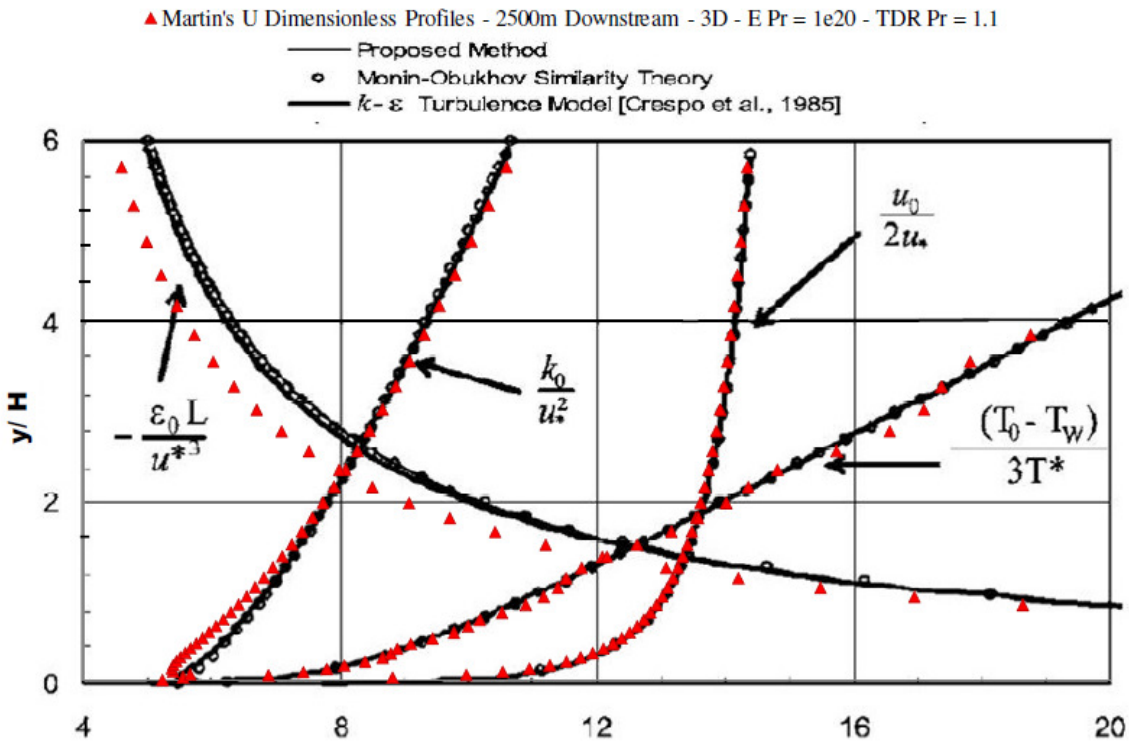

Figure 9.15: Unstable verification simulated dimensionless profiles for the 3D domain.

Additionally, the y-velocity component remains as a small development caused by the boundary conditions and solution methodology that arises in both 2D(S) and 3D simulations. The y-velocity component is displayed in the subsequent plot on the next page with a maximum velocity magnitude of O(-3) at 400 m downstream in the 2D(S) simulation, while this component amounts to a maximum velocity magnitude of O(-2) for

all downstream positions in the 3D simulation shown in the bottom figure, Figure 9.17.

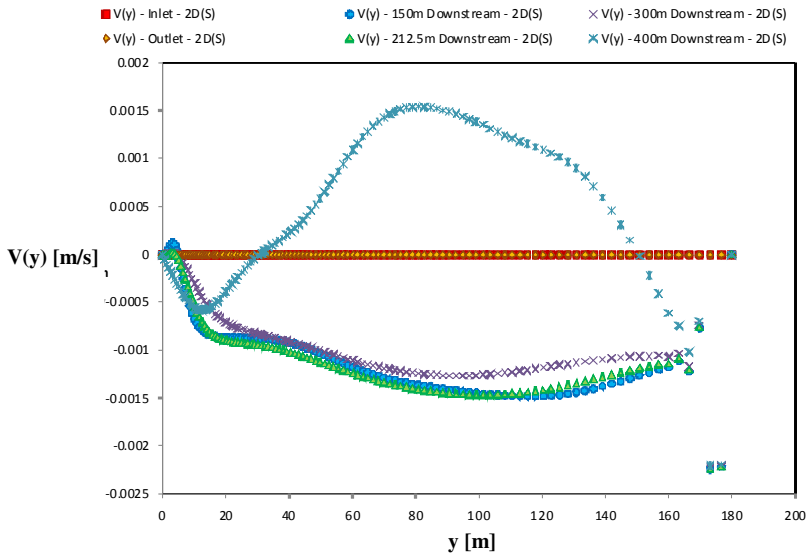

Figure 9.16: Unintended y-velocity component generated in the 2D(S) unstable simulation.

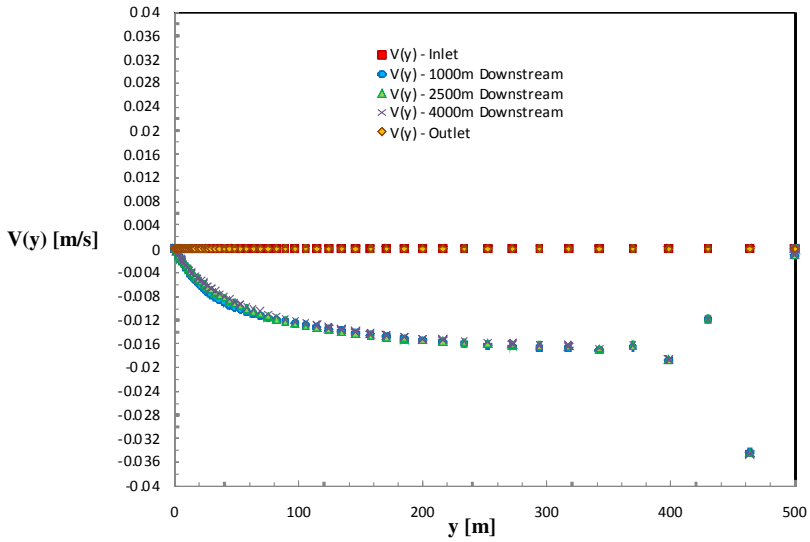

Figure 9.17: Unintended y-velocity component generated in the 3D unstable simulation.

Furthermore, there is an anomaly that totals a maximum velocity magnitude of O(-5) at 4000 m downstream in the z-velocity component viewed in Figure 9.18. These aforementioned velocity developments in the lateral and vertical dimensions are acknowledged because these quantities will have a causal effect on the average flow variables of the ABL simulations.

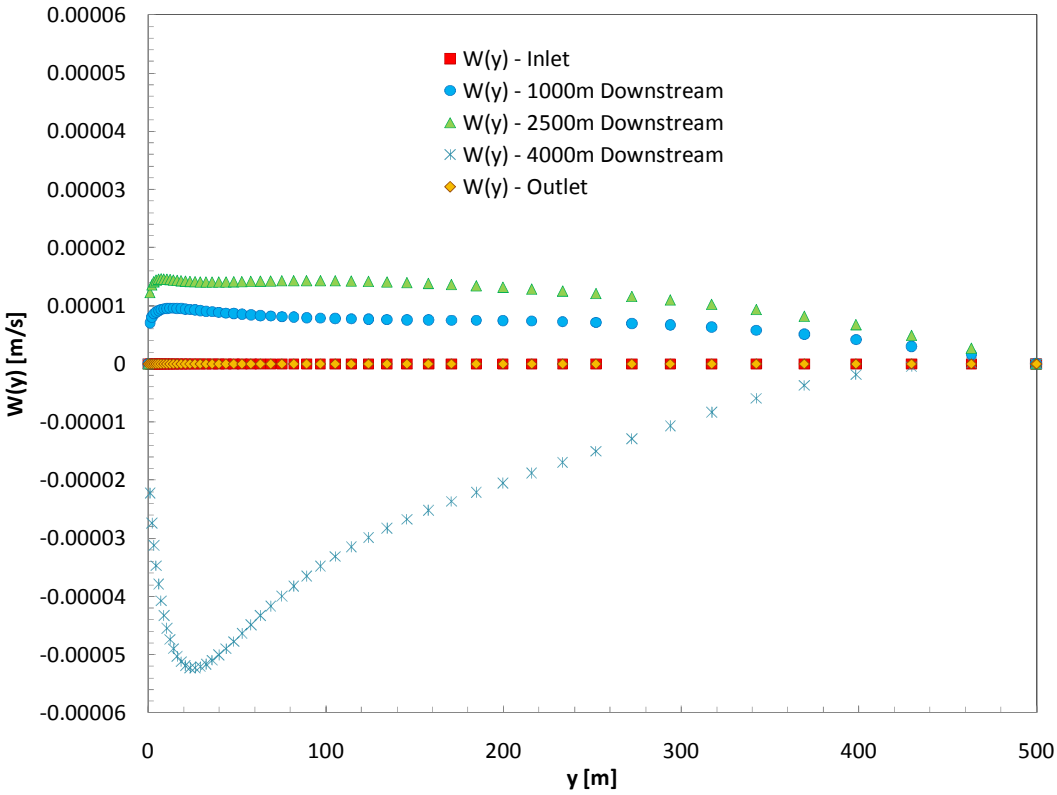

Figure 9.18: Unintended z-velocity component generated in the 3D unstable simulation.

Mentioned previously, a solution approach to improve the TDR profile is proposed. This paper's author turned to the employment of two custom field functions (CFFs) detailed in the successive section.

9.2.2.1 Correcting the Dimensionless Unstable TDR Profile

In combination with the aforementioned correction of the dimensionless TKE profile by modification of σ_ε detailed in Appendix B, a CFF that incorporates the MO TDR relation, a non-constant C_μ, and the FLUENT simulated TKE into an expression for a quantity that is dubbed the 'TDR Correction' is employed in this paper. The non-constant C_μ is called the 'Cmu Correction' because the MO TDR relation, $\varepsilon_o(z)$, is used

instead of the FLUENT output value for TDR. The 'Cmu Correction' CFF is expressed as

$$\text{Cmu Correction} = \left(\frac{\varepsilon_o(z)\kappa y}{k_{FLUENT}^{3/2}}\right)^{\frac{4}{3}}, \tag{67}$$

where $\varepsilon_o(z)$ is given by (19), y is the vertical grid point in the 3D domain, and k_{FLUENT} is the TKE values obtained after running the unstable simulation with Martin's solution approach. The equation's form is taken from the FLUENT 6.3 UDF Manual, which states that the TDR is defined in FLUENT by the following equation (Fluent Inc., 2006a)

$$\varepsilon = \frac{k^{3/2} C_\mu^{3/4}}{\kappa y}. \tag{68}$$

Equation (68) becomes the 'TDR Correction' with the following changes

$$\text{TDR Correction} = \frac{k_{FLUENT}^{3/2}(\text{Cmu Correction}^{3/4})}{\kappa y}. \tag{69}$$

At first glance, it seems that this corrector step does not suffice since the TKE has an obvious peak in the surface layer. This is true, for the values of the TDR Correction when $k_{FLUENT} \neq k_o(z)$. In these instances, the TDR Correction continues to exhibit an inaccuracy, but a reduction in error is seen throughout the remainder of the domain. For values of $k_{FLUENT} \approx k_o(z)$, which occur after about *y/H≈1.6*, the TDR Correction displays an improvement of the dimensionless TDR behavior. The subsequent plot exemplifies how the dimensionless TDR profile becomes a near-exact representation of the MO theoretical profile by utilizing CFFs (67) and (69).

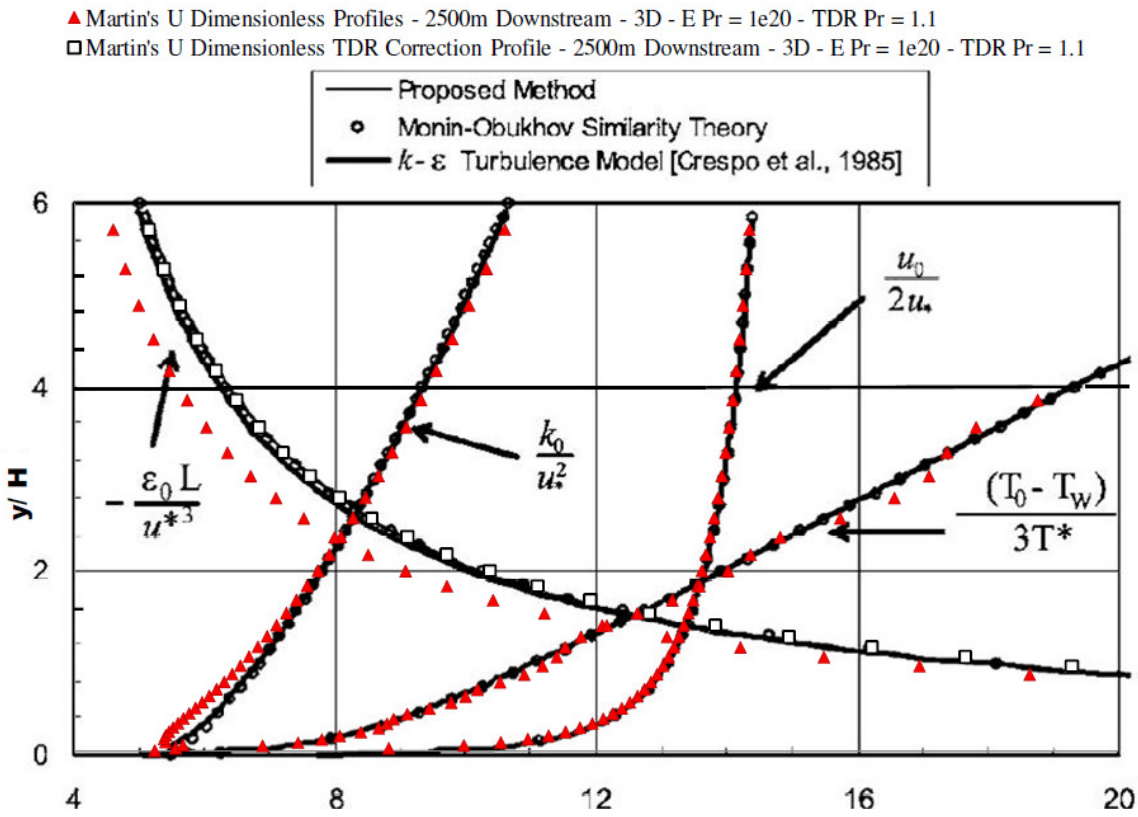

Figure 9.19: Unstable verification simulated dimensionless profiles with the TDR correction.

The unstable (U) dimensionless TDR correction profile clearly justifies the use of a simple corrector step using the two CFFs. Of course, it is better housekeeping to run two UDFs that redefine the turbulent viscosity as the MO turbulent viscosity given by (25) and a non-constant C_μ that calls on the first UDF written for the MO turbulent viscosity. The two CFFs, (67) and (69), are also benchmarks and thus are employed in all validation cases to increase the accuracy of the dimensionless TDR profiles.

9.3 Neutral and Unstable Validation Studies

Referring to Peña *et al.* (2008) and their averaged Horns Rev data set from July to October 2004 (M2 measurements only) & May to October 2006 (LiDAR & M2 measurements), both LiDAR and M2 temperature and wind profile data explained

previously are reproduced below. It is remembered that LiDAR observations are only available during the May to October 2006 data campaign; however, the average values in the table below are a conglomerate of both data campaigns where M2 and LiDAR observations are considered.

Table 9.6: Average data categorized by stability class.

Stability class	$\overline{L_b}$ [m]	$\overline{u_{*o}}$ [m s^{-1}]	u_{15} [m s^{-1}]	$\overline{z_o}$ [m]	z_i [m]	No. of Profiles
vs	28	0.12	4.94	1.9×10^{-5}	122	109
s	85	0.15	5.33	2.9×10^{-5}	150	73
ns	314	0.23	7.08	6.3×10^{-5}	223	18
n	-1531	0.40	11.10	19.6×10^{-5}	393	314
nu	-288	0.42	11.54	22.0×10^{-5}	-	600
u	-139	0.30	8.60	11.1×10^{-5}	-	544
vu	-73	0.22	6.65	6.2×10^{-5}	-	358

In Table 9.4, the averaged MO length, friction velocity, and surface roughness are used to define the MO profiles for velocity, temperature, TDR, TKE, and other stability relationships in equations (14)-(21). These parameters are computed using post-processing algorithms defined by Peña *et al.* (2008). This paper's purpose is not to verify the corrections posed by Peña *et al.* (2008); however, the graphic contains average data taken from Horns Rev in 2004 & 2006, and the k-ε simulation data is plotted along with this data to exam how well the simulations compare. Figure 9.20 highlights the averaged wind profile data at Horns Rev for each stability class and measurement height as well as the Peña *et al. (*2008) theoretical corrections for the logarithmic profile that include the sea roughness Charnock parameter, deviation in friction velocity, averaged roughness parameter, and atmospheric stability (shown as solid lines). Of most importance from this paper's perspective are the last four data markers, which represent neutral ($\bar{z}_0/\bar{L}_b$ = -1.3e-7), near unstable ($\bar{z}_0/\bar{L}_b$ = -7.7e-7), unstable ($\bar{z}_0/\bar{L}_b$ = -8.0e-7), and very unstable

($\bar{z}_0/\overline{L_b}$ = -8.5e-7) sects.

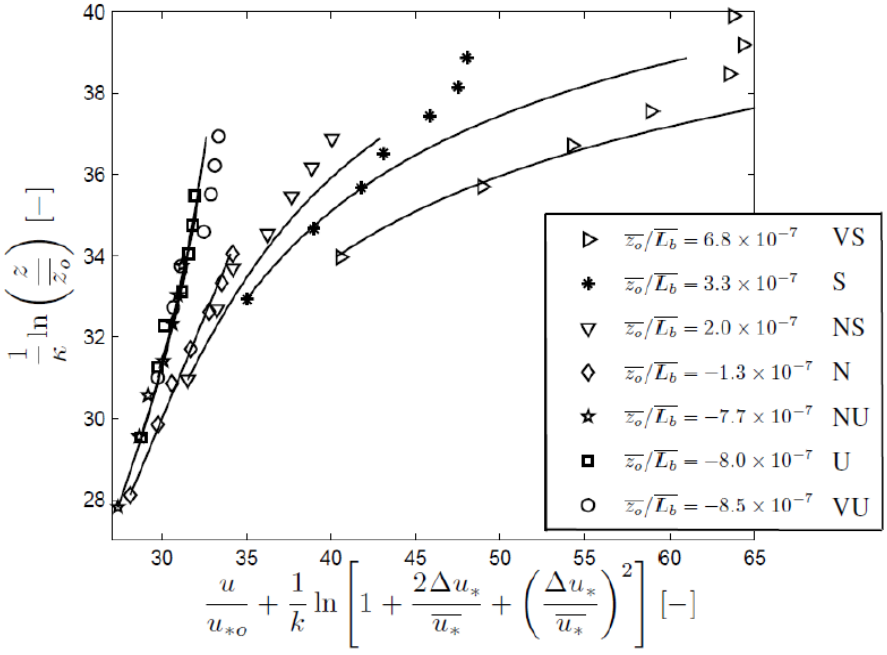

Figure 9.20: Horns Rev average data at all observation heights classified by thermal stability.

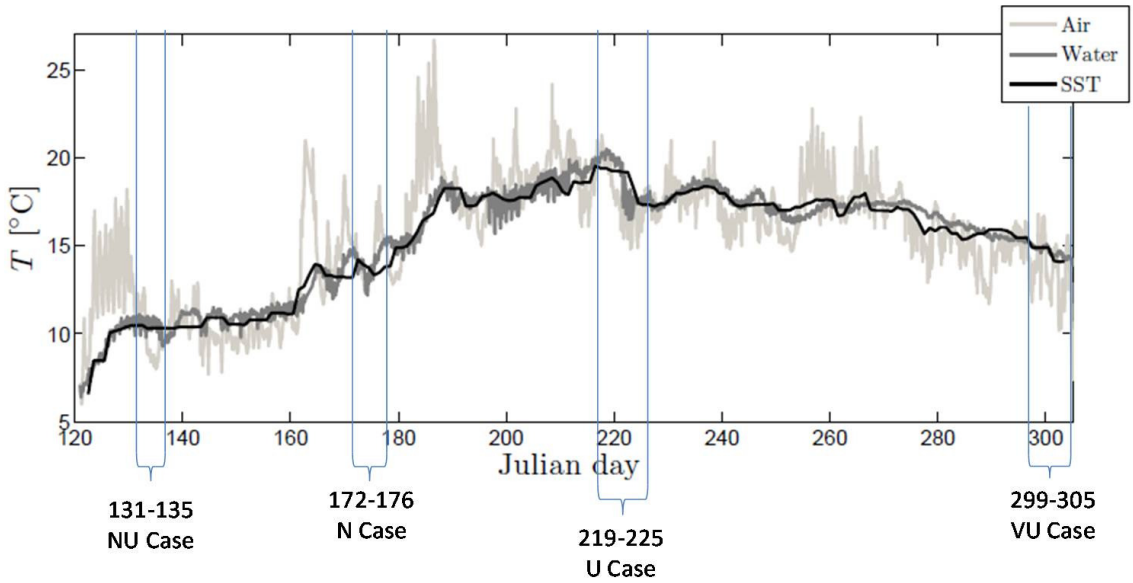

Figure 9.21: Martin's election of stability regions used to generate the MO temperature profile.

Furthermore, the temperature data provided by Peña *et al.* (2008) shown in Figure 9.21 is used to solve for T_* by placing the temperature at 55 m ASL, T(55), and that at 4 m BSL, T(-4)≈T(0)= T_W, into equation (18). The constant T_* is then easily found.

Additionally, the temperature regions from which the T_* is computed in each stability class are labeled in the figure, i.e., N-Neutral, NU-Near Unstable, U-Unstable, and VU-Very Unstable, as well as the days that comprise each stability region. The leading approach employed when identifying where a neutral, near unstable, unstable, and very unstable region exists on the temperature plot is—the larger the temperature difference between the water and the air, the more unstable the atmosphere. The selections made for this study are by no means the only regions where neutral to very unstable tendencies appear. Nevertheless, a way to determine the wall temperature and a second temperature are necessary reference data in order to generate the MO temperature profiles for each stability case. Moreover, a method to check whether the region elected is indeed in the correct stability class ensues with the computation of the bulk Richardson number, $R_{B,Larsén}$, in equation (10) mentioned previously. It is also noted that Larsén *et al.* (2011) illustrate the monthly stability classes in the figure revisited on the next page, which includes the bulk Richardson number value ranges where the extremes, dark green and green regions, correspond to unstable and very unstable classes, while light green and yellow stand for stable and very stable classes. The conclusion is made that Figure 9.22 is representative of the ambient thermal stability at Horns Rev as a whole after perusing the noted reference. It is interesting to compare Figure 9.22 with a recent review of the ambient thermal stability at Horns Rev in the spectrum 1999-2006 by Sathe *et al.* (2011) whose similar stability bar graph is provided in the bottom image on the next page and employs the bulk Richardson formulation comprising potential temperature effects given by $Ri_{B,Peña}$ aforementioned. The image illustrates the monthly stability at Horns Rev from April 1999 to December 2006. It is revealed that Sathe *et al.* (2011) has fewer unstable and greater stable frequencies than Larsén *et al.* (2011) during the winter

months, but that the general stability behavior is verified by both works from April to October, which are predominantly the VU to N classes.

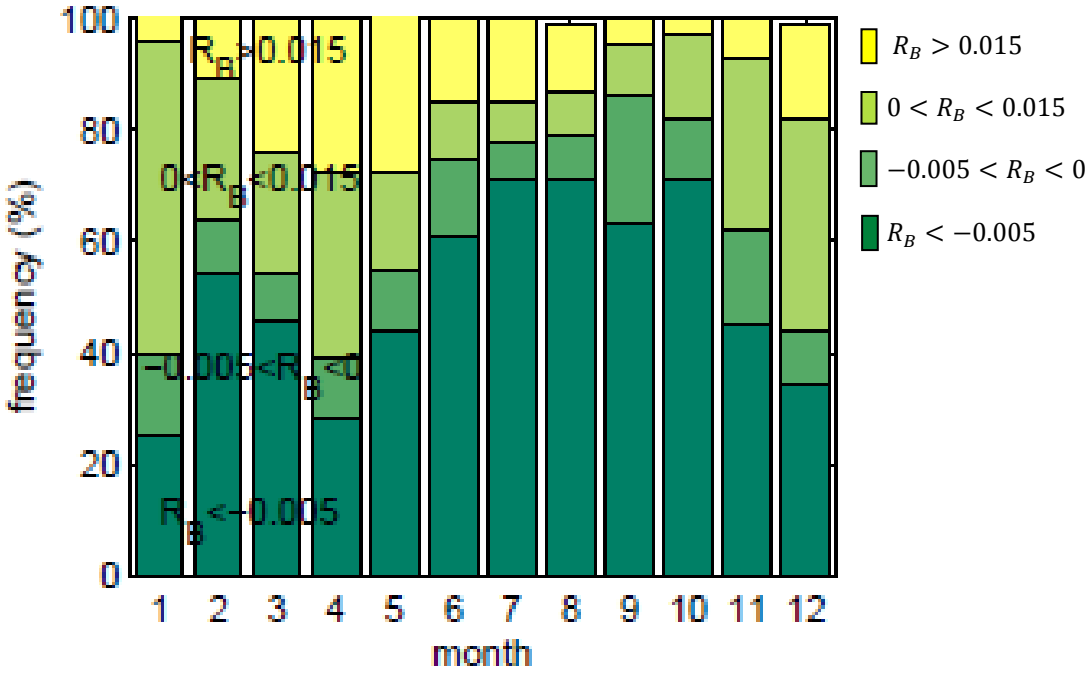

Figure 9.22: Stability classification of Horns Rev from 2003-2007.

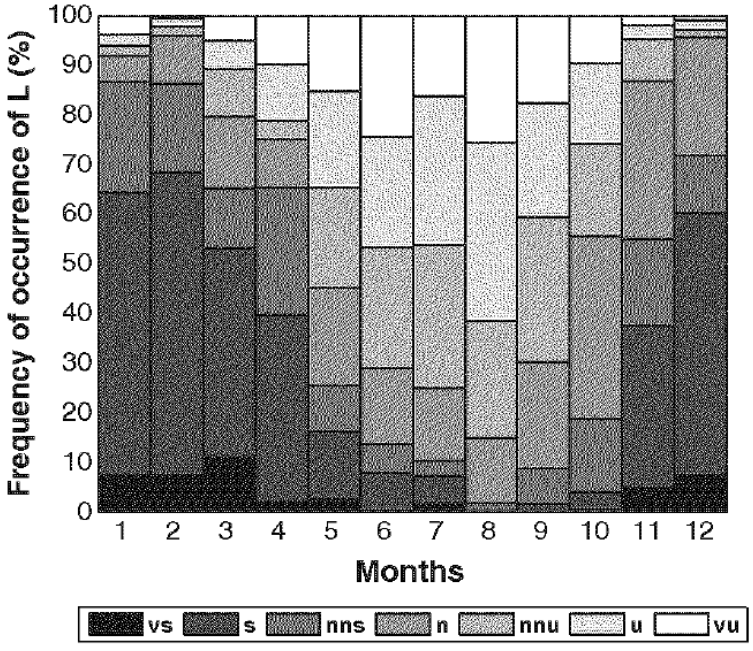

Figure 9.23: Stability classification of Horns Rev from 1999-2006.

Since the two formations of the Richardson number yield consistent stability statistics for the months of April to October, the conclusion is made in this paper that when conducting a stability analysis for the Horns Rev site, $Ri_{B,Peña}$ and $R_{B,Larsén}$ are readily interchangeable. Also, delineation of an additional four stability classes is produced in the Sathe *et al.* (2011) classification scheme, namely NNS, NNU, VS, and VU. This is increasingly helpful when attempting to select a temperature region in Figure 9.21 from which to construct the MO temperature profiles. It is observed in Figure 9.23 that May through June have a robust number of occurrences of neutral and near unstable classes similar to the summer and fall months. These months encompass the temperature collection campaign in Figure 9.21 that represent the neutral and near unstable validation cases modeled in this paper. Further, Figure 9.22 exhibits a somewhat larger frequency of neutral and near unstable environments, i.e., light green and green regions, in the months of April to June than the months covering the temperature observations, May to October. Clearly, utilization of Figure 9.23 to classify the dominant N and NU regions on the temperature plot is achieved with greater ease. The modeled neutral case highlighted in Figure 9.21 displays a 0 °C temperature change in the diurnal temperature plot. The modeled near unstable section labeled in Figure 9.21 portrays an average -1.0 °C temperature difference, i.e., $T(55\ m) \approx 9.5$ °C and $T_W \approx 10.5$ °C at day 133 (see Figure 2.37). Moving forward, to construct the unstable temperature profile, the unstable section highlighted in the diurnal temperature plot comprises days 219-225 of July and depicts a temperature change from the surface to 55 m of -1.5 °C, i.e., $T(55\ m) \approx 17.5$ °C and $T_W \approx 19$ °C at day 220 (see Figure 9.21). July is illustrated as predominantly near unstable and unstable in Figure 9.23 and unstable to very unstable in Figure 9.22.

Thus, the selection is concluded representative of the unstable class.

Lastly, the choice of days 300-305, which include the end of October and beginning of November, as symbolic for the very unstable class is decided with the logic that the largest temperature differentials are noticed in this region of the diurnal temperature plot. The temperature difference is -2 °C, i.e., $T(55\ m) \approx 13$ °C and $T_W \approx 15$ °C at day 300 (see Figure 9.21). October and November project readily unstable to very unstable atmospheric conditions in Figure 9.22; however, Figure 9.23 exhibits a more frequent neutral and near unstable class for these months. It seems like more information is required before constructing the MO temperature profile from this region. Thus, computation of the bulk Richardson number for each region selected in the diurnal temperature figure is a necessary step implemented in order to verify that each region is in fact representative of that stability class. To do this, a modified formulation of the bulk Richardson number in (10) reflecting the data labeled in Figure 9.21 is derived. The expression employed is the following

$$R_{B,Martin} = \frac{g}{T(20)} \frac{(T(20) - T_W)}{z} / (\frac{U(20)}{z})^2, \tag{70}$$

where $T(20)$ is the absolute temperature found using the reference data for the MO temperature profile at z = 20 m ASL, T_W = T(-4 m) = T(0 m) is the surface temperature measured at 4 m BSL and approximated from Figure 9.21, z is the difference between the surface and the first temperature measurement, or 20 m ASL, and $U(20)$ is the velocity at 20 m ASL extracted from the MO velocity profile. Each selected region in focus is listed in the table below, which also estimates the bulk Richardson number from (70) and compares this value to the Larsén *et al.* (2011) version, (10), and the Peña *et al.* (2008)

variant, (5), of the bulk Richardson number.

Table 9.7: Stability classes selected by Martin and comparison of three bulk Richardson number formulations.

Stability Class	$\bar{L}_b$[m]	Month	Day(s)	Temperature [K]			U(15) [m/s]	U(20) [m/s]	$R_{B,Martin}$	$R_{B,\text{Larsén}}$ Domain (#,#)	$Ri_{B,Peña}$ Domain (#,#)
				Surface	20 m	55 m					
Neutral - N	∞	May	172-176	286.69	286.49	286.15	11.08	11.53	-0.0010	(-0.005,0.015)	(-0.003,0.003)
Neutral - N	1531	May	172-176	286.15	286.44	286.15	11.05	11.48	0.0015	(-0.005,0.015)	(-0.003,0.003)
Nearly Unstable - NU	-288	April	133	283.15	282.52	282.15	11.53	11.76	-0.0032	(-0.005,0)	(-0.0075, 0.003)
Unstable - U	-139	July	220	292.15	291.03	290.65	8.64	8.80	-0.0098	(-∞,-0.005)	(-0.015,-0.0075)
Very Unstable - VU	-73	Sept/Oct	300	288.15	286.53	286.15	6.56	6.67	-0.0249	(-∞,-0.005)	(-0.03,-0.015)

The values of $R_{B,Martin}$ all fall within the domain of $R_{B,\text{Larsén}}$ in Table 9.5. A point of clarification—$Ri_{B,Peña}$ is not computed directly, but is instead found using a rearranged form of equation (4) below

$$\frac{z}{C_1 L} = Ri_{B,Peña}, \tag{71}$$

where $C_1 = 10$ (see the 'Meteorological Measurements at Horns Rev' section and 'Peña *et al.* (2008) Observations' subsection for more details), z is the reference height, 15 m ASL, and L is given the value at each stability class' extrema listed in the following revisited table from Peña *et al.* (2008).

Table 9.8: Stability classes categorized by MO length scale range.

Obukhov length interval [m]	Atmospheric stability class
$10 \leq L \leq 50$	Very stable (vs)
$50 \leq L \leq 200$	Stable (s)
$200 \leq L \leq 500$	Near stable/neutral (ns)
$\lvert L \rvert \geq 500$	Neutral (n)
$-500 \leq L \leq -200$	Near unstable/neutral (nu)
$-200 \leq L \leq -100$	Unstable (u)
$-100 \leq L \leq -50$	Very unstable (vu)

It is encouraging to note the similarity in the extrema values for the domain of $R_{B,\text{Larsén}}$ and $Ri_{B,Peña}$.

Finally, it is decided that the four selections highlighted in Figure 9.21 are representative of those stability classes labeled and are the basis for the construction of

the MO temperature profiles. The next sections provide the results of two neutral cases and three unstable cases using the same approach that was discussed previously, and the simulation results are compared to Figure 9.20 above from Peña *et al.* (2008).

9.3.1 Neutral (N) Validation Study

The neutral (N) validation simulations are performed by considering first that there is a constant gradient in the temperature profile, but no effect of the temperature, T_*, or heat flux at the wall. Thus, for L=∞, the neutral stability temperature profile is modeled as adiabatic, i.e., no heat flux is generated at the wall ($\dot{q_w} = 0$ W/m^2), which is represented in the neutral verification study with the Alinot & Masson (2005) reference data below.

Table 9.9: Adiabatic neutral property table.

Flow Parameter & Property	Value
L	∞ m
$u_{ref}(z_{ref})$	11.21 ms^{-1}
$H = z_{ref}$	15 m
u_*	0.40 ms^{-1}
$T(z_{ref1}) = T_{ref1}$	286.686 K
z_{ref1}	0 m
$T(z_{ref2}) = T_{ref2}$	286.686 K
z_{ref2}	55 m
$T_w = T_{ref1} = T_{op}$	286.686 K
T_*	0 K
κ, von Karman constant	0.40
z_0, surface roughness length	19.6e-5 m
E	9.793
ε_R, roughness height	$20 \cdot z_0$ = 0.00392 m
C_s, roughness constant	0.5
σ_k	1
σ_ε	3D Domain – 1.1
$C_{\varepsilon 1}$	1.176
$C_{\varepsilon 2}$	1.92
C_μ	0.0333
Energy Prandtl Number	1e20
Wall Prandtl Number	1
ρ_0	1.225 kg/m^3
c_p	1006.43 J/kg-K
μ_0	1.8e-5 kg/m-s
k_0, thermal conductivity	0.0242 W/m-K
$\beta = \frac{1}{T_w}$	0.00349 K^{-1}
Peña *et al.*(2008) Average Data	**Value**
No. of Neutral Profiles	314/2016 (16%)
$\overline{L_b}$	-1531 m
$\overline{z_0}$	19.6e-5 m
$\overline{u_{*0}}$	0.40 ms^{-1}
u_{15}	11.10 ms^{-1}

A second way to represent a neutral ABL is by defining a non-adiabatic, or diabatic, neutral case, where there is strong thermal mixing in the surface layer that generates heat such that T_* is non-zero, L has a large negative value, and the first temperature recording, i.e., T(55 m), has the same temperature as the surface. The diabatic neutral case is pictured in Figure 9.21 in which the surface and temperature at 55 m ASL are equivalent. The two neutral cases' flow properties, parameters, and model constants as well as the Peña *et al.* (2008) average data are provided below for $L = -1531\ m$.

Table 9.10: Diabatic neutral property table.

Flow Parameter & Property	Value
L	-1531 m
$u_{ref}(z_{ref})$	11.21 ms^{-1}
$H = z_{ref}$	15 m
u_*	0.40 ms^{-1}
$T(z_{ref1}) = T_{ref1}$	286.15 K
z_{ref1}	0 m
$T(z_{ref2}) = T_{ref2}$	286.15 K
z_{ref2}	55 m
$T_w = T_{ref1} = T_{op}$	286.15 K
T_*	0.0174 K
κ, von Karman constant	0.40
z_0, surface roughness length	19.6e-5 m
E	9.793
ε_R, roughness height	$20 \cdot z_0$ = 0.00392 m
C_S, roughness constant	0.5
σ_k	1
σ_ε	3D Domain – 1.2
$C_{\varepsilon 1}$	1.176
$C_{\varepsilon 2}$	1.92
C_μ	0.0333
Energy Prandtl Number	1e20
Wall Prandtl Number	1
ρ_0	1.225 kg/m^3
c_p	1006.43 J/kg-K
μ_0	1.8e-5 kg/m-s
k_0, thermal conductivity	0.0242 W/m-K
$\beta = \frac{1}{T_w}$	0.00349 K^{-1}
Peña *et al.*(2008) Average Data	**Value**
No. of Neutral Profiles	314/2016 (16%)
$\overline{L_b}$	-1531 m
$\overline{z_0}$	19.6e-5 m
$\overline{u_{*0}}$	0.40 ms^{-1}
u_{15}	11.10 ms^{-1}

The next graphic displays that the N simulation is performing in a consistent manner with all dimensionless profiles aligning to MO theoretical profiles with little to no deviation. The dimensionless temperature profile has the typical undesirable over approximation that was previously discussed in the verification simulations that leads to

an under approximation of the temperature profile, T(y). The error in the dimensionless TDR and TKE profiles necessitate ad hoc corrections mentioned previously in the verification studies—tune the σ_ε constant as recommended in Appendix B to minimize the over approximation in the TKE profile and employ equation (69), the TDR Correction.

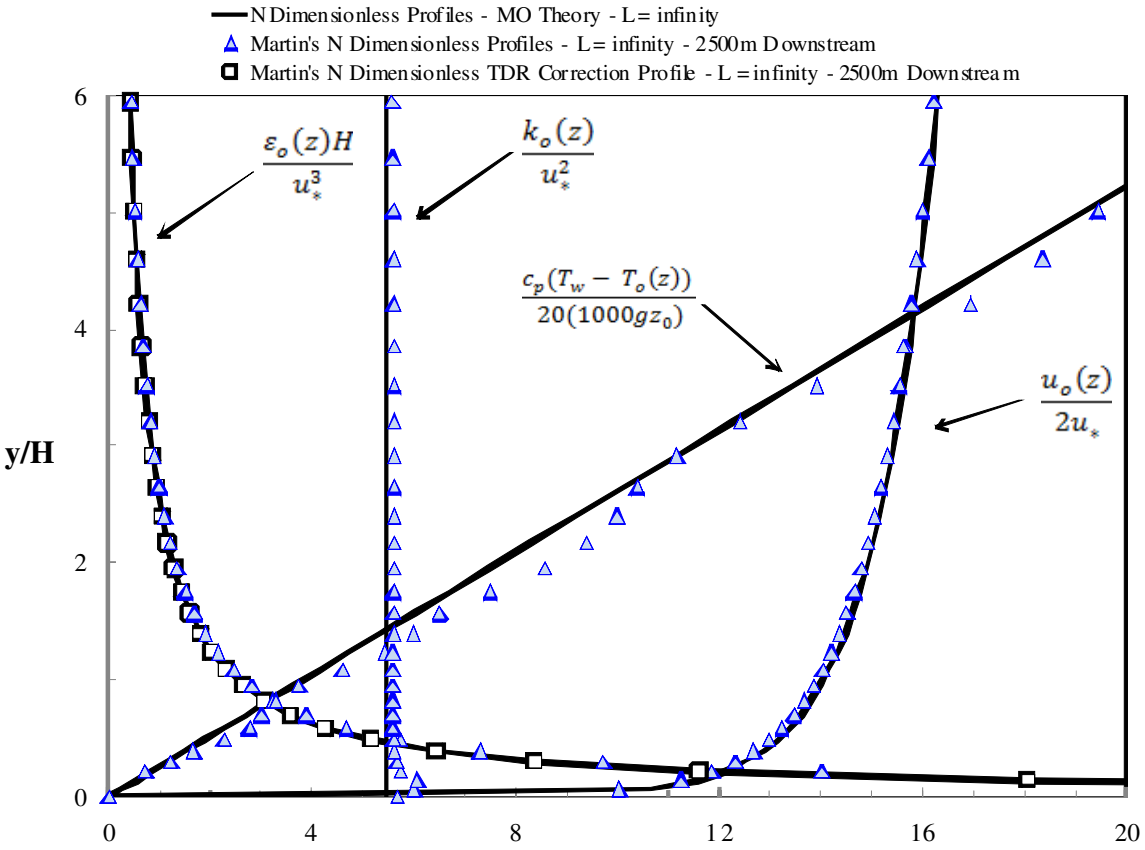

Figure 9.24: Dimensionless profile results for the N validation study at L = ∞.

The dimensionless parameters utilized are labeled in the plot and are referred to as (51)-(54). The gamut of TDR Prandtl numbers tested for the dimensionless TKE correction is 0.7-1.3, and the selection of $\sigma_\varepsilon = 1.1$ is decided. This correction approach is discussed in Appendix B. There is very little error in this simulation, and the output is generated at 2500 m downstream of the 3D 5000 m long domain after laterally averaging

the desired flow variables. The adjustments expected when altering the MO length scale from infinity to -1531 m are illustrated in the next graphic, which indicates the initial MO profiles of a diabatic neutral ABL. The $L=\infty$ simulation results and MO theory profiles are combined with the MO theoretical profiles computed when *L=-1531 m* and are given below.

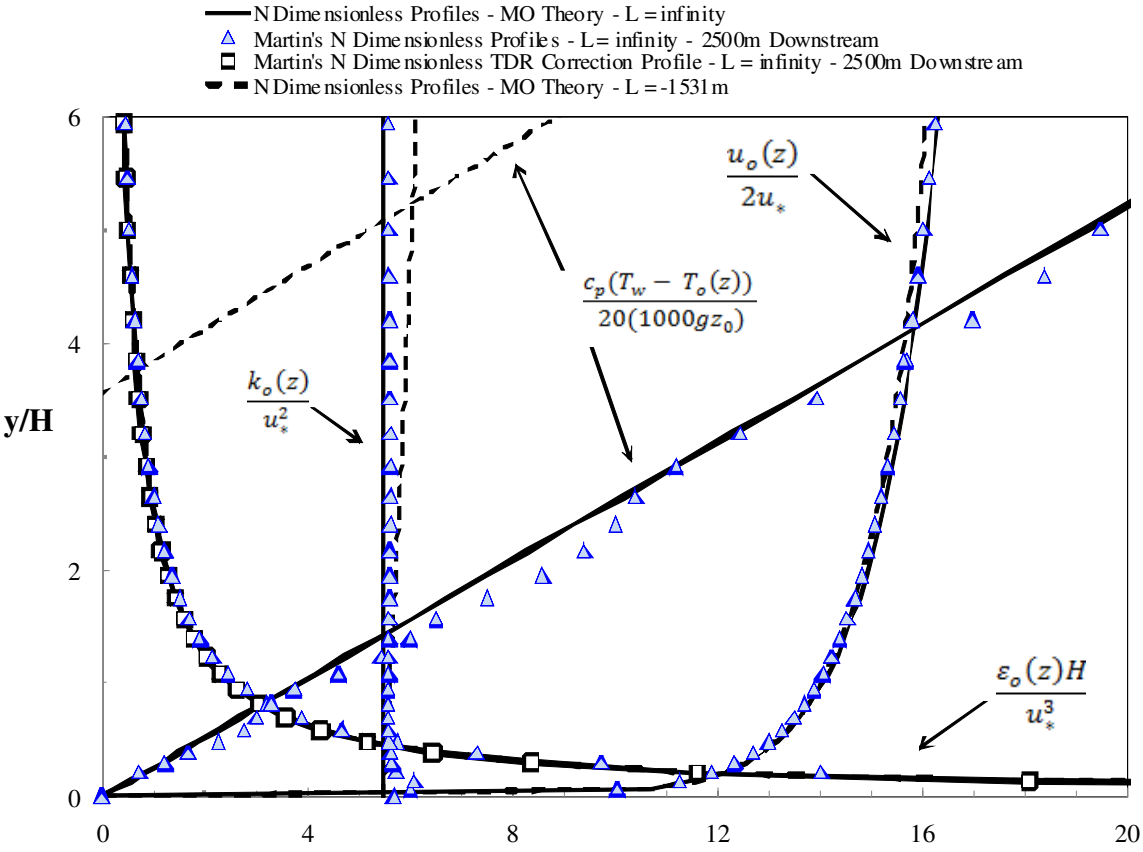

Figure 9.25: Dimensionless profiles for the N validation study at two values of L.

One notices that the MO TDR profile is nearly unchanged between the two cases; on the contrary, the MO TKE profile contains larger values of energy throughout the height of the domain and the MO velocity profile shows a slight slowdown effect for the diabatic case. Lastly, the MO temperature profile maintains the same slope through the height of the domain, but this behavior extends left of the x-axis into the negative region, revealing

that from 0 m to 55 m ASL, or $y/H \approx 3.7$, the difference between the wall temperature and the profile temperature is negative. This alludes to the fact that between the two constant isotherms at 0 m and 55 m ASL, there is an increase in the heat flux causing the temperature to maintain a larger value than both isotherms. After *y/H≈0.5*, the diabatic neutral temperature profile sustains the same slope as the adiabatic neutral simulation.

The diabatic neutral simulation is adjusted to complement Table 9.8, and the simulation is run for the range of TDR Prandtl numbers 0.7-1.3 using the approach cited in Appendix B. After which a value of $\sigma_\varepsilon = 1.2$ is selected since it minimizes the TKE over approximation in the surface layer. The following results display that the diabatic neutral code is able to replicate the MO theoretical profiles modified for *L=-1531 m*.

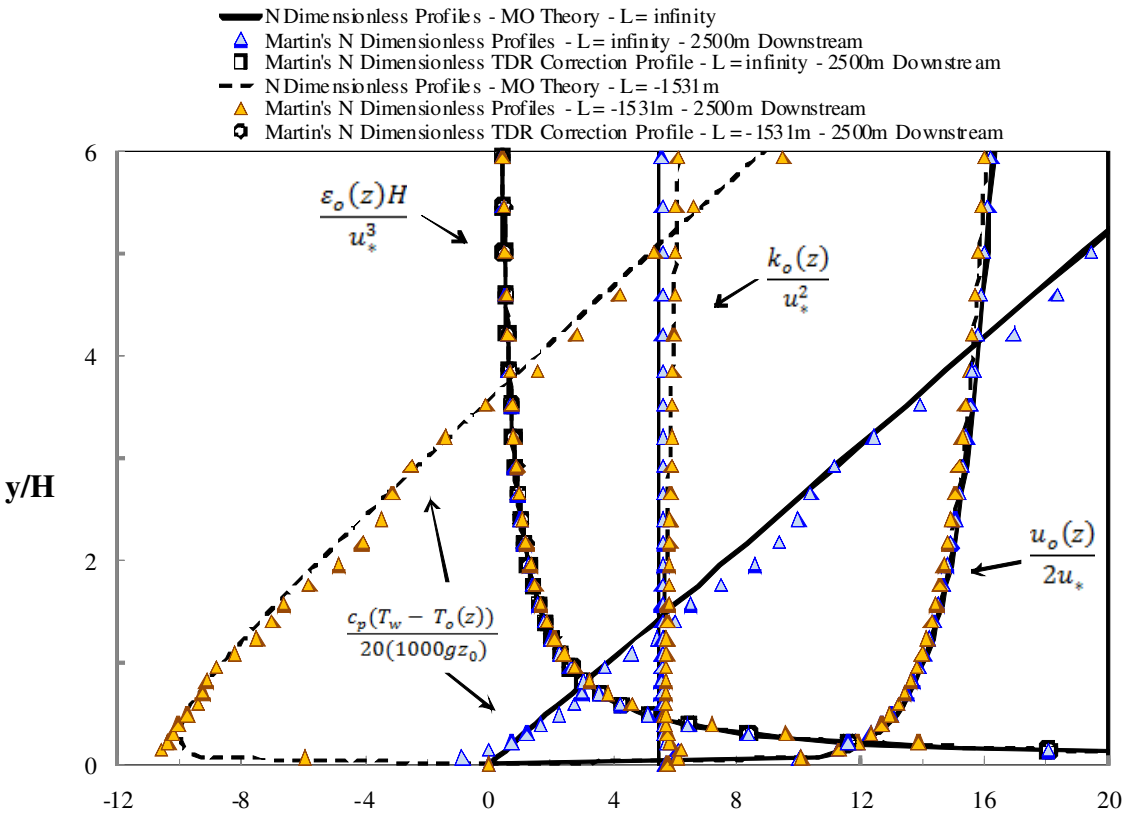

Figure 9.26: Dimensionless profile results for the N validation study at two values of L using the neutral dimensionless parameterizations.

It should be pointed out that the TDR Corrections for both adiabatic and diabatic neutral simulations yield the same result; therefore, the white squares and white circles are in fact exactly overlapping one another. Secondly, the diabatic simulations is well-tuned and capable to model the MO theoretical profiles for *L=-1531 m* with little to no error, except for the typical overshoot in the dimensionless TKE profile and the bend in the dimensionless temperature profile in the first five cells, which equates to a height of about 4.5 m from the bottom of the domain. No error reduction solutions are suggested for these simulation outcomes. The abscissa has been extended from -12 to 20 in order to show the negative values that the dimensionless temperature profile takes on from 0 to 3.7 along the ordinate.

Remembering that by definition, when the air temperature is warmer than the surface temperature, a stable atmospheric boundary layer is generated, the next image elucidates that the Martin k-ε code is capable of modeling a slightly neutral to near stable ABL. It is understood that Figure 9.22 represents a stable ABL by the shape of the dimensionless temperature profile, which bends backwards to the left. The dimensionless parameters are labeled in the figure and are previously mentioned as equations (55)-(58). Stable ABL dimensionless profiles are not detailed in this paper; nonetheless, the interested reader is referred to Alinot & Masson (2005), who have quantified stable simulation temperature results similar to Figure 9.22. After the TKE profile is examined for the TDR Prandtl number spectrum of 0.7-1.3 using the approach suggested in Appendix B, it is decided that the dimensionless TKE accuracy is maximized at a value of $\sigma_\varepsilon = 1.2$. The dimensionless TKE profile illustrates a slight over approximation until *y/H≈3.5*. The dimensionless temperature profile somewhat over approximates the MO dimensionless

temperature profile with the largest errors present after *y/H≈2* and in the first few cells to a height of about 4.5 m. The over approximation in the dimensionless temperature profile leads to an under approximation in the temperature profile, T(y), and it is recalled that T_* is positive for stable atmospheric flows. The dimensionless velocity profile shows a minor slowdown, and no recommendations to correct this behavior are proposed. Furthermore, the dimensionless TDR profile's over approximated results are corrected using the TDR Correction equation, which matches the theoretical TDR profile.

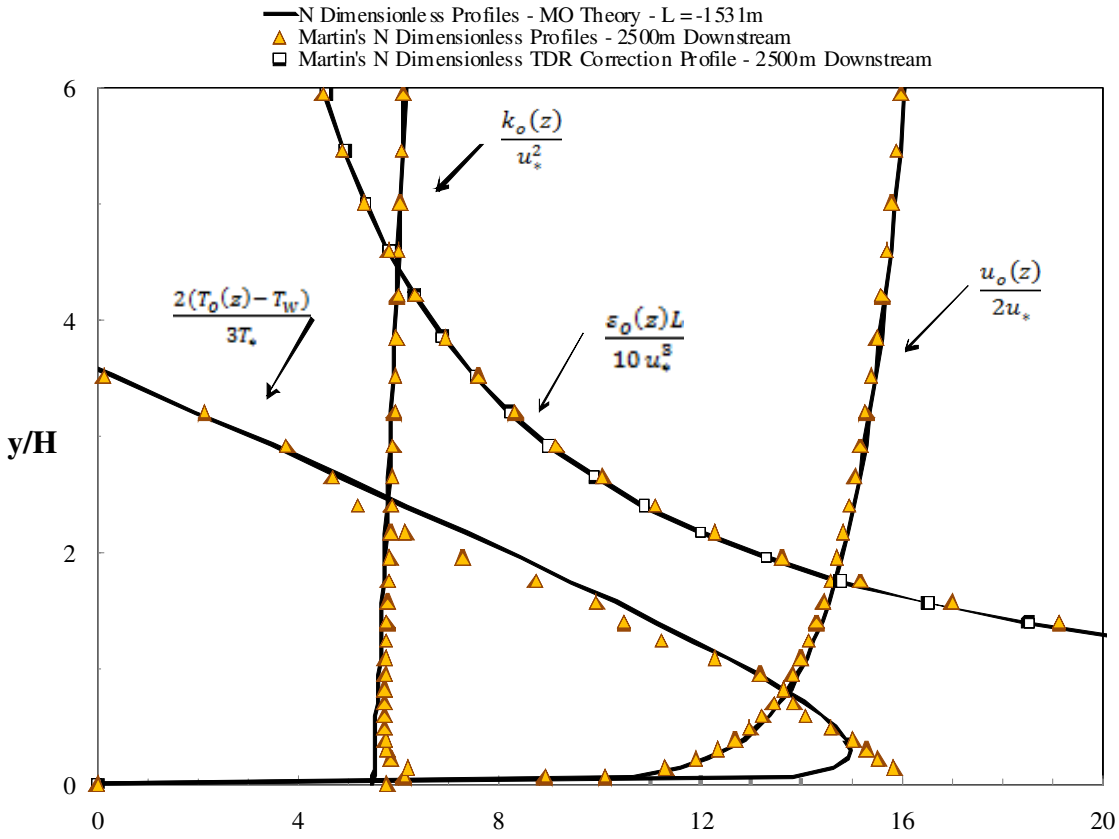

Figure 9.27: Dimensionless profile results for the N validation study at L = -1531 m using the unstable dimensionless parameterizations.

9.3.2 Near Unstable (NU) Validation Study

The near unstable (NU) validation simulation is constructed next for *L=-288 m*. The NU study's flow properties, parameters, and model constants as well as the Peña *et al.* (2008)

average data are provided in Appendix C. The NU case results are presented in the figure below. The tuning of the TDR Prandtl number in the range of 0.7-1.5 is performed using the methodology mentioned in Appendix B, and election of $\sigma_\varepsilon = 1.3$ is made, which minimizes the simulations' dimensionless TKE over approximated areas in the surface layer. The dimensionless quantities are labeled on the plot and are equations (63)-(66). Here again, the dimensionless TDR profile is corrected using the TDR Correction CFF and matches perfectly the MO dimensionless TDR profile for *L=-288 m* after *y/H≈1*. Additionally, the dimensionless velocity profile exhibits a hint of under approximation, while the dimensionless temperature profile is slightly over approximated. The conclusion is made that Martin's k-ε code is capable of maintaining MO theory profiles along the length of the 3D domain to model NU ABLs.

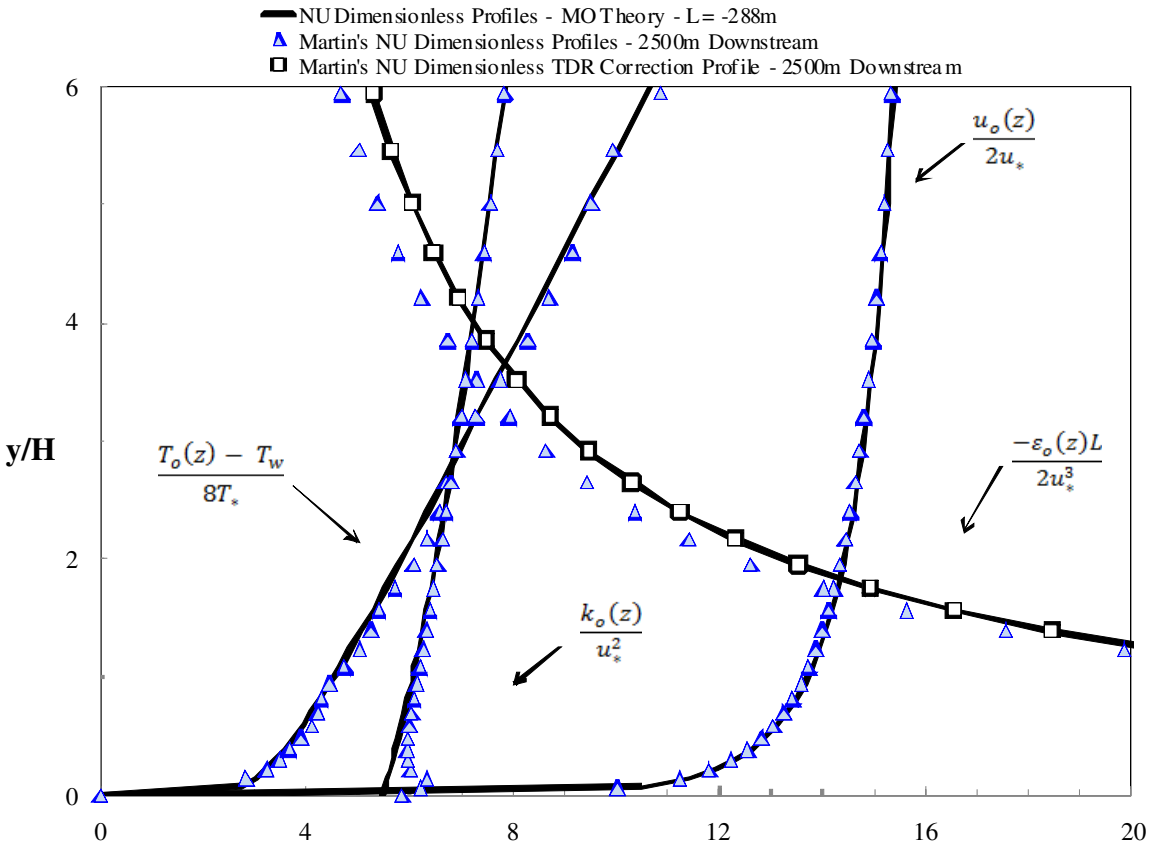

Figure 9.28: Dimensionless profile results for the NU validation study at L = -288 m.

9.3.3 Unstable (U) Validation Study

The unstable (U) validation simulation is created next for *L=-139 m*. The U study's flow properties, parameters, and model constants along with the Peña *et al.* (2008) average data are supplied in Appendix C. The U case results are presented in the next image.

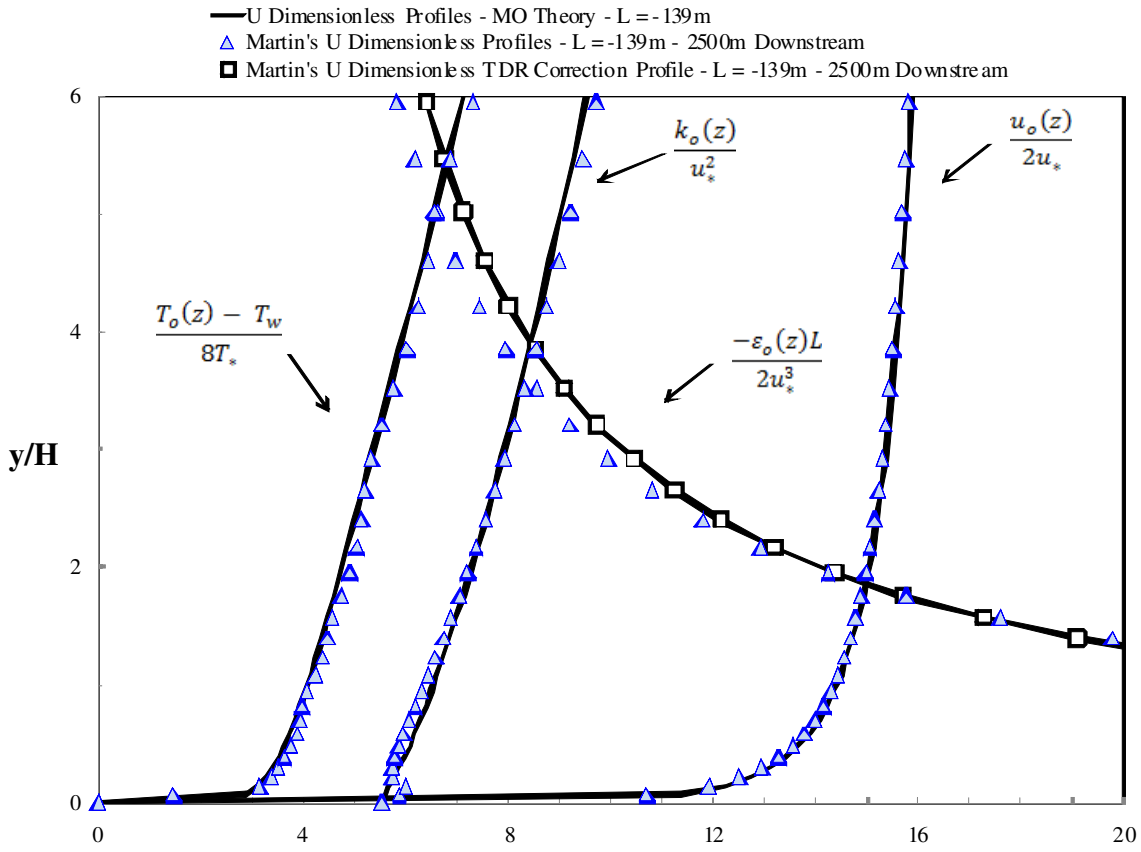

Figure 9.29: Dimensionless profile results for the U validation study at L = -139 m.

The pre-processing TKE profile corrector methodology referenced in Appendix B is performed within the band of TDR Prandtl numbers between 0.7-1.1, and the choice of $\sigma_\varepsilon = 1.0$ is recommended, which educes a slight over approximation. The dimensionless quantities are labeled on the plot and are equations (63)-(66). Once again, the

dimensionless TDR profile is corrected using the TDR Correction equation, which is a comparable solution to the MO dimensionless TDR profile for *L=-139 m*. Moreover, the dimensionless velocity profile contains only a weak under approximation in U(y), and the dimensionless temperature profile is tenuously over approximated indicating that T(y) has a modicum of over cooling. It is concluded that Martin's k-ε code is capable of maintaining MO theory profiles along the length of the 3D domain with the modifications suggested for the U case study.

9.3.4 Very Unstable (VU) Validation Study

The very unstable (VU) validation simulation is prepared at an MO length scale of *L=-73 m*. The VU study's flow properties, parameters, and model constants and the Peña *et al.* (2008) average VU data are detailed in Appendix C. As an initial sensitivity test of the TKE results, the TDR Prandtl number is adjusted within the range of 0.5-1.5 employing the error corrector step methodology cited in Appendix B and illuminates that the best choice is $\sigma_\varepsilon = 0.7$ for a reduction in the TKE profile over approximation compared to the theoretical TKE profile. All results are provided in Figure 9.30.

The simulated TKE profile underestimates the theoretical TKE in the first few cells up to approximately *y/H≈1.5*. Along the length of the curve after *y/H ≈1.5*, an over approximation is noticed in the TKE profile results. For this case, the dimensionless TKE profile demonstrates the largest error in the surface and outer layer in comparison to the aforementioned cases sussed. Perhaps this stability class has a greater tendency to evade current MO theory TKE profiles, which would indicate that theory alone is not a good enough benchmark from which to construct VU k-ε codes.

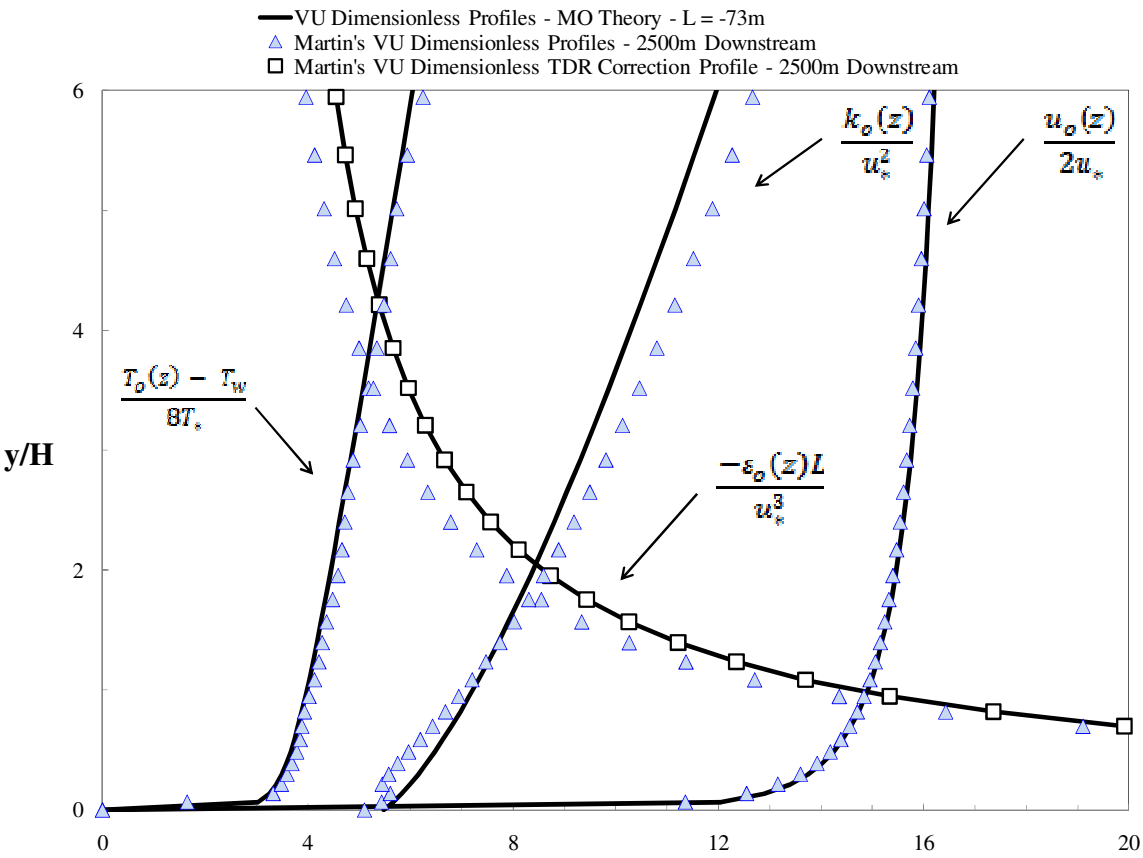

Figure 9.30: Dimensionless profile results for the VU validation study at L = -73 m

The dimensionless quantities are labeled on the plot and are equations (63)-(66). As usual, the dimensionless TDR profile is corrected using the TDR Correction CFF and reproduces the MO dimensionless TDR profile for *L=-73 m*, which initially shows weaker dissipation rates than theorized. In addition, the dimensionless velocity and temperature profiles follow suit with MO theory profiles with a small slowdown effect noted in the velocity profile, U(y), and a slightly heightened cooling in the temperature profile, T(y).

These results point to a weakness in Martin's k-ε code—the dimensionless TKE profile displays the largest incongruity compared to MO theory, yet. It is suspected that this limitation is traced back to the initial boundary conditions, which are based on MO

theory. It is concluded that MO theory for extreme cases of unstable atmospheric conditions may lead to inferior performance of the k-ε unstable codes. To take this topic a step further, the velocity simulation results and friction velocity of each validated stability class are plotted in tandem with the Peña *et al.* (2008) average Horns Rev data set in the next section to visualize how well the simulations perform compared to genuine data.

9.3.5 Comparison with a Horns Rev Data Set from Peña *et al.* (2008)

This section is devoted to judging how well measurements relate to the simulation results obtained in this manuscript. The data set comprises observations garnered at Horns Rev from July to October 2004 and May to October 2006, which extend the wind profile to 161 m using LiDAR observations from 2006. This data set is averaged by Peña *et al.* (2008), who cite nominal parameters for each stability class previously referred to in Table 9.4 and Figure 9.20. The two neutral cases and three unstable studies are plotted together with Figure 9.20. The blue open diamonds represent the adiabatic ($L=\infty$) neutral case, whereas the orange open diamonds correspond to the diabatic ($L=-1531$ *m*) neutral case. The diabatic orange results display similar performance in the first three data markers of the neutral averaged measurements, which relate to the measuring heights at M2, i.e., 15, 30, and 45 m, compared to the adiabatic simulation results. However, the diabatic solution shows an inclination to maintain a larger slope than the neutral data at greater heights. On the contrary, the adiabatic blue simulation reflects better accuracy at greater heights that signify the LiDAR observations, i.e., 63, 91, 121, and 161 m. Both simulations contain weaker velocity, u, than the Horns Rev neutral data and are shifted left of the data. Overall, the adiabatic ($L=\infty$) k-ε simulation performs

superiorly with neutral Horns Rev average data, which is marked by open black diamonds.

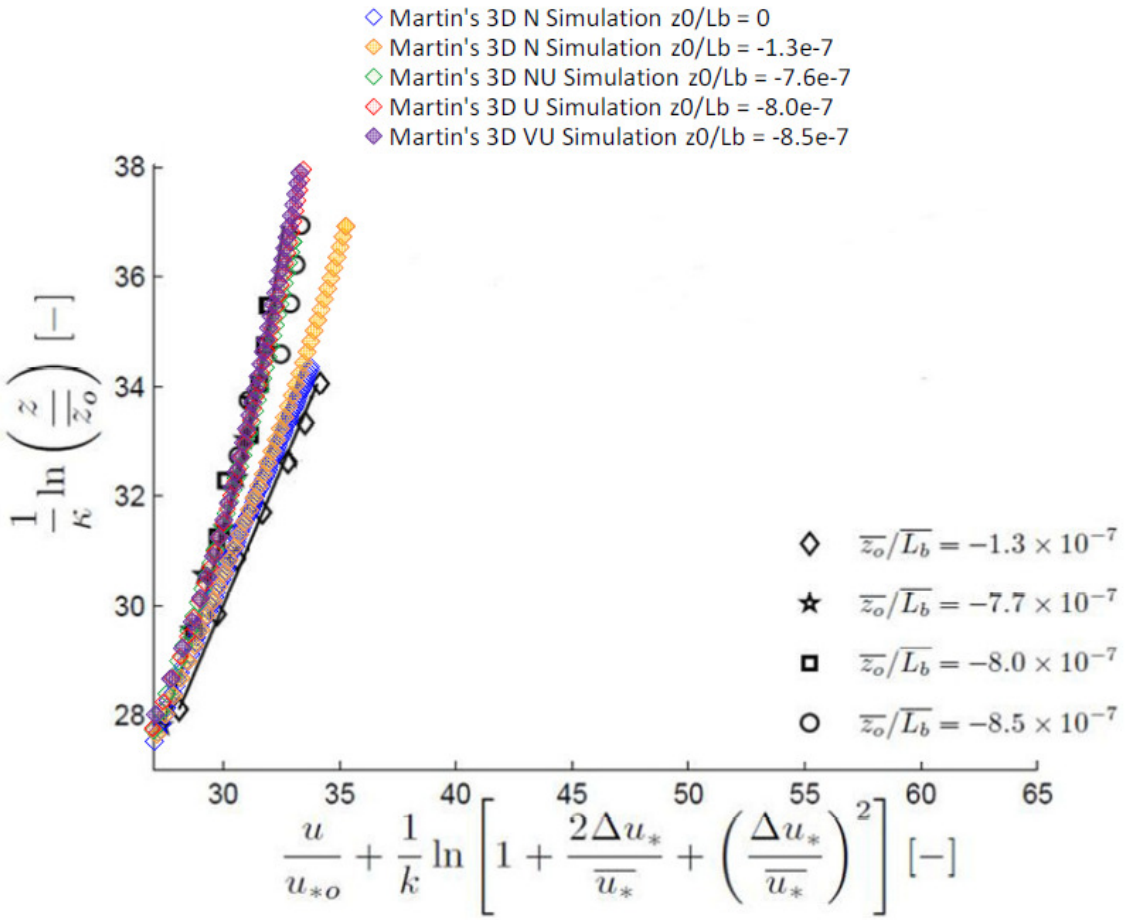

Figure 9.31: Martin's simulation results plotted together with Peña *et al.* (2008).

Next, the general conclusion is made that the unstable k-ε simulations begin to bend leftward toward the y-axis for increased unstable environments, which is desirable and suitable compared to the observations. All simulations fit within the Horns Rev unstable data markers for each unstable class (open star-NU, open square-U, and open circle-VU). A second plot is created that changes the scale along the abscissa for a magnified view of the data and simulation results (see next figure). A side note—the solid lines represent the Peña *et al.* (2008) corrections to MO theory that include average parameters, stability,

and marine roughness, but this correction approach is not detailed in this paper. The abscissa dimensionless quantity used by the authors is reduced to the first term only with the knowledge that there is no variation in the friction velocity, u_*, leading to $\Delta u_* = 0$ in the simulations. The y- and x-axis parameters become the following equation

$$y = \frac{1}{\kappa}\ln\left(\frac{z}{\bar{z}_0}\right) = x = \frac{u}{u_{*0}}, \tag{72}$$

where $\bar{z}_0$ is the average marine roughness length given by Table 9.4 for each stability class, u is the simulated velocity in the 3D domain for each stability class, z is the vertical grid points in the 3D domain, and $u_{*0} = \bar{u}_{*0}$ since there is no deviation in u_{*0} in the k-ε simulations. The closeup on the next page discloses that the k-ε simulations are not as good an approximation of the neutral and unstable classes as was once suggested by Figure 9.31. The comments made for the neutral simulation are upheld—the adiabatic curve produces a better model for the Horns Rev neutral conditions, but it is slightly shifted above the data markers. This trend is sustained the entire height of the simulation domain and signifies that adjustments to the MO theory velocity inlet profile are necessary.

The general trend of increasing unstable thermal stratification is displayed in Figure 9.32 following a sharper bend to the left with larger convective nature, i.e., green(NU) then red(U) then purple(VU). Here again, the simulations seem to be placed within the data markers. But it is noted that the VU data markers recorded by LiDAR observations show wide variability compared to the lower open circle M2 data markers. Variability in the averaged Horns Rev data is viewed in the NU and U classes also.

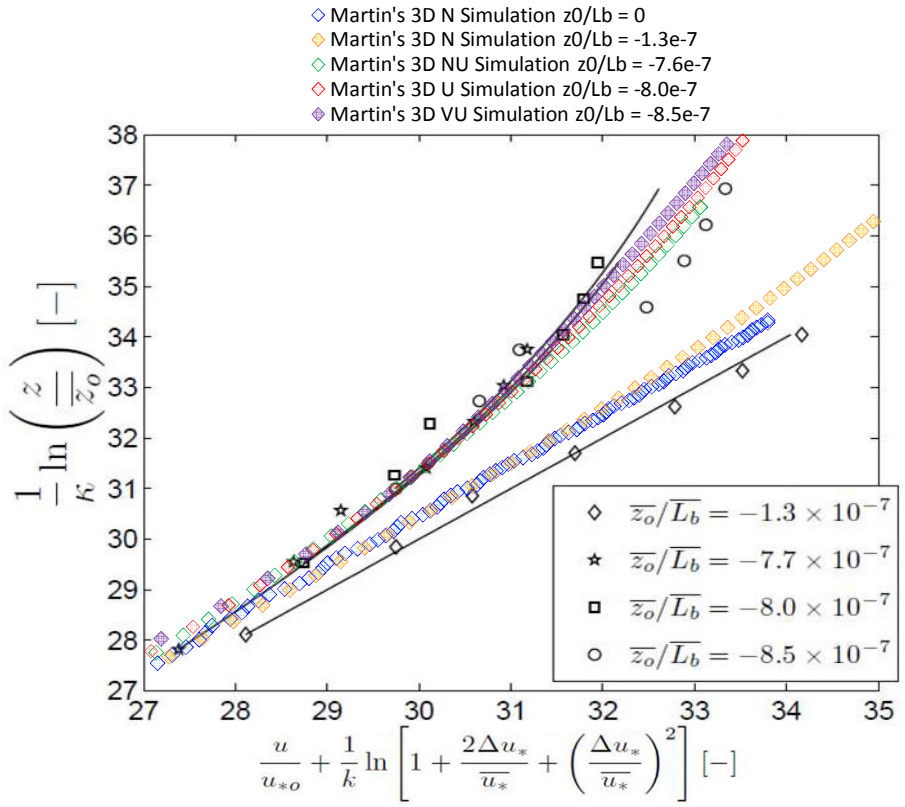

Figure 9.32: Martin's simulation results plotted together with Peña *et al.* (2008). (abscissa = 27-35)

It is concluded that the k-ε unstable simulations perform superiorly in the first three measuring heights, but thereafter are unable to mock the curved nature of the Horns Rev data at greater heights. Once again, since the simulations are steady and align well compared to MO theory with the exception of the dimensionless TKE profile in the SL, it is presupposed that MO theory is the cause of the anomalous behavior in the simulations. Specifically, the simulated velocity results have elucidated the need to redefine the MO velocity profile so that the simulations are better suited to mimic marine thermally stratified and neutral ABLs.

9.3.5.1 Suggested Correction for Simulations

A recommendation to expunge most of the inaccuracy in the Martin neutral and unstable codes when compared to the data highlighted in Peña *et al*. (2008) is to adjust

the MO length scale until the initial inlet velocity profiles nearly match the average data markers in Figure 9.20. For the neutral case, increasing the value of the length scale boosts the average velocity at 15 m by 1.35% compared to the averaged data set values for that stability class recited in Table 9.4. However, this modification corrects the simulation to a near-perfect fit of the Horns Rev data set. Additionally, with respect to the unstable simulations, a decrease in the length scale is the necessary correction methodology, which in turn reduces the average velocity at 15 m by no more than 2.25%. The tradeoff is an improved fit of the simulation results to the Horns Rev data set.

One should expect the initial profiles of the MO temperature, TDR, and TKE to consequently change slightly due to the nomination of a corrected $\bar{L}_b$. The aforementioned recommended values of the TDR Prandtl number, σ_ε, are held constant during this refinement phase and are displayed in Appendix C for the unstable cases and in Tables 9.7 and 9.8 above for the neutral cases.

The altered $\bar{L}_b$ and u_{15} are provided for each simulation in the following table, except for the adiabatic neutral simulation for which no correction is suggested because these simulations are independent of $\bar{L}_b$.

Table 9.11: Corrected $\bar{L}_b$ and u_{15}.

Stability Class	σ_ε	$\bar{L}_{b,Peña}$[m]	$\bar{L}_{b,Martin}[m]$	$u_{15,Peña}$[ms^{-1}]	$u_{15,Martin}$[ms^{-1}]
N	1.2	-1531	-1e20	11.10	11.25
NU	1.3	-288	-215	11.54	11.46
U	1.0	-139	-105	8.60	8.59
VU	0.7	-73	-53	6.65	6.50

Illustrated in the subsequent figure, the corrected simulation results yield more accurate behavior. Peña *et al*. (2008) elucidates that the formulation of the bulk

Richardson number using data collected at the first few measuring heights at M2 to attain the average values of MO length in equation (6) for the unstable classes is too high compared to the average MO length scale that is derived using turbulent fluxes at 50 m from data collected at the M2 sonic anemometer in 2004.

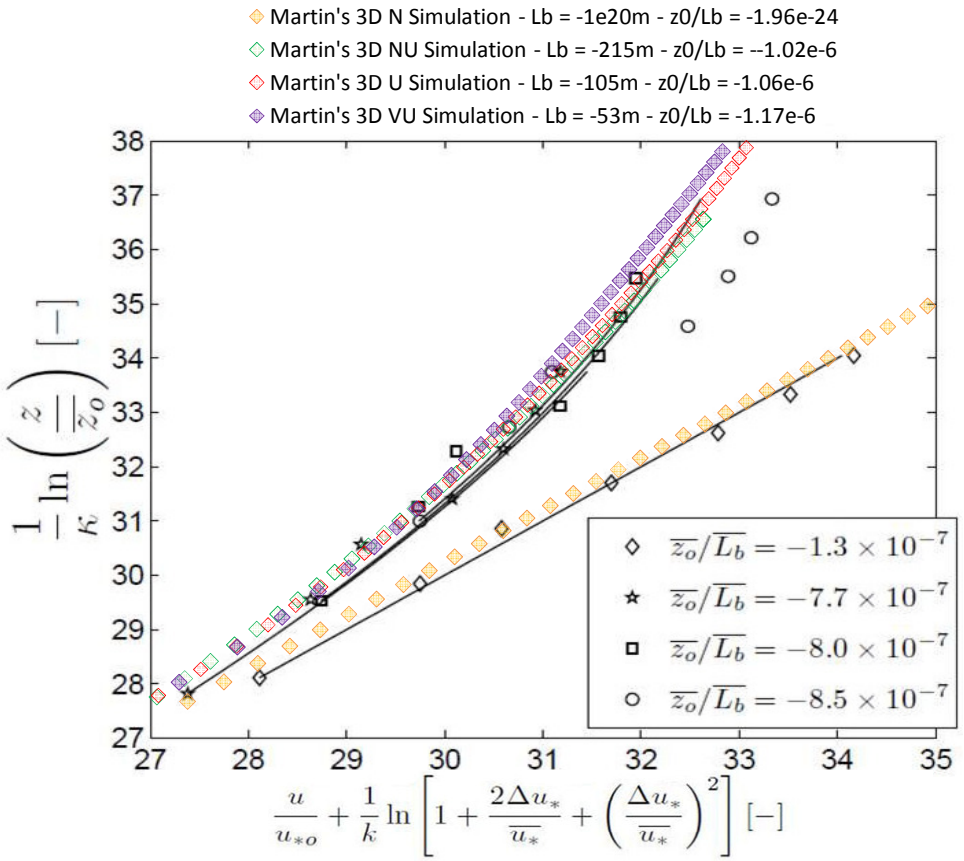

Figure 9.33: Martin's corrected simulation results plotted together with Peña *et al.* (2008).

On the other hand, the MO length derived from the bulk Richardson method are too low for the neutral case when comparing the 2004 sonic-derived MO length at 50 m ASL. The next figure displaying this trend is evidenced below. This conclusion justifies lowering the values of $\bar{L}_b$ for the unstable bins, while increasing the value of $\bar{L}_b$ in the neutral bins in order to obtain better simulation agreement between the observations at the lower measuring heights and those at the higher measuring heights.

Furthermore, it is noted in the same article that MO length scale estimations taking into account humidity fluctuations are most sensitive in the neutral case; thus, the most deviation in the derived MO length scale is presupposed in the neutral simulation. In fact, the neutral simulation correction for $\bar{L}_b$ from -1531 to -1e20 m is the largest adjustment found after correcting all simulations. Lastly, it is worth noting that the LiDAR-averaged observations tend to show a speedup in the wind profile at higher altitudes although they sustain the same profile shape; therefore, perfectly fitting MO similarity theory curves to the Horns Rev data set is challenging as seen in the case of the VU data markers as well as the other unstable classes. On the contrary, the neutral data markers seem to be approximated by MO theory sufficiently well.

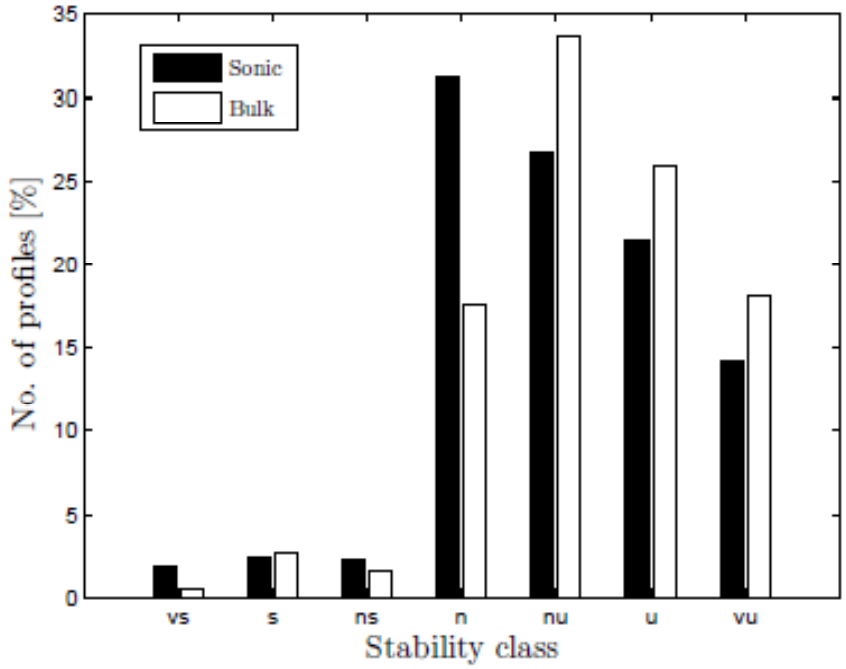

Figure 9.34: Sonic-derived and M2 bulk Richardson number-derived stability bins.

The next figure summarizes the linear relationship between the MO length scale generated by Peña *et al*. (2008) and that obtained by Martin, which is used to forecast the

required length scale needed to construct the MO initial inlet boundary profiles of velocity, temperature, TDR, and TKE, but only after one has computed the average length scale of Horns Rev data, or perhaps marine data anywhere, by employing the bulk Richardson number formulation proposed by Peña *et al*. (2008) (see equations (4) and (5) in this paper).

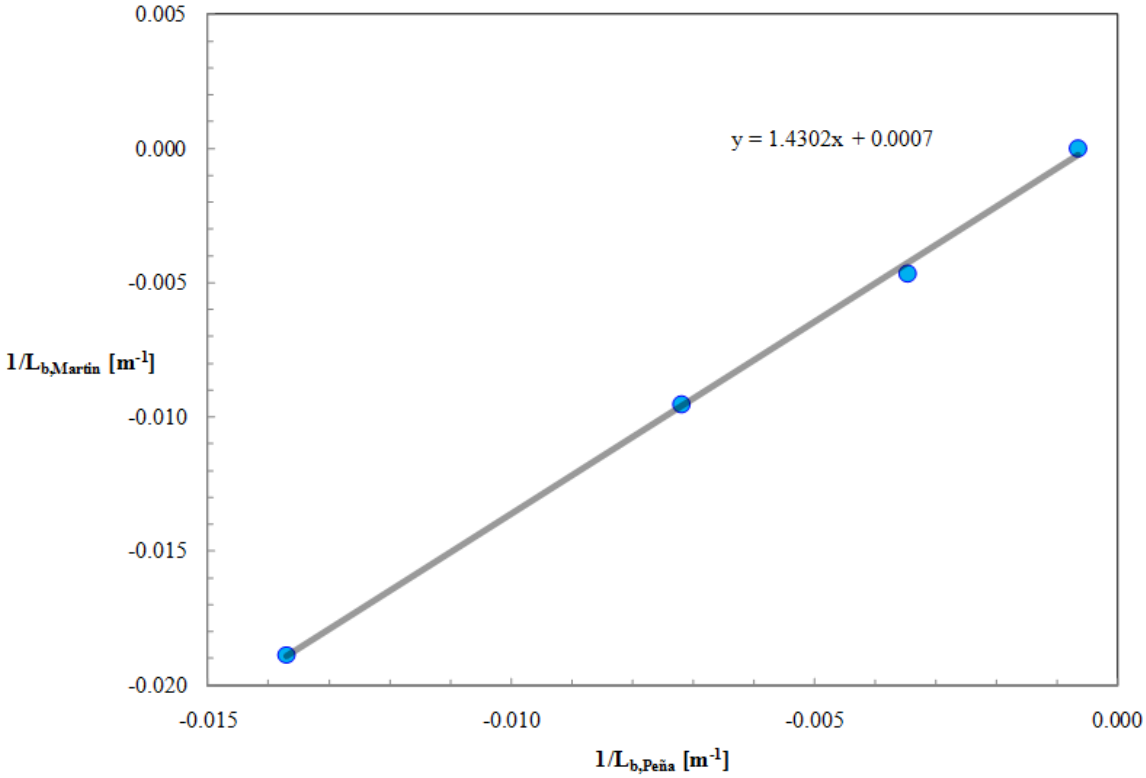

Figure 9.35: Proposed linear relationship between two MO length scales.

Linear regression analyses between MO length scales obtained from various approaches, such as those length scales computed from a WRF model, a bulk Richardson number relationship, and a sonic anemometer-derived length scale formulation, have all recently been portrayed in a study by Peña & Hahmann (2012) for the Horns Rev site. The figure displayed on the previous page generated by Martin is based from this paper's research and functions as a metric to implement when employing the steady k-ε method

in FLUENT 6.3 to model unstable and neutral ABLs at Horns Rev and possibly other marine locations around the world.

10 Limitations of the Customized k-ε Code

It has been noted throughout the manuscript the restricted use of the customized k-ε method devised to model neutral and unstable ABLs. These limitations are supplied in the following list including a brief summary after each heading:

1. Use of velocity inlet condition at outlet

   Utilization of the velocity inlet condition at the outlet is similar to a strong outflow condition—strong meaning the normal flow variables are set by the user and outflow meaning the remaining flow variables such as the temperature, TKE, and TDR are given the value as the neighboring cells. It is obvious that if no obstacles exist in the domain to cause an acceleration or deceleration of the flow, then specification of the normal velocity, U(y), at the outlet follows. However, this application can only be used for models without objects placed inside the domain. Whenever one is attempting to model flow around a structure, the typical specification of the outflow condition at the outlet is desirable so that the normal flow variable U can be given the flexibility to accelerate and decelerate around and past the object.

2. Use of W(y) = 0 m/s initial condition

   When one speaks of the atmosphere and the associated velocity components, they recognize that the Coriolis force produces both a U and W component, where W is the lateral dimension. However, W(y) is set initially to 0 m/s for all heights, and the ABL simulations have not been designed to include the effects of the Earth's rotation. This limitation makes expanding to a 3D domain to characterize

the turbulent structures such as vortices and streaks elusive since these structures can only be determined with the contribution of the W(y) component due to the Coriolis force. Any attempts to model the turbulent structures of neutral or unstable ABLs should comprise the effects of the rotation of the Earth.

3. Use of velocity inlet condition at top and fixing the top 4 m flow variables

   With the specification of the normal vertical velocity using the velocity inlet condition at the top edge and the top 4 m cells' flow variables fixed, the ABL simulations yield results with excessive negative velocity in the interior of the domain that amount to O(-2) to O(-3) m/s at the tradeoff of benefiting the turbulent viscosity profile, TKE, and TDR. Also, the unintended V(y) developments have a negligible effect on the flow variables on which this paper reports. It was shown in the section titled 'Consistency of Velocity Inlet Boundary Conditions' that the unintended vertical velocity gradients with magnitudes larger than O(-2) m/s affect heights beyond 400 m, 100 m downstream of the inlet, 500 m upstream of the outlet, and 100 m from each lateral edge. This provides a sufficiently large 3D domain to model neutral and unstable ABL flows that are free of obstacles. However, if one is modeling flow around objects, the preferred boundary condition at the top of the domain is the symmetry condition without fixing the top 4 m flow variables.

4. Use of 3D domain

   The 3D domain detailed in this document cannot model the turbulent structures native to turbulent ABLs. But it is interesting and even noteworthy to recall the change in the TKE profile with increasing thermal stability. Alinot & Masson

(2005) cites the TDR Prandtl number, σ_ε, of 1.3 for neutral and unstable cases; however, this manuscript details an increase in the TKE profile for unstable simulations necessitating the lowering of the TDR Prandtl number, σ_ε, in enlarged 3D domains.

5. Design of Martin's Richardson number

   Martin's Richardson number given by (70) leaves out the effect of potential temperature differences, and thus the relative humidity is not accounted for in the stability analysis. The relative humidity could play a major role in the stability at Horns Rev and marine environments, which have an excess of moisture. Nonetheless, the simplification utilizing (70) is applied in this manuscript.

6. Exclusion of latent heat computations

   The latent heat is not explicitly computed in this paper when determining the atmospheric conditions at Horns Rev. Instead, the 'Energy Equation', Boussinesq approximation, gravity option, a constant surface temperature, and the MO theorized inlet temperature profile are employed to describe the heat transfer in the CFD simulations.

11 Conclusion

The ambient thermal stability at Horns Rev is considerably unstable during the summer and fall months comprising June to October. The winter and spring seasons tend to develop fewer occurrences of unstable atmospheric conditions. These stability trends are discerned after the Richardson number is calculated. In the past, Horns Rev studies have computed the Richardson number in a variety of different ways illustrating the lack of standardization within the ABL research community on this topic; and not one bulk or gradient Richardson number methodology highlighted in this paper has been endorsed as the touchstone, leaving it up to the experience of the user to determine how he or she will perform a stability analysis.

To generate accurate simulations that are representative of the Horns Rev neutral and unstable ABL, a correction should be considered for the MO length scale found when employing the stability analysis in the same manner as Peña *et al.* (2008). After finding the new MO length scale, this quantity is used to define the MO profiles of velocity, temperature, TDR, and TKE, which are implemented in the FLUENT code as the initial conditions.

The novel k-ε code devised in this paper performs remarkably well and maintains MO initial profiles midway downstream of a 5000 m long and wide 3D domain with the exception of the tendency of the TKE profile to become over approximated with increasing convective stability. Altering the TDR Prandtl number, σ_ε, within the range 0.5-1.5 until the best suited σ_ε yielding the smallest TKE profile error is encouraged. A slight over cooling in the temperature profile, T(y), throughout the entire height of the

domain is also realized. Furthermore, there is a minor slowdown in the velocity profile, U(y). Greater performance is obtained when the user applies CFFs or UDFs for the TDR and turbulent viscosity such as those suggested in this manuscript.

References

61400-12-1 IEC. (2005). Wind turbines - part 12-1: power performance measurements of electricity producing wind turbines. *International Electrotechnical Commission, Geneva*.

Alinot, C. & Masson, C. (2005). k-ε model for the atmospheric boundary layer under various thermal stratifications. *Journal of Solar Energy Engineering*, *127*(4), 438.

Andrén, A., Brown, A.R., Mason, P.J., Graf, J., Schumann, U., Moeng, C.H. & Nieuwstadt, F.T.M. (1994). Large-eddy simulation of a neutrally stratified boundary layer: A comparison of four computer codes. *Quarterly Journal of the Royal Meteorological Society, 120*(520), 1457-1484.

Bhaskaran, R. & Collins, L. (2002). Introduction to CFD basics. Retrieved November 2011, from https://docs.google.com/viewer?a=v&q=cache:pJKeA3WLu0IJ:www.cfluid.com/bbs/attachment.php?aid%3D15671+Bhaskaran,+R.+%26+Collins+Lance&hl=en&gl=us&pid=bl&srcid=ADGEESiblTZlJ5oqdVqQDEKigks7Q9UpBSKks_IRNUXuyU9rrzIvRez3pNEKZKGoJQAN5be76YALvZGN9Jr2BNB-Ku7jYHR0bKZXVK1QHZ1wpfDXGgB6yX2ynLbM7emzR0w_0fcaITdV&sig=AHIEtbTcOFpsv5PAGA5C2bwDz2qdbT0jng.

Blocken, B., Stathopoulos, T. & Carmeliet, J. (2007). CFD simulation of the atmospheric boundary layer: wall function problems. *Atmospheric Environment, 41*(2), 238-252.

Crasto, G. (2007). *Numerical simulations of the atmospheric boundary layer*. Ph.D. thesis. Universita degli Studi di Cagliari, Cagliari, Italy.

Crespo, A., Manuel, F., Moreno, D., Fraga, E. & Hernandez, J. (1985). Numerical analysis of wind turbine wakes. *Workshop on Wind Energy Applications, Delphi, Greece*.

Charnock, H. (1955). Wind stress over a water surface. *Quarterly Journal of Royal Meteorological Society, 81*, 639-640.

Churchfield, M.J., Moriarty, P.J., Vijayakumar, G. & Brasseur, J.G. (2010). Wind energy-related atmospheric boundary layer large-eddy simulation using OpenFOAM: Preprint. In *19th Symposium on Boundary Layers and Turbulence*, 1-26.

Cushman-Roisin, B. (2012). *Environmental fluid mechanics*. Book in preparation. John Wiley & Sons, Inc.

Deardorff, J.W. (1972). Numerical investigation of neutral and unstable planetary boundary layers. *Journal of the Atmospheric Sciences*.

Duynkerke, P.G. (1988). Application of the E-ε turbulence closure model to the neutral and stable. *Journal of the Atmospheric Sciences*, *45*(5), 865-880.

Efiong, A. (2007). *Wind turbine manufacturers; here comes pricing power*. Merrill Lynch. Retrieved February 2011, from http://www.ml.com/media/81290.pdf.

Ferziger, J.H. & Perić, M. (2002). *Computational methods for fluid dynamics*. Springer.

Fluent Inc. (2006a). *FLUENT 6.3 UDF manual*. Fluent Inc., Lebanon.

Fluent Inc. (2006b). *FLUENT 6.3 user's guide*. Fluent Inc., Lebanon.

Fossum, H. E., Pettersson Reif, B. A., Tutkun, M., & Gjesdal, T. (2012). On the use of computational fluid dynamics to investigate aerosol dispersion in an industrial environment: a case study. *Boundary-Layer Meteorol., 144*(1), 21-40.

Garratt, J.R. (1992). *The atmospheric boundary layer.* Cambridge Atmospheric and Space Science Series.

Grachev, A.A. & Fairall, C.W. (1997). Dependence of the Monin–Obukhov stability parameter on the bulk Richardson number over the ocean. *Journal of Applied Meteorology*, *36*(4), 406-414.

Gryning, S-E, Batchvarova, E., Brümmer, B., Jørgensen, H., & Larsen, S. (2007). On the extension of the wind profile over homogeneous terrain beyond the surface boundary layer. *Boundary Layer Meteorol. 124*(2), 251-268.

Hansen, K. (2001). *SITE: hornsrev*. Retrieved June 2011, from http://130.226.17.201/extra/web_docs/hornsrev/description.pdf.

Hargreaves, D.M. & Wright, N.G. (2007). On the use of the k-ε model in commercial CFD software to model the neutral atmospheric boundary layer. *Journal of Wind Engineering and Industrial Aerodynamics 95*(5), 355-369.

Hasager, C.B., Peña, A., Christiansen, M.B., Astrup, P., Nielsen, M., Monaldo, F.M., Thompson, D.R. & Nielsen, P. (2008). Remote sensing observation used in

offshore wind energy. IEEE J. Sel. Topics Appl. Earth Obs. Remote Sens. 1, 67-79.

Hasager, C.B., Peña, A., Mikkelsen, T., Courtney, M., Antoniou, I., Gryning, S-E, Hansen, P. & Sørensen, P.B. (2007). *12MW Horns Rev experiment*. Risø-R-1506(EN). Risø National Laboratory.

Høyer, J.L. & She, J. (2007). Optimal interpolation of sea surface temperature for the North Sea and Baltic Sea. *Journal of Marine Systems 65*(1-4), 176-189.

IEA Wind. (2011). *IEA Wind 2010 annual report*. Retrieved May 2012, from http://www.ieawind.org/index_page_postings/IEA%20Wind%202010%20AR_cover.pdf.

Irtaza, H. (2009). *Experimental and computational determination of wind loads on netted/sheeted scaffolds.* PhD thesis. Oxford Brookes University.

Jones, W.P. & Launder, B.E. (1972). The prediction of laminarization with a two-equation model of turbulence. *International Journal of Heat and Mass Transfer,15*, 301-314.

Larsén, X.G., Vincent, C. & Larsen, S. (2011). Spectral structure of mesoscale winds over the water. In preparation for *Quarterly Journal of the Roy. Met. Soc. & Boundary Layer Meteorol.* Attached to S. Larsen, X. Larsén, C. Vincent, P. Sørensen, P. Pinson, P-J Trombe, H. Madsen, N. Cutululis. (2011). *Meso-scale wind variability. Final Report.* Risø-Report-1794. Risø National Laboratory.

Laurence, D. & Uribe, J. (2011). *The finite volume method* [PowerPoint slides]. Retrieved from http://www.mace.manchester.ac.uk/research/centres/masc/events/training/codeSaturnSyrthes/presentations/2_The%20Finite%20Volumes%20Method.pdf.

Moeng, C-H, Dudhia, J., Klemp, J. & Sullivan, P. (2007). Examining two-way grid nesting for large eddy simulation of the PBL using the WRF model. *Monthly Weather Review 135*(6), 2295-2311.

Moeng, C-H & Sullivan, P. (1994). A comparison of shear- and buoyancy-driven planetary boundary layer flows. *Journal of the Atmospheric Sciences 51*(7), 999-1022.

Monin, A.S. & Obukhov, A.M. (1954). Basic laws of turbulent mixing in the atmosphere near the ground. *Trudy Akademiia Nauk SSSR Geofizicheskogo Instituta 24*, 163-187.

Moskalenko, N., Rudion, K. & Orths, A. (2010). Study of wake effects for offshore wind farm planning. *Modern Electric Power Systems MEPS 2010 Proceedings of the International Symposium*.

Musial, W. & Ram, B. (2010). *Large-scale offshore wind power in the United States*. DIANE Publishing.

Neckelmann, S.A. & Petersen, J. (2000). Evaluation of the stand alone wind and wave measurement systems for the Horns Rev 150 MW offshore wind farm in

Denmark. *Proc. Offshore Wind Energy in Mediterranean and Other European Seas (OWEMES) 2000*, 17–27.

Nieuwstadt, F.T.M., Mason, P.J., Moeng, C-H & Schumann, U. (1992). Large-eddy simulation of the convective boundary layer : A comparison of four computer codes. *Turbulent Shear Flows 8*(1984), 343-367.

Nissen, J.N. & Gryning, S-E. (2009). Application of a numerical model to simulate seasonal differences in onshore normalized wind profiles up to 160 m. In *EWEC 2009 Proceedings online.* EWEC.

O'Sullivan, J.P., Archer, R.A. & Flay, R.G.J. (2011). Consistent boundary conditions for flows within the atmospheric boundary layer. *Journal of Wind Engineering and Industrial Aerodynamics 99*(1), 65-77.

Panofsky, H. & Dutton, J. (1984). *Atmospheric Turbulence*. Wiley, New York.

Pederson, T.F. & Wagner, R. (2011). *Advancements in wind energy metrology – UPWIND 1A2.3.* Risø-Report-1752. Risø National Laboratory.

Peña, A. & Hahmann, A.N. (2012). Atmospheric stability and turbulence fluxes at Horns Rev—an intercomparison of sonic, bulk and WRF model data. *Wind Energy 15*(July 2012), 717-731.

Peña, A., Hasager, C.B., Gryning, S-E, Courtney, M. & Antoniou, I. (2009). Offshore wind profiling using light detection and ranging measurements. *Wind Energy 12*(September 2008), 105-124.

Peña, A., Gryning, S-E & Hasager, C.B. (2008). Measurements and modelling of the wind speed profile in the marine atmospheric boundary layer. *Boundary Layer Meteorology, 129* (3), 479-495.

Peña, A., Gryning, S-E & Hasager, C.B. (2006). LiDAR observations of offshore winds at future wind turbine operating heights. *European Offshore Wind Berlin.*

Perrin, D., McMahon, N., Crane, M., Ruskin, H.J., Crane, L. & Hurley, B. (2007). The effect of a meteorological tower on its top-mounted anemometer. *Applied Energy 84*(4), 413-424.

Richards, P.J. & Hoxey, R.P. (1993). Appropriate boundary conditions for computational wind engineering models using the k-ε turbulence model. *Journal of Wind Engineering and Industrial Aerodynamics 46-47*, 145-153.

Rossby, C. & Montgomery, R. (1935). The layers of frictional influence in wind and ocean currents. *Papers in Physical Oceanography and Meteorology 3*(3), 101.

Salim, S. M., Buccolieri, R., Chan, A., & Di Sabatino, S. (2011). Numerical simulation of atmospheric pollutant dispersion in an urban street canyon: Comparison between RANS and LES. *Journal of Wind Engineering and Industrial Aerodynamics*, *99*(2-3), 103-113.

Sathe, A., Gryning, S-E & Peña, A. (2011). Comparison of the atmospheric stability and wind profiles at two wind farm sites over a long marine fetch in the North Sea. *Wind Energy 14*, 767-780.

Sathe, A. (2010). Atmospheric stability and wind profile climatology over the North Sea – case study at Egmond aan Zee. In *Torque 2010: The Science of Making Torque from Wind Crete, Greece June 28-30*.

Schetz, J. (1993). *Boundary Layer Analysis*. Prentice-Hall, New Jersey.

Seibert, P., Beyrich, F., Gryning, S-E, Joffre, S., Rasmussen, A., & Tercier, P. (2000). Review and intercomparison of operational methods for the determination of the mixing height. *Atmospheric Environment 34*, 1001-1027.

Smirnov, A., Shi, S., & Celik, I. (2001). Random flow generation technique for large eddy simulations and particle-dynamics modeling. *Journal of Fluids Engineering*, *123*(2), 359.

Stull, R.B. (1988). *An Introduction to Boundary Layer Meteorology.* Kluwer Academic.

Tambke, J., Lange, M., Focken, U. & Heineman, D. (2003). Previento meets Horns Rev short term wind power prediction-adaptation to offshore sites. *Proceedings of the European Wind Energy Conference EWEC in Madrid, Spain June 2003*.

Tech-Wise. (2002). *Wind resources at Horns Rev*. Retrieved May 2011, from http://130.226.56.153/rispubl/NEI/nei-dk-4851.pdf.

Tennekes, H. & Lumley, J.L. (1972). *A First Course in Turbulence*. MIT Press.

Troen, I. & Petersen, E.L. (1989). *The European Wind Atlas.* Risø National Laboratory, Roskilde.

Vendel, F., Lamaison, G., Soulhac, L., Volta, P., Donnar, L., Duclaux, O. & Puel, C. (2010). Modelling diabatic atmospheric boundary layer using a RANS CFD code with a k-epsilon turbulence closure. In *13th Conference on Harmonisation within Atmospheric Dispersion Modelling for Regulatory Purposes*.

Vincent, C.L., Hahmann, A.N. & Kelly, M.C. (2011). Idealized mesoscale model simulations of open cellular convection over the sea. *Boundary Layer Meteorology, 1-19.*

Yahyai, M., Daryan, A. S., Ziaei, M., & Mirtaheri, S. M. (2011). Wind effect on milad tower using computational fluid dynamics. *The Structural Design of Tall and Special Buildings, 20*, 177-189.

Appendix A: Computation of Wind Deficit, u_d

To compute the wind deficit, u_d, use the following relation

$$u_d = 1 - (0.062C_t^2 + 0.076C_t)(\frac{L}{R} - 0.082), \quad \text{(A-1)}$$

where *R* is the distance from the center of the boom/lattice to the end of the iso-circle formed by the iso-speed plot of the angle between the boom/lattice and the wind direction, or θ_{rel}, *L* is the length of the boom/lattice cross-section, and C_t is the thrust coefficient. Additionally, the thrust coefficient is found by employing the expression

$$C_t = 2.6(1 - t)t, \quad \text{(A-2)}$$

where t is the boom/lattice solidity. These equations have been referenced by Peña *et al*. (2009) and are taken from 61400-12-1 IEC (2005). An example of an iso-speed plot with the related variables and boom/lattice geometry is supplied in the figure next.

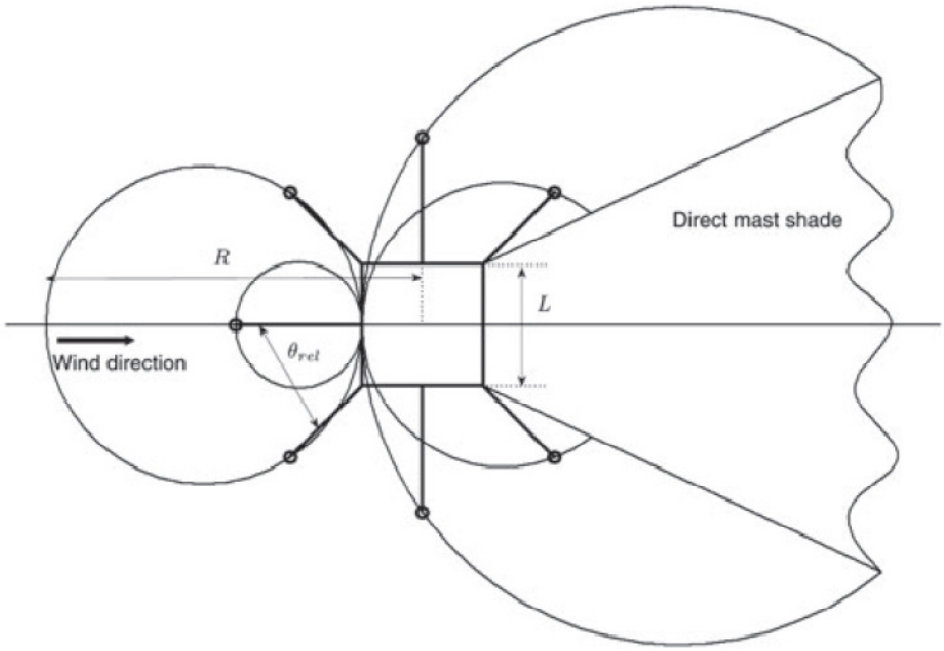

Figure A.1: Iso-speed plots used to compute the wind deficit.

Appendix B: Correcting the Simulated Dimensionless TKE Profile

A corrector pre-processing step is recommended by this author who noted that the TKE profile begins to shift rightward and yield over approximated results with increasing unstable nature of the flow desired to model. Although, it is considered misleading to use 3D meshes that are smaller than those meshes required to model lateral streaks and other developing 3D characteristics of the flow as highlighted by Moeng *et al.* (2007), it is suggested by this paper's author to choose a smaller 3D domain on which testing of the initial MO profile conditions and boundary conditions is attempted as a pre-processing step to correct the typical shift in the TKE profile as the thermal stability increases in a flow. A domain that has been employed by previous authors is used during this step to find the best suited TDR Prandtl number, σ_ε, that minimizes the TKE over approximation by reducing the σ_ε constant. The smaller mesh suggested to perform the TKE profile corrector step on is called '3D(S)' where 'S' stands for the 'Small' 3D domain.

The 3D(S) mesh is amalgamated from Hargreaves & Wright (2007) and O'Sullivan *et al.* (2011). The 3D(S) mesh is constructed from a rectangular brick with the dimensions 5000 m x 500 m x 10 m in the x-, y-, and z-direction, respectively, where the z-direction is taken as the lateral dimension. The vertical edge is comprised of 50 non-uniform hexahedral cells with a vertical stretching ratio of 1.076 and the first cell set 1 m from the ground. The specifications in Figure B.1 are taken from an intercomparison between Hargreaves & Wright (2007) and O'Sullivan *et al.* (2011). Following the precondition to avoid generating an IBL, Hargreaves & Wright (2007) selects the first cell height of 1 m and the boundary mesh stretches at a ratio of 1.076 for a total of 50 cells and total length

of 500 m. This is also followed in the 3D(S) mesh. The streamwise and lateral lengths are uniformly spaced hexahedral cells. The lengthwise edge is shared by both authors extending 5000 m with 500 cells given a uniform length of 10 m. The lateral edge comprising the O'Sullivan *et al.* (2011) domain is elected in this paper. Since each author's grid yields errors of the same order, it was decided that the thinner mesh would be beneficial as an initial test of the TKE rightward shift. Thus, a 10 m wide lateral edge composed of 1 cell with a thickness of 10 m is chosen. It should be noted that this pre-processing step cannot be reproduced on the 2D domains because all 2D simulations show near-perfect accuracy in the TKE profile and are void of an overshoot regardless of the stability class of the modeled flow (see Figures 9.13 and 9.14). On the contrary, 3D domains illustrate an overshoot and a rightward shift in the TKE profile with increasing unstable nature. Thus, this corrector step can only be implemented in smaller 3D domains. The domain details and characteristics are viewed in the figure below and in the table on the following page.

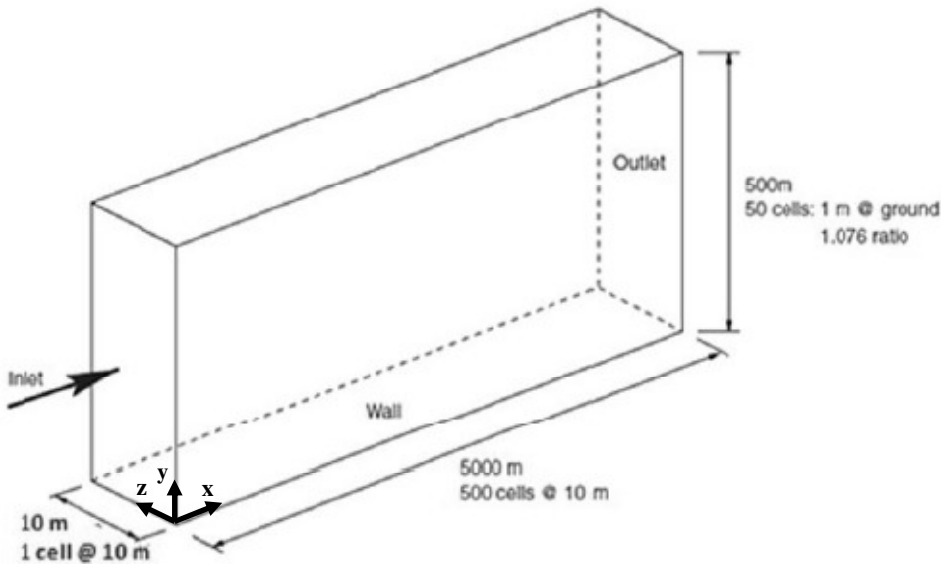

Figure B.1: Domain details of mesh 3D(S).

Table B.1: Domain characteristics for mesh 3D(S).

Mesh Name	Lx, Lz (m)	Ly (m)	Δx, Δz (m)	Δy (m)	Total Cells	Total Nodes	Disk Space (Kb)
3D(S)	5000, 10	500	10, 10	50 cells; 1m at ground; 1.076 ratio	25500; Hexahedral	52104	6,655

The proposed initial conditions, boundary conditions, and solution approach remain the same as that detailed in the 'Boundary Conditions and Prescribed Quantities' and 'Solution Approach and Numerical Schemes' sections.

It is recalled that the 3D(S) mesh is quite thin and contains only 1 cell in the cross-stream direction; thus, this domain is not suitable for unsteady simulations due to the fact that the lateral turbulence and mean variables are prevented from reaching a genuine nature. The details of enlarged 3D domains that allow for 3D modeling of the turbulent structures of the ABL are detailed in Moeng & Sullivan (1994), Andrén *et al.* (1994), Churchfield *et al*. (2010) among others. These authors answer the question—how large should ABL CFD simulation domains be? They propose altering the horizontal dimensions of the domain until they are greater than or equal to five times the expected boundary layer height (Moeng *et al*., 2007). In general, the boundary layer height of the CBL at Horns Rev is taken as approximately 500 m (Gryning *et al*., 2007); therefore, the enlarged 3D domain from which the simulation results are processed and which has been described in the text previously is refined to 10 times the expected boundary layer height along the horizontal edges conforming to the dimensional requirements needed to perform accurate steady and unsteady ABL simulations. These final dimensions are 5000 m x 500 m x 5000 m, x-, y-, and z-direction, respectively. These domain characteristics are elucidated in Figure 5.1 in the text for the 3D domain employed in all simulations reported on in the 'Results' section. This domain is considered adequate for modeling

the realistic 3D turbulent behavior of the ABL when employing an unsteady solver like LES in combination with a random turbulence generator like the Spectral Synthesizer. Those who have implemented the Spectral Synthesizer with modest error for high Reynolds number flows are Smirnov *et al.* (2001), Irtaza (2009), Yahyai *et al.* (2011), Salim *et al.,* (2011), and Fossum *et al.* (2012), to name a few.

With the fact that the 3D(S) domain cannot be used to any degree of accuracy for the illustration of 3D structures when using unsteady solvers since this domain is too thin to permit their development, it is still sagacious to take a smaller domain from which to test the sensitivity of the TKE profile rightward shift in the surface layer and the overshoot. This paper's author recommends tuning the dimensionless TKE profile in a smaller 3D domain. By adjusting the k-ε constant σ_ε, also known as the TDR Prandtl number, from a range between 0.5 and 1.5, a better suited simulation of TKE is obtained on an enlarged 3D domain, which exhibits the most severe deviations compared to other average profiles as the unstable nature of the ABL increases. It is recommended to make adjustments to the σ_ε constant using a smaller 3D domain, such as the 3D(S) domain, so that one is able to easily view the outcome of the TKE profile after the modifications are made to σ_ε. It is noted that the results can be post-processed after 4-5 minutes when employing the 3D(S) domain compared to a delay of 16 hours to view the simulation results from the enlarged 3D simulation after modifications to σ_ε are made. The aforementioned are the main reasons why a smaller 3D domain should be used while making minor adjustments to the initial conditions, to the boundary conditions, and to the k-ε constants for an ABL simulation. It is imperative that once the best suited σ_ε is found when using the 3D(S) domain, application of this value with an enlarged 3D domain, such as the one viewed in

Figure 5.1 that allows lateral development of the flow variables, occurs.

B.1 Correcting the Dimensionless Neutral TKE Profile

This paper's author chooses to tune the dimensionless TKE profile by adjusting the k-ε constant σ_ε, also known as the TDR Prandtl number. By culling from a range of σ_ε between 0.5 and 1.5, a better suited simulation of TKE is obtained on the 3D(S) domain compared to the default $\sigma_\varepsilon = 1.3$ used by Alinot & Masson (2005). These values of σ_ε found while employing the 3D(S) domain are verified by the results obtained on the enlarged 3D domain shown in Figures 9.13, 9.19, 9.24, 9.27, 9.28, 9.29, and 9.30. Thus, this methodology does hold true in all simulations aforementioned that were run on the enlarged 3D mesh.

The figure below shows the transformation that occurs as σ_ε is modified between 1.3 in brown, the original Alinot & Masson (2005) specification, and 0.9 in red on the 3D(S) domain in the neutral verification simulation.

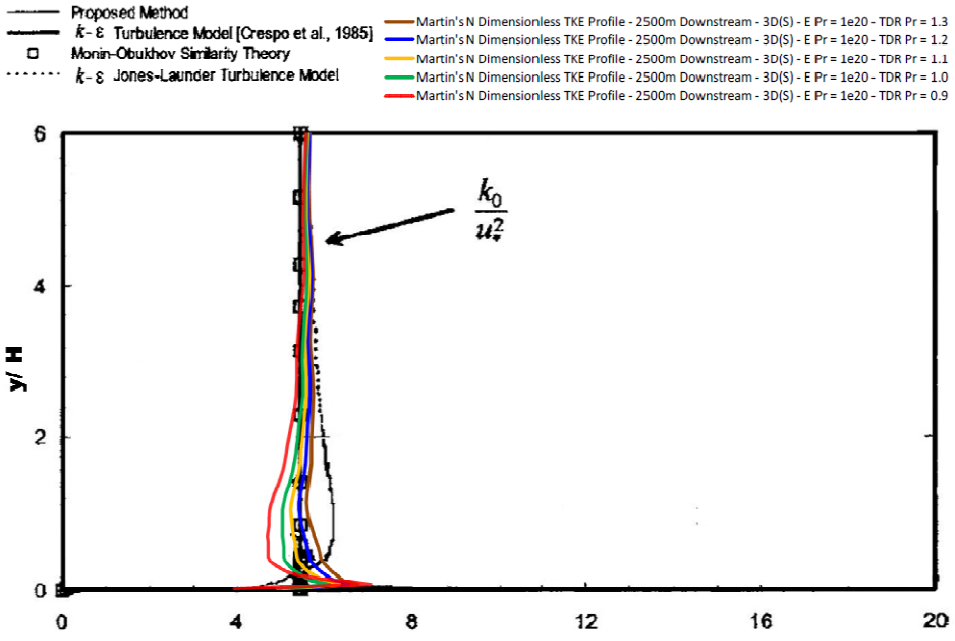

Figure B.2: Dimensionless TKE profiles for assorted σ_ε in the 3D(S) neutral verification study.

The final selection of $\sigma_\varepsilon = 1.1$ is decided because it yields the closest approximation to the MO theory data points, which are shown as open squares, while minimizing the overestimation near the surface displayed in the next figure.

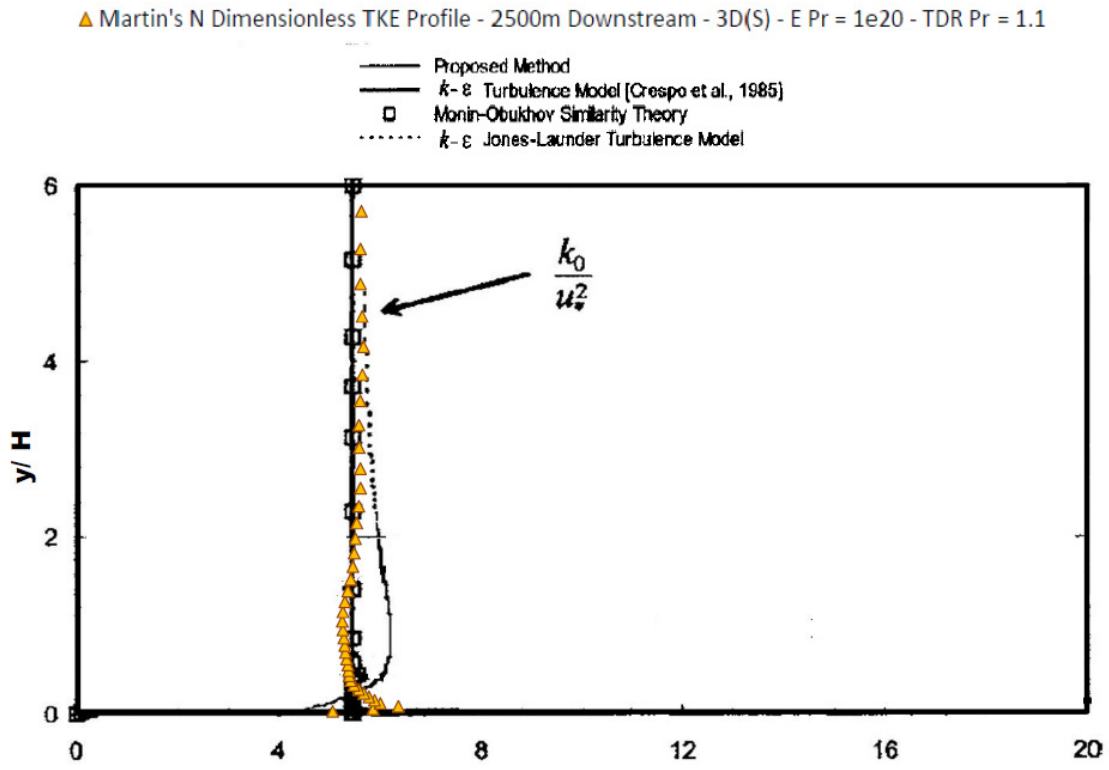

Figure B.3: Dimensionless TKE profile for $\sigma_\varepsilon = 1.1$ in the 3D(S) neutral verification study.

The author of this paper finds that after adjustments to the σ_ε are made in the 3D(S) domain, that these same values provide accurate and well-suited TKE profiles when employed on the enlarged 3D mesh. This methodology would be especially useful for VU simulations when the value of the σ_ε constant is altered significantly from the default Alinot & Masson (2005) constant of 1.3, to the Martin proposed constant of 0.7.

The next image presents the neutral verification dimensionless simulated results using the modified TDR Prandtl number, 1.1, on the enlarged 3D domain in Figure 5.1 along

with the MO theoretical values representing open squares. One notes that the dimensionless TKE profile is under approximated near the surface but retains a more accurate value of TKE after *y/H≈0.8*.

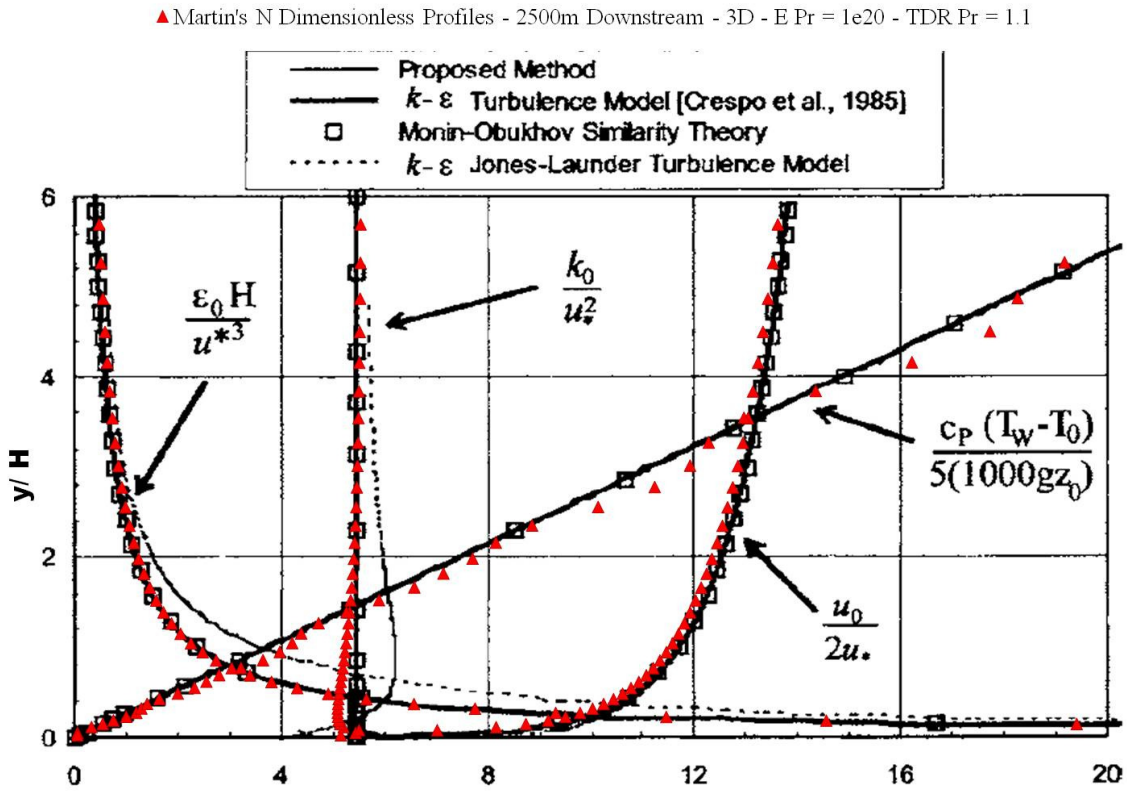

Figure B.4: Neutral verification simulated dimensionless profiles for the enlarged 3D domain using $\sigma_\varepsilon = 1.1$.

B.2 Correcting the Dimensionless Unstable TKE Profile

Mentioned previously, by modifying σ_ε, the dimensionless TKE exhibits greater accuracy compared to the results obtained when employing the value detailed by Alinot and Masson (2005), i.e., $\sigma_\varepsilon = 1.3$. Tuning σ_ε using the 3D(S) domain for the unstable verification case is showcased in the next image for values between 0.9-1.3. It is decided that the most suitable σ_ε is 1.1 after reasoning that this value yields a dimensionless TKE profile that approximates MO theory with a minimal over approximation in the surface

layer as viewed in the bottom figure.

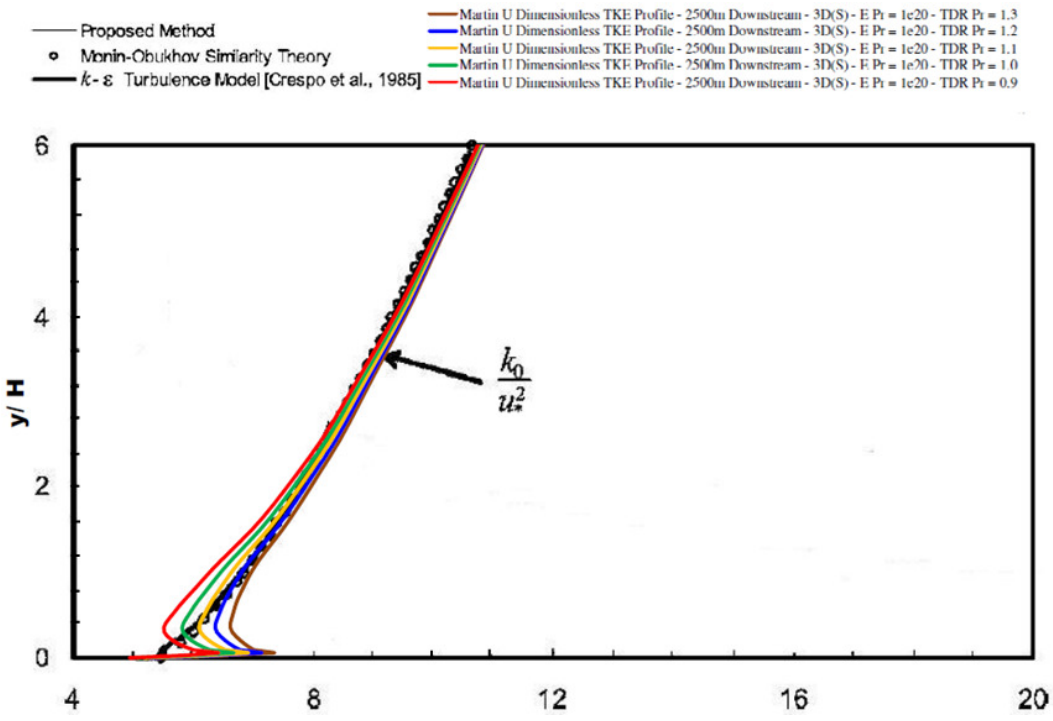

Figure B.5: Dimensionless TKE profiles for assorted σ_ε in the 3D(S) unstable verification study.

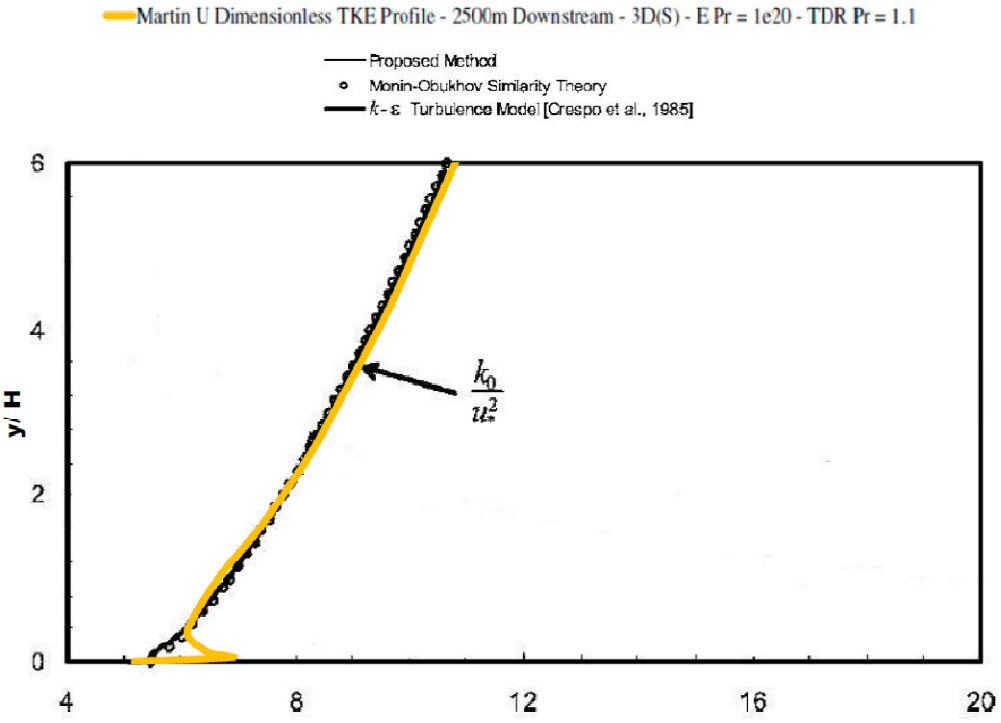

Figure B.6: Dimensionless TKE profile for $\sigma_\varepsilon = 1.1$ in the 3D(S) unstable verification study.

The final results obtained when applying the TDR Prandtl number of 1.1 from the 3D(S) pre-processing corrector step into the enlarged 3D mesh given by Figure 5.1 elucidate that this value is well-suited for enlarged 3D domains as well (see Figure B.7 below).

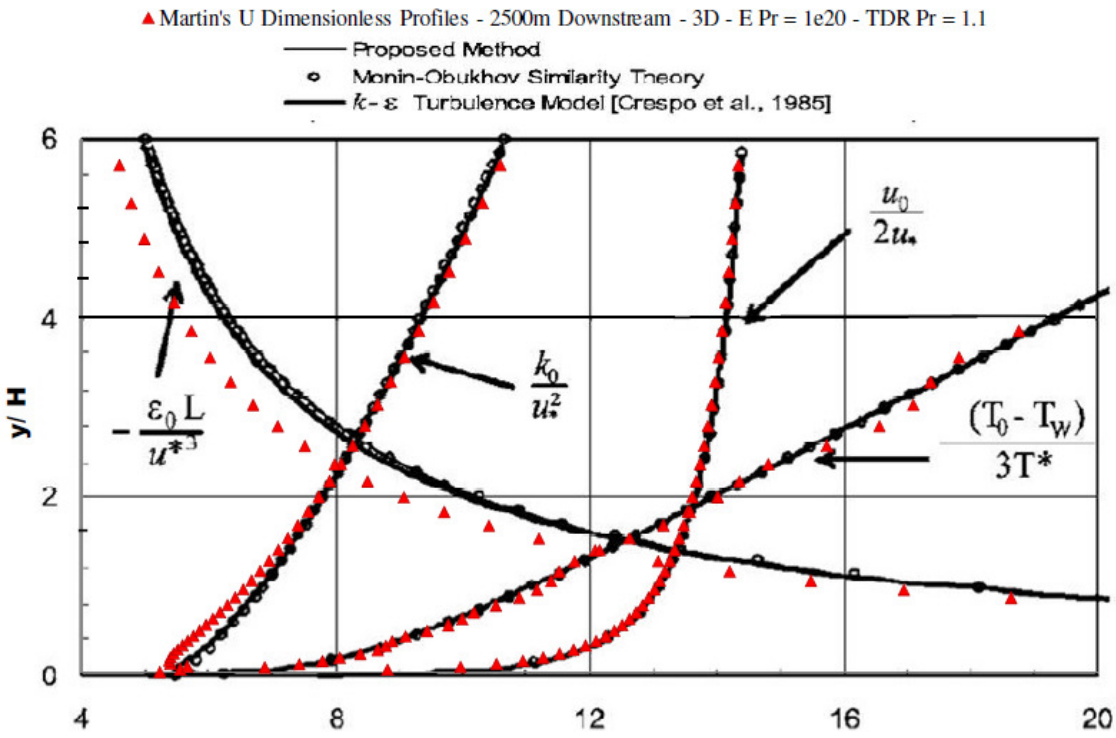

Figure B.7: Dimensionless U verification profiles on the 3D enlarged domain for $\sigma_\varepsilon = 1.1$.

In conclusion, the best suited values of σ_ε found using the 3D(S) mesh produce accurate TKE profiles on the enlarged 3D simulations studied in this paper. These values of σ_ε correct the TKE rightward shift and over approximation found typically in 3D, steady k-ε ABL simulations. The best suited TDR Prandtl numbers found after implementing the pre-processing TKE corrector step on the 3D(S) domain are supplied in the table below for all neutral and unstable simulations. This table can be used as a guide for selecting an appropriate σ_ε for a specific stability class. Recall that L is the MO length scale.

Table B.2: Recommended pre-processed σ_ε for neutral and unstable verification & validation simulations

Case Study	L [m]	Pre-Processed σ_ε
N Verification	∞	1.1
U Verification	-231	1.1
N Validation	∞	1.1
N Validation	-1531	1.2
NU Validation	-288	1.3
U Validation	-139	1.0
VU Validation	-73	0.7

Appendix C: Stability Class Flow Parameter & Property Tables

Table C.1: NU flow parameter & property table.

Flow Parameter & Property	Value
L	-288 m
$u_{ref}(z_{ref})$	11.51 ms^{-1}
$H = z_{ref}$	15 m
u_*	0.42 ms^{-1}
$T(z_{ref1}) = T_{ref1}$	283.15 K
z_{ref1}	0 m
$T(z_{ref2}) = T_{ref2}$	282.15 K
z_{ref2}	55 m
$T_w = T_{ref1} = T_{op}$	283.15 K
T_*	-0.0158 K
κ, von Karman constant	0.40
z_0, surface roughness length	22e-5 m
E	9.793
ε_R, roughness height	$20 \cdot z_0$ = 44e-4 m
C_S, roughness constant	0.5
σ_k	1
σ_ε	3D Domain – 1.3
$C_{\varepsilon 1}$	1.176
$C_{\varepsilon 2}$	1.92
C_μ	0.0333
Energy Prandtl Number	1e20
Wall Prandtl Number	1
ρ_0	1.225 kg/m^3
c_p	1006.43 J/kg-K
μ_0	1.8e-5 kg/m-s
k_0, thermal conductivity	0.0242 W/m-K
$\beta = \frac{1}{T_w}$	0.00353 K^{-1}
Peña *et al.*(2008) Average Data	**Value**
No. of Near Unstable Profiles	600/2016 (30%)
$\overline{L_b}$	-288 m
$\overline{z_0}$	22e-5 m
$\overline{u_{*0}}$	0.42 ms^{-1}
u_{15}	11.54 ms^{-1}

Table C.2: U flow parameter & property table.

Flow Parameter & Property	Value
L	-139 m
$u_{ref}(z_{ref})$	8.64 ms^{-1}
$H = z_{ref}$	15 m
u_*	0.30 ms^{-1}
$T(z_{ref1}) = T_{ref1}$	292.15 K
z_{ref1}	0 m
$T(z_{ref2}) = T_{ref2}$	290.65 K
z_{ref2}	55 m
$T_w = T_{ref1} = T_{op}$	292.15 K
T_*	-0.0325 K
κ, von Karman constant	0.40
z_0, surface roughness length	11.1e-5 m
E	9.793
ε_R, roughness height	$20 \cdot z_0 = 0.00222$ m
C_S, roughness constant	0.5
σ_k	1
σ_ε	3D Domain – 1.0
$C_{\varepsilon 1}$	1.176
$C_{\varepsilon 2}$	1.92
C_μ	0.0333
Energy Prandtl Number	1e20
Wall Prandtl Number	1
ρ_0	1.225 kg/m^3
c_p	1006.43 J/kg-K
μ_0	1.8e-5 kg/m-s
k_0, thermal conductivity	0.0242 W/m-K
$\beta = \frac{1}{T_w}$	0.00342 K^{-1}
Peña *et al.*(2008) Average Data	**Value**
No. of Unstable Profiles	544/2016 (27%)
$\overline{L_b}$	-139 m
$\overline{z_0}$	11.1e-5 m
$\overline{u_{*0}}$	0.30 ms^{-1}
u_{15}	8.60 ms^{-1}

Table C.3: VU flow parameter & property table.

Flow Parameter & Property	Value
L	-73 m
$u_{ref}(z_{ref})$	6.56 ms^{-1}
$H = z_{ref}$	15 m
u_*	0.22 ms^{-1}
$T(z_{ref1}) = T_{ref1}$	288.15 K
z_{ref1}	0 m
$T(z_{ref2}) = T_{ref2}$	286.15 K
z_{ref2}	55 m
$T_w = T_{ref1} = T_{op}$	288.15 K
T_*	-0.0487 K
κ, von Karman constant	0.40
z_0, surface roughness length	6.2e-5 m
E	9.793
ε_R, roughness height	$20 \cdot z_0$ = 0.00124 m
C_S, roughness constant	0.5
σ_k	1
σ_ε	3D Domain – 0.7
$C_{\varepsilon 1}$	1.176
$C_{\varepsilon 2}$	1.92
C_μ	0.0333
Energy Prandtl Number	1e20
Wall Prandtl Number	1
ρ_0	1.225 kg/m^3
c_p	1006.43 J/kg-K
μ_0	1.8e-5 kg/m-s
k_0, thermal conductivity	0.0242 W/m-K
$\beta = \frac{1}{T_w}$	0.00347 K^{-1}
Peña *et al.*(2008) Average Data	**Value**
No. of Very Unstable Profiles	358/2016 (18%)
$\overline{L_b}$	-73 m
$\overline{z_0}$	6.2e-5 m
$\overline{u_{*0}}$	0.22 ms^{-1}
u_{15}	6.65 ms^{-1}

Appendix D: Boundary Profile .txt File for 2D(L) N Verification Study

```
((turb-prof point 52)
(x
0 0 0 0 0 0 0 0 0 0 0
0 0 0 0 0 0 0 0 0 0 0
0 0 0 0 0 0 0 0 0 0 0
0 0 0 0 0 0 0 0 0 0 0
0 0 0 0 0 0 0 0 )
(y
0 1 2.076 3.23378 4.47954 5.81999 7.26231 8.81424 10.4841 12.2809
14.2143 16.2946 18.5329 20.9414 23.533 26.3215 29.3219 32.5504 36.0242 39.7621
43.784 48.1116 52.7681 57.7784 63.1696 68.9705 75.2122 81.9284 89.1549 96.9307
105.297 114.3 123.987 134.41 145.625 157.692 170.677 184.649 199.682 215.858
233.263 251.991 272.142 293.825 317.156 342.259 369.271 398.336 429.609 463.26
499.467 500 )
(u
0.000000000000000 6.383839763642720 7.126776608037900
7.577566249260550 7.909008707971060 8.175264480045000
8.400450828153200 8.597434107558850 8.773892820707080
8.934783892587130 9.083487920443510 9.222409410798470
9.353324764920210 9.477595134578560 9.596266446207610
9.710164256197870 9.819959246665440 9.926200879626250
10.029336577663700 10.129748454513800 10.227750804735700
10.323617847641800 10.417581553102200 10.509841234966700
10.600575267582300 10.689933701741000 10.778050119784100
10.865045351332500 10.951020801327100 11.036072082277700
11.120276781037200 11.203721706353000 11.286463312539400
11.368562066034900 11.450072816711300 11.531043428835700
11.611526012681900 11.691555706587900 11.771163842509000
11.850390876901100 11.929263048958400 12.007810776824300
12.086057254688900 12.164028856819900 12.241745217842200
12.319222131732000 12.396484474654600 12.473545478645600
12.550417854557600 12.627120716160700 12.703660962521400
12.704745774251200 )
(tke
1.000023742617270 1.000023742617270 1.000023742617270
1.000023742617270 1.000023742617270 1.000023742617270
1.000023742617270 1.000023742617270 1.000023742617270
1.000023742617270 1.000023742617270 1.000023742617270
1.000023742617270 1.000023742617270 1.000023742617270
1.000023742617270 1.000023742617270 1.000023742617270
1.000023742617270 1.000023742617270 1.000023742617270
1.000023742617270 1.000023742617270 1.000023742617270
1.000023742617270 1.000023742617270 1.000023742617270
1.000023742617270 1.000023742617270 1.000023742617270
1.000023742617270 1.000023742617270 1.000023742617270
1.000023742617270 1.000023742617270 1.000023742617270
1.000023742617270 1.000023742617270 1.000023742617270
1.000023742617270 1.000023742617270 1.000023742617270
1.000023742617270 1.000023742617270 1.000023742617270
1.000023742617270 1.000023742617270 1.000023742617270
1.000023742617270 1.000023742617270 1.000023742617270
1.000023742617270 )
```

(eps
0.000000000000000 0.185607421995065 0.089406272637315
0.057396428326932 0.041434482557375 0.031891364417304
0.025557628632634 0.021057677348820 0.017703705801649
0.015113503244474 0.013057795459155 0.011390732021349
0.010015023120778 0.008863181162437 0.007887112650111
0.007051551849061 0.006329993008470 0.005702154873521
0.005152298232718 0.004667948171627 0.004239160926253
0.003857851786161 0.003517417189459 0.003212401554821
0.002938239627844 0.002691113186001 0.002467783444642
0.002265483299992 0.002081853291239 0.001914846606855
0.001762703799682 0.001623861959712 0.001496990990951
0.001380904858233 0.001274557404258 0.001177024972700
0.001087477644879 0.001005190507368 0.000929515038887
0.000859858897956 0.000795700226761 0.000736563694716
0.000682024171187 0.000631693770084 0.000585224375371
0.000542301070228 0.000502632001958 0.000465956935841
0.000432038020607 0.000400654971280 0.000371610981296
0.000371214843990)
(t
290.000000000000000 289.990271000268000 289.979782878889000
289.968497621295000 289.956354794074000 289.943288992677000
289.929230231313000 289.914103065688000 289.897826398060000
289.880312405036000 289.861466927456000 289.841189567879000
289.819372130998000 289.795895699453000 289.770634532754000
289.743454117822000 289.714208244786000 289.682739006985000
289.648878750435000 289.612444225430000 289.573241460211000
289.531058937830000 289.485670520354000 289.436833499399000
289.384283722465000 289.327740466600000 289.266900590006000
289.201435607842000 289.130996565881000 289.055203318462000
288.973654275807000 288.885899111513000 288.791476777123000
288.689880411752000 288.580564165218000 288.462943198037000
288.336374186779000 288.200184566040000 288.053653033793000
287.895980309411000 287.726328122969000 287.543780225947000
287.347361885874000 287.136010644357000 286.908595811731000
286.663908719732000 286.400613984877000 286.117307992409000
285.812479906998000 285.484472683445000)
)